AD NUMBER

ADC015969

CLASSIFICATION CHANGES

TO: unclassified

FROM: confidential

LIMITATION CHANGES

TO:

Approved for public release, distribution unlimited

FROM:

Distribution: Further dissemination only as directed by [controlling agency] or higher DoD authority.

AUTHORITY

OCA; 31 Dec 1984 per document markings; DTRA ltr dtd 1 Mar 2000

CONFIDENTIAL

LEVEL II

DNA 4622F

MAGNETIC FLYER FACILITY CORRELATION AND UGT SIMULATION (U)

Kaman Sciences Corporation
P.O. Box 7463
Colorado Springs, Colorado 80933

May 1978

Final Report

CONTRACT No. DNA 001-76-C-0359

THIS WORK SPONSORED BY THE DEFENSE NUCLEAR AGENCY
UNDER RDT&E RMSS CODE B34207T464 N99QAXAC31218 H2590D.

Prepared for

Director
DEFENSE NUCLEAR AGENCY
Washington, D. C. 20305

When this report is no longer needed, Department of Defense organizations will destroy it in accordance with appropriate procedures. Contractors will destroy the report according to the requirements of DoD 5220.22-M, "Industrial Security Manual for Safeguarding Classified Information."

Retention of this document by DoD contractors is authorized in accordance with DoD 5200.1-R, "Information Security Program Regulation."

PLEASE NOTIFY THE DEFENSE NUCLEAR AGENCY, ATTN: TISI, WASHINGTON, D.C. 20305, IF YOUR ADDRESS IS INCORRECT, IF YOU WISH TO BE DELETED FROM THE DISTRIBUTION LIST, OR IF THE ADDRESSEE IS NO LONGER EMPLOYED BY YOUR ORGANIZATION.

UNCLASSIFIED
SECURITY CLASSIFICATION OF THIS PAGE (When Data Entered)

REPORT DOCUMENTATION PAGE		READ INSTRUCTIONS BEFORE COMPLETING FORM
1. REPORT NUMBER DNA 4622F	2. GOVT ACCESSION NO.	3. RECIPIENT'S CATALOG NUMBER
4. TITLE (and Subtitle) MAGNETIC FLYER FACILITY CORRELATION AND UGT SIMULATION (U).		5. TYPE OF REPORT & PERIOD COVERED Final Report.
		6. PERFORMING ORG. REPORT NUMBER K-78-32U(R)
7. AUTHOR(s) W. S. Doane, L. J. Webster T. F. V. Meagher J. Oscarson		8. CONTRACT OR GRANT NUMBER(s) DNA 001-76-C-0359
9. PERFORMING ORGANIZATION NAME AND ADDRESS Kaman Sciences Corporation P.O. Box 7463 Colorado Springs, Colorado 80933		10. PROGRAM ELEMENT, PROJECT, TASK AREA & WORK UNIT NUMBERS Subtask N99QAXAC312-18
11. CONTROLLING OFFICE NAME AND ADDRESS Director Defense Nuclear Agency Washington, D.C. 20305		12. REPORT DATE May 1978 13. NUMBER OF PAGES 162
14. MONITORING AGENCY NAME & ADDRESS (if different from Controlling Office) 12 163p.		15. SECURITY CLASS (of this report) CONFIDENTIAL 15a. DECLASSIFICATION/DOWNGRADING SCHEDULE GDS (84)
16. DISTRIBUTION STATEMENT (of this Report) 18 DNA, SBIE 19 4622F, AD-E300 371		
17. DISTRIBUTION STATEMENT (of the abstract entered in Block 20, if different from Report)		
18. SUPPLEMENTARY NOTES This work sponsored by the Defense Nuclear Agency under RDT&E RMSS Code B34207T464 N99QAXAC31218 H2590D.		
19. KEY WORDS (Continue on reverse side if necessary and identify by block number) Facility Correlation Study UGT Simulation Study Impulsive Loading Magnetically Driven Flyer Plates Pressure-Time Pulse Shaping Using Advanced Capacitor Bank Techniques		
20. ABSTRACT (Continue on reverse side if necessary and identify by block number) The goals of the program were to: (1) Correlate the KSC magnetically driven flyer plate facility test techniques with those of another facility; (2) define AGT test techniques which successfully duplicate UGT test results; and (3) expand the 3DQP material data base. KSC participation in this program touched all three program goals; however, KSC impulsive load testing was most heavily concentrated in goals (1) and (2) under the Facility Correlation Study and the UGT Simulation Study. → (over)		

DD FORM 1 JAN 73 1473 EDITION OF 1 NOV 65 IS OBSOLETE

UNCLASSIFIED
SECURITY CLASSIFICATION OF THIS PAGE (When Data Entered)

389 119

LB

NATIONAL SECURITY INFORMATION
Unauthorized disclosure subject to criminal sanctions.

UNCLASSIFIED
SECURITY CLASSIFICATION OF THIS PAGE(When Data Entered)

20. ABSTRACT (Continued)

This program consists of two phases:

(1) To develop, demonstrate and assess the ability of magnetically driven flyer plates to duplicate the combined shock and structural response caused by a selected underground test (UGT) environment on 3DQP; and,

(2) To correlate the magnetically driven flyer plate facilities of KSC with those of the Atomic Weapons Research Establishment (AWRE) in the United Kingdom.

The program is in progress such that the efforts accomplished to date are described herein. The successful completion of these tasks will not only enhance the simulation capability of the community but it will also develop and demonstrate a methodology for dynamic testing of 3-dimensional materials which ~~utilizes~~ a realistic stimulus. This realism is required to ensure that the critical material response modes are addressed during a period when underground testing may not be available.

The simulation development has been tailored to match the pressure vs. time and total impulse measurements obtained on UGT events. This matching of experimental data required considerable development of capacitor bank technology to develop the proper magnetic pressure vs. time profile. ~~(Indeed, sensitivity~~ studies conducted during the course of this program vividly demonstrated that two different waveforms with the same prompt and total impulse values could produce radically different response modes and failure levels.) The proper simulation environment is realized by the proper control of the post-impact magnetic pressure amplitude and decay time. This significant achievement represents the first known time that these parameters have been utilized to control damage mode and level.

Evaluations of the degree of simulation have been made by detailed examinations of the damage modes and level in addition to correlation of mag flyer induced data with UGT data of pressure vs. time, total momentum and strain signatures on ring specimens. These mag flyer experiments were conducted on 11 arc specimens and 2 rings of 19.6-cm diameter C cycle 3DQP. (The UGT material was the same size and pedigree.)

Included in the damage mode assessment were measurements of the apparent degradation of the dynamic modulus as determined by Electromagnetic Excitation (EME) testing at KSC of both UGT and aboveground (AGT) rings. KSC then utilized this dyamic data to correlate measured strain vs. time signatures from ring specimens. The modeling for the ring analyses included variable thickness and degraded modulus as a function of angle. KSC also conducted ultrasonic and radiographic NDT inspections. The overall agreement between the response of the UGT and the final optimized AGT simulation is very good and is explained in detail herein.

Additional experiments were performed for the sole purpose of comparing the AWRE and KSC facilities including diagnostics, flyer configuration and specimen holding methods. KSC tested 18 3DQP arc samples and 1 3DQP ring from 50.8-cm diameter billets during this course of the program. This larger diameter material was typical of AVCO "A" cycle material; hence it had a minimal contribution to the 3DQP data base. In summary, the current AWRE-KSC facility agreement is in the range of 10 to 15%, depending on the criteria.

UNCLASSIFIED
SECURITY CLASSIFICATION OF THIS PAGE(When Data Entered)

While individual paragraphs, sections, graphs, figures, etc., are unclassified, this report is overall classified Confidential because of the advanced state of technology used in evaluating a potentially operational material.

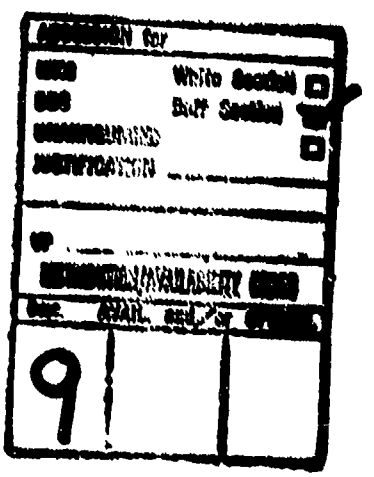

SUMMARY

This program consists of two phases:

1) To develop, demonstrate and assess the ability of magnetically driven flyer plates to duplicate the combined shock and structural response caused by a selected underground test (UGT) environment on 3DQP; and,

2) To correlate the magnetically driven flyer plate facilities of KSC with those of the Atomic Weapons Research Establishment (AWRE) in the United Kingdom.

The program is in progress such that the efforts accomplished to date are described herein. The successful completion of these tasks will not only enhance the simulation capability of the community but it will also develop and demonstrate a methodology for dynamic testing of 3-dimensional materials which utilizes a realistic stimulus. This realism is required to ensure that the critical material response modes are addressed during a period when underground tests might not be available for hardness confirmation.

The simulation development has been tailored to match the pressure vs. time and total impulse measurements obtained on UGT events. This matching of experimental data required considerable development of capacitor bank technology - to develop the proper magnetic pressure vs. time profile. (Indeed, sensitivity studies conducted during the course of this program vividly demonstrated that two different waveforms with the same prompt and total impulse values could produce radically different response modes and failure levels.)

The proper simulation environment is realized by the proper control of the post-impact magnetic pressure amplitude and decay time. This significant achievement represents the first known time that these parameters have been utilized to control damage mode and level.

Evaluations of the degree of simulation have been made by detailed examinations of the damage modes and level in addition to correlation of mag flyer induced data with UGT data of pressure vs. time, total momentum and strain signatures on ring specimens. These mag flyer experiments were conducted on 11 arc specimens and 2 rings of 19.6-cm diameter C cycle 3DQP. (The UGT material was the same size and pedigree.)

Included in the damage mode assessment were measurements of the apparent degradation of the dynamic modulus as determined by Electromagnetic Excitation (EME) testing at KSC of both UGT and aboveground (AGT) rings. KSC then utilized this dynamic data to correlate measured strain vs. time signatures from ring specimens. The modeling for the ring analyses included variable thickness and degraded modulus as a function of angle. KSC also conducted ultrasonic and radiographic NDT inspections. The overall agreement between the response of the UGT and the final optimized AGT simulation is very good and is explained in detail herein.

A methodology was worked out for the purpose of comparing the AWRE and KSC facilities using both arcs and rings experiments which included diagnostics, flyer configuration and specimen holding methods. KSC tested 18 3DQP arc samples and 1 3DQP ring from 50.8-cm diameter billets during this course of the program. After selection of comparable loading

conditions a combined response experiment using strain-gaged aluminum rings was accomplished with good correlation between the two agencies. The inadvertent use of material which behaved as "A" cycle indicated that magnetic flyer experiments were sensitive to porosity differences and can be used to detect production lot variations. Using comparable methods, the two facilities were able to produce the same damage modes to within 10 to 15% of the measured impulse.

PREFACE

This report describes the Facility Correlation and UGT Simulation Program conducted for DNA by Kaman Sciences Corporation. The work authorization was covered by DNA Contract DNA001-76-C-0359. The program was conducted under the direction of Mr. Donald Kohler, DNA.

It is a special pleasure to acknowledge the assistance and technical information forwarded over the years by AWRE personnel and, in particular, Mr. Angus MacAulay. In addition, KSC gratefully acknowledges assistance in this program from the following:

Southern Research Institute C. Pears and G. Fornaro	- Material properties and damage data
Air Force Weapons Laboratory D. Newlander	- Shock wave calculations and pulse shaping
Systems, Science & Software G. Gurtman	- Shock wave calculations and pulse shaping
T. McKinley	- Interpretations and suggestions

Companion reports are being prepared by these individuals to document their participation in this program as part of the DNA reporting system. Advantage was taken of the TINC hydrocode by S^3 to provide flyer pulse shaping guidance and predict the location and form of damage. Physical damage correlation was accomplished using methods developed by Southern Research Institute and KSC. A further correlation was accomplished by comparing ring strain gage records with the TWORNG ring response code. Other ring correlations are being reported by PDA.

The purpose of this program was to provide a laboratory method for verifying the x-ray hardness of 3-Dimensional Quartz Phenolic (3DQP) without recourse to underground testing.

A secondary purpose of the program was to determine whether the magnetic flyer technology developed at one facility could be applied to another. A cooperative program was instituted with the Atomic Weapons Research Establishment, Aldermaston, England, to conduct corresponding magnetic flyer experiments. Many innovative ideas passed back and forth which contributed to the success of this program. This report describes the initial effort, and later progress will be documented in subsequent reports by all participants.

Conversion Factors for U. S. Customary to Metric (SI) Units of Measurement.

To Convert From	To	Multiply By
angstrom	meters (m)	1.000 000 X E -10
atmosphere (normal)	kilo pascal (kPa)	1.013 25 X E +2
bar	kilo pascal (kPa)	1.000 000 X E +2
barn	meter^2 (m^2)	1.000 000 X E -28
British thermal unit (thermochemical)	joule (J)	1.054 350 X E +3
calorie (thermochemical)	joule (J)	4.184 000
cal (thermochemical)/cm^2	mega joule/m^2 (MJ/m^2)	4.184 000 X E -2
curie	giga becquerel (GBq)*	3.700 000 X E +1
degree (angle)	radian (rad)	1.745 329 X E -2
degree Fahrenheit	degree kelvin (K)	$t_k = (t° f + 459.67)/1.8$
electron volt	joule (J)	1.602 19 X E -19
erg	joule (J)	1.000 000 X E -7
erg/second	watt (W)	1.000 000 X E -7
foot	meter (m)	3.048 000 X E -1
foot-pound-force	joule (J)	1.355 818
gallon (U.S. liquid)	meter^3 (m^3)	3.785 412 X E -3
inch	meter (m)	2.540 000 X E -2
jerk	joule (J)	1.000 000 X E +9
joule/kilogram (J/kg) (radiation dose absorbed)	Gray (Gy)**	1.000 000
kilotons	terajoules	4.183
kip (1000 lbf)	newton (N)	4.448 222 X E +3
kip/inch^2 (ksi)	kilo pascal (kPa)	6.894 757 X E +3
ktap	newton-second/m^2 (N-s/m^2)	1.000 000 X E +2
micron	meter (m)	1.000 000 X E -6
mil	meter (m)	2.540 000 X E -5
mile (international)	meter (m)	1.609 344 X E +3
ounce	kilogram (kg)	2.834 952 X E -2
pound-force (lbf avoirdupois)	newton (N)	4.448 222
pound-force inch	newton-meter (N·m)	1.129 848 X E -1
pound-force/inch	newton/meter (N/m)	1.751 268 X E +2
pound-force/foot^2	kilo pascal (kPa)	4.788 026 X E -2
pound-force/inch^2 (psi)	kilo pascal (kPa)	6.894 757
pound-mass (lbm avoirdupois)	kilogram (kg)	4.535 924 X E -1
pound-mass-foot^2 (moment of inertia)	kilogram-meter^2 (kg·m^2)	4.214 011 X E -2
pound-mass/foot^3	kilogram/meter^3 (kg/m^3)	1.601 846 X E +1
rad (radiation dose absorbed)	Gray (Gy)**	1.000 000 X E -2
roentgen	coulomb/kilogram (C/kg)	2.579 760 X E -4
shake	second (s)	1.000 000 X E -8
slug	kilogram (kg)	1.459 390 X E +1
torr (mm Hg, 0° C)	kilo pascal (kPa)	1.333 22 X E -1

*The becquerel (Bq) is the SI unit of radioactivity; 1 Bq = 1 event/s.
**The Gray (Gy) is the SI unit of absorbed radiation.

A more complete listing of conversions may be found in "Metric Practice Guide (E 380-74)," American Society for Testing and Materials.

TABLE OF CONTENTS

TABLE OF CONTENTS (CONT'D)

LIST OF FIGURES

LIST OF FIGURES (CONT'D)

LIST OF FIGURES (CONT'D)

LIST OF FIGURES (CONT'D)

LIST OF TABLES

SECTION 1

INTRODUCTION

This report describes work performed by KSC in support of the Magnetic Flyer Correlation Program. The objectives of this program are as follows:

1. Correlate results from KSC and AWRE flyer plate facilities.

2. Define an above ground test which duplicates underground test damage.

3. Expand the 3DQP data base
   - higher impulse levels
   - porosity effects
   - combined response effects.

4. Establish 3D Quality Control (3DQC) procedures
   - analytics
   - NDM, NDT techniques
   - flyer plate loading.

The program was divided into two major parts, the Facility Correlation Study and the UGT Simulation STudy. For the Facility Correlation Study, impulse tests were conducted on 50.80-cm diameter 3DQP arc and ring materials selected from an AVCO cylinder originally believed to have been through the "C" process fabrication (as will be described, this material is now thought to be more characteristic of "A" process). This work has been completed and will be reported in its entirety.

For the UGT Simulation Study, impulse tests were conducted on samples similar to both AVCO "C" process fabrication materials and materials fielded underground. The sample dimensions were matched to those fielded underground, the rings and arcs being machined from a 19.6-cm diameter 3DQP cylinder. In total, KSC support for the Correlation of Simulation Testing and the UGT Simulation Study produced 31 damaged 3DQP arcs, 10 transmitted or front surface pressure-time waveforms, 3 3DQP ring shots instrumented with 10 strain gages, and approximately 60 calibration or correlation shots. Finally, numerous x-ray radiographs and ultrasonic measurements were made to support on-site evaluations of post-test sample evaluations.

KSC utilized its magnetically driven flyer plate facility to provide both comparative data for the AWRE equivalence program and as the technique for the AGT/UGT simulation of Ring Z, a ring damaged by UGT exposure. In-house damage assessments were accomplished using pre- and post-test radiographs, ultrasonic velocity and attenuation, post-test photomicroscopy, in addition to electromagnetic excitation (EME) testing to measure modulus. Considerable structural response correlations of measured strain traces were also accomplished to demonstrate an understanding of the simulation environment, the material condition and the resultant ring response.

Section 2 of this report presents a description of the impulsive load test techniques while Section 3 details the test matrix. Section 4 describes the experimental results obtained from the Facility Correlation Study and Section 5 the experimental results from the UGT Simulation Study while Section 6 gives the conclusions obtained for the Correlation of Simulation Testing Program.

SECTION 2

IMPULSIVE LOAD TEST TECHNIQUES

2.1 CAPACITOR BANK DESCRIPTION

The samples were tested in the Kaman 220-kilojoule magnetic flyer plate facility. This capacitor bank consists of 36 capacitors storing 220 kilojoules of energy at 45 kilovolts. The output parameters of the bank are several megamperes at a ringing frequency of 120 kilohertz. The electrical circuit consists of 36 capacitors, a Blumlein-triggered solid dielectric switch, and a flyer plate assembly. The discharge of the stored energy is initiated by a high voltage pulse induced into the solid dielectric switch to produce multiple current carrying channels. The discharging current produces a magnetic field which then produces an accelerating force on the flyer plate, itself a current carrying part of the circuit. The flyer plate is thus accelerated to a predetermined velocity, at which point it then strikes the target. The flyer plate velocity and, thus, the impulse is controlled by varying the width of the flyer plate, the flyer plate free run, and the stored energy in the capacitor bank. The post-test impact magnetic push is controlled either by the free run distance or by capacitor bank crowbar techniques.

2.2 FOIL CHOP TECHNIQUES

The initial phase of the Facility Correlation Study dictated that all of the momentum be delivered to the flyer plate prior to flyer plate impact. Thus, comparisons between the AWRE and KSC facilities could be accomplished in the most straightforward manner. To achieve this goal, the capacitor

bank discharge must be altered such that the post-impact push associated with a normal ringing discharge will be eliminated. The other alternative to foil choping would be to place the target at abnormally long free run distances. This would be an unacceptable solution due to flyer buckling considerations. As a result, foil chop methods were used to achieve the "sharp" impulse.

At the free run distances (2.54 mm) acceptable for proper flyer plate performance the bank needed to be disconnected extremely early in its discharge cycle. Through previous contact with AWRE, KSC was aware of foil chop techniques which could satisfy both the impulse and free run requirements. The technique has been referred to as dynamic damping and involves placing an exploding foil in series with the capacitor bank discharge circuit. After several trial shots, the technique was perfected and used almost without exception through the remainder of the Facility Correlation Study.

To demonstrate the repeatability of this foil chop technique, Table 1 lists the pertinent bank and flyer plate impulse data for 0.3-mm and 0.64-mm thick aluminum flyer plates. All data were taken at 2.54 mm free run distances. The current waveform produced by the discharge of the capacitor bank is shown in Figure 1. This waveform represents the average of all the shots performed around an impulse level of 8 kilotaps. The bars represent the total range of data, while the waveform is drawn through the average current value. These data are thought to be quite consistent.

The capacitor bank was operated in a second configuration to perform tests on the UGT Simulation Program. The early UGT analysis suggested that to deliver an impulse of 8 kilotaps prompt and 8 kilotaps post magnetic push to the sample would

TABLE 1 CAPACITOR BANK DISCHARGE PARAMETERS, ANALYSIS OF BANK PERFORMANCE, 0.3-mm AND 0.64-mm THICK AL FLYERS

SHOT #	FLYER THCK. (mm)		PEAK CURRENT mamps	SHARP IMPULSE kilotaps
2-290	0.64		1.67	8.0
2-291	0.64		1.67	8.0
2-292	0.64		1.63	7.9
2-296	0.64		1.61	7.2
2-297	0.64		1.61	8.3
2-300	0.64		1.64	8.1
2-304	0.64		1.69	8.6
2-323	0.64		1.61	7.9
2-324	0.64		1.65	8.4
2-325	0.64		1.60	7.8
2-326	0.64		1.65	8.4
2-327	0.64		1.65	8.4
2-328	0.64		1.64	8.3
		Mean	1.64	8.1
		1σdev	0.03	.4
		$\frac{1\sigma dev}{Mean}$	2%	5%
2-293	0.3		1.64	7.5
2-294	0.3		1.61	7.3
2-295	0.3		1.58	7.4
2-298	0.3		1.57	7.3
2-299	0.3		1.64	7.8
2-306	0.3		1.65	8.0
2-329	0.3		1.66	8.1
2-330	0.3		1.63	7.9
		Mean	1.63	7.7
		1σdev	0.04	.3
		$\frac{1\sigma dev}{Mean}$	3%	4%

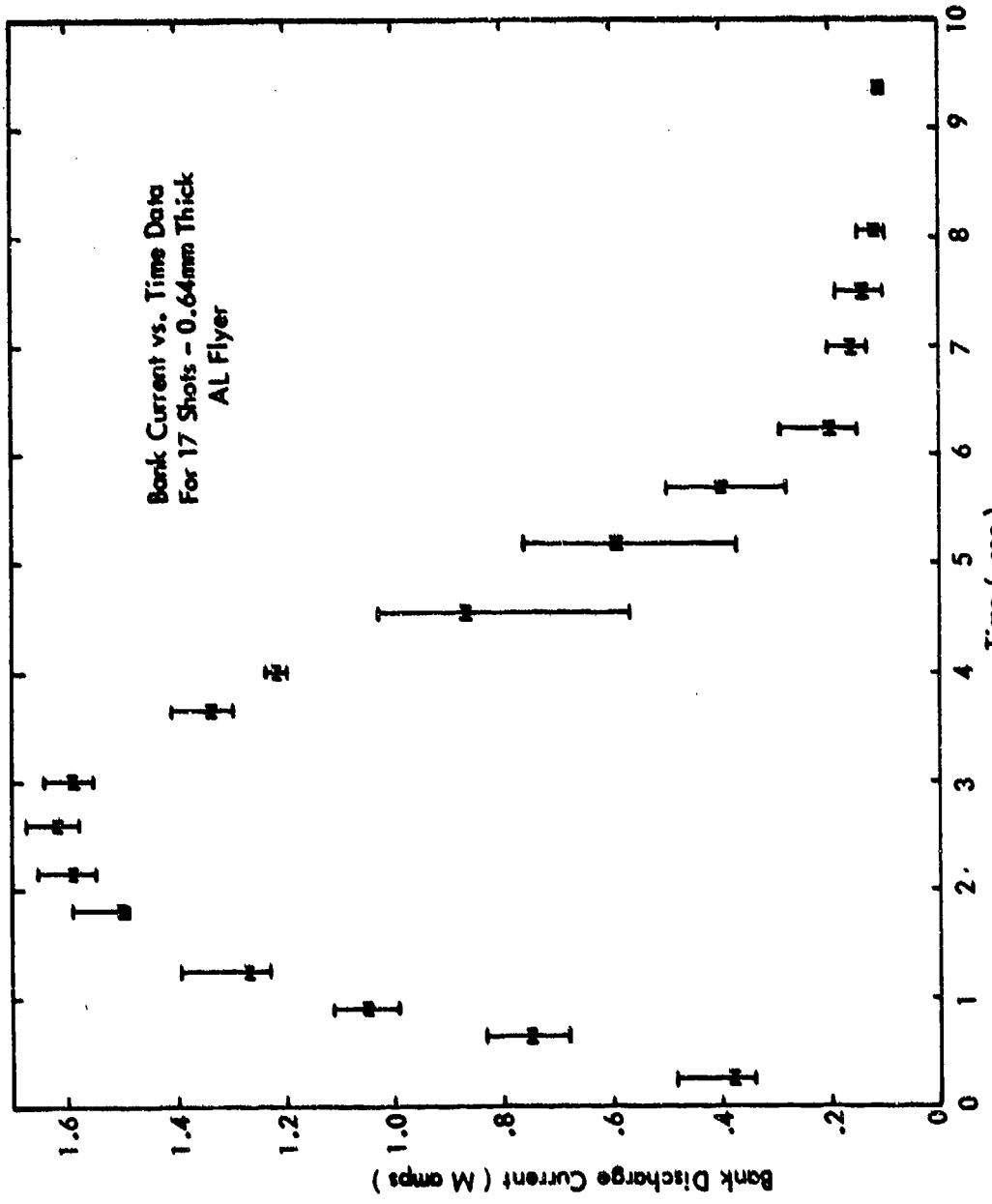

FIGURE 1 CAPACITOR BANK DISCHARGE CURRENT WAVEFORM

provide a duplication of the damage mode experienced underground. To achieve the 8 KT post-impact magnetic push at a reasonable flyer-target standoff distance, the capacitor bank discharge frequency was slowed by the addition of a ballast inductance. The resultant ringing frequency of the bank was approximately 60 kilohertz. This slower bank configuration, the second configuration used on the program to date, produced a dramatic simulation of the desired UGT damage mode (the details of these simulation shots will be report in Section 5, UGT Simulation Study Experimental Results).

The versatility of the KSC capacitor bank to impact a variety of impulsive loading conditions to the test samples has become an important development achieved in this program. Two unique bank configurations developed in this program, coupled with the normal ringing discharge technique, provides four testing options for above ground simulation of underground test impulse conditions. These options should result in improved simulation of loading conditions and the resultant stress wave damage modes which are found to occur underground. The circuit parameters used for these four capacitor bank configurations are outlined in Table 2.

2.3 FLYER PLATE DESCRIPTION

One of the most important items in obtaining good magnetic flyer experimental data is the quality control of the flyer plate assembly. Due to the criticality of the flyer assembly, Kaman has expended considerable effort to insure repeatability in each of the assembly steps. Flyer plate shape is established by a template which is designed and fabricated for each new test assembly. Each flyer plate is individually fabricated by a special process which enables the flyer plate to conform to the precise dimensions of the template with edges which are

TABLE 2 CAPACITOR BANK CONFIGURATIONS AND INDUCTANCE SCHEMES

BANK CONFIGURATION	PURPOSE	CROWBARRED	INDUCTANCE DISTRIBUTION			
			FLYER PLATE	BALLAST INDUCTANCE	BANK	TOTAL
Configuration 1	Normal Bank Discharge	No	4 nH	0	15 nH	19 nH
Configuration 2 Facility Correlation Study	Produce 8 KT Sharp Impulse	Yes	8 nH	0	15 nH	23 nH
Configuration 3 UGT Simulation Study	Produce 8/16 KT 8/16 w Long Magnetic Tail [1]	Yes	4 nH	12 nH	15 nH	31 nH
	8/16 w Shorter Magnetic Tail [2]	Yes	4 nH	12 nH	15 nH	31 nH
Configuration 4 UGT Simulation Study	8/16 w Shorter Magnetic Tail [2]	Yes	4 nH	81 nH	15 nH	100 nH

1. Long magnetic tails are produced by shorting crowbar techniques.
2. Shorter magnetic tails are produced by series foil chop crowbar techniques.

smooth and free of burrs, machine marks, etc. The flyer plate/insulation/backstrap layout is then assembled in a controlled environment such that dust particles are virtually eliminated. The repeatability on the overall assembly thickness is normally less than 0.0127 mm.

In these experiments flyer plates 7.62 cm wide were used to impact the arc and ring samples. All flyer plates were made from either 0.3-mm or 0.64-mm thick aluminum and were sized in length to load 160° of arc.

Initially, the flyer insulation/backstrap was fabricated flat and then curved to the proper radius before being placed in the massive aluminum backing block. The thicker 0.64-mm aluminum flyers did tend to lift, however, indicating that residual stresses had been built in during the assembly process. To overcome the flyer lift, the flyers were assembled over a curved mandrel, and then place in the aluminum backing block. Fabrication by this technique insured stress-free flyer assemblies, and the lift was eliminated.

2.4 MOMENTUM CALIBRATION

Of prime importance to the understanding of any flyer plate experiment is the knowledge of the flyer plate behavior. To meet this requirement, Kaman has developed a flyer plate diagnostic scheme capable of determining the imparted magnetically-derived momentum in a flyer plate experiment.

Kaman determines the flyer plate impulse versus capacitor bank voltage by means of a velocity measurement of a known mass density flyer plate. The basic measurement technique relies on a calibrated Rogowski coil to determine the "effective" current through the flyer plate. The time resolved

"effective" current is then used to input the computer code Veldet such that the flyer plate performance (displacement, velocity, and momentum density) can be determined. The momentum density at impact and at the end of current ring-down are obtained by this method.

The "effective" current calibration is determined from time-of-arrival measurements and correlated by flyer plate velocity measurements as derived from offset pin switch closures. These data have been previously correlated to within ±5% for a 5.59-cm wide flyer as shown in Figure 2. The pin switches (either shorting or PZT pins) for these experiments are monitored on high-speed oscilloscopes. The standard data display for these recordings includes a timing wave on each channel and a fiducial mark which is common to the Rogowski coil measurement of the bank current (Figure 3) and all pin switch records (Figure 4). The timing marks are used to calibrate the sweep speed of the oscilloscope beams on each test and the fiducial mark is utilized to establish a positive reference time between all events including the start of current flow from the capacitor bank. These data are used as input to the Veldet computer code. The Veldet output includes printouts of the time varying items of interest (current, displacement, velocity, etc.).

All shots documented in this report were conducted with a free-flying backstrap. Since all materials were fabricated as an arc or ring, the same load coil, with a free-flying backstrap, was used such that both sample geometries were tested under identical loading conditions.

The purpose of the free flight backstrap is to insure the free response of the rings tested in this program. As the impulsive load is applied, the ring surface begins to

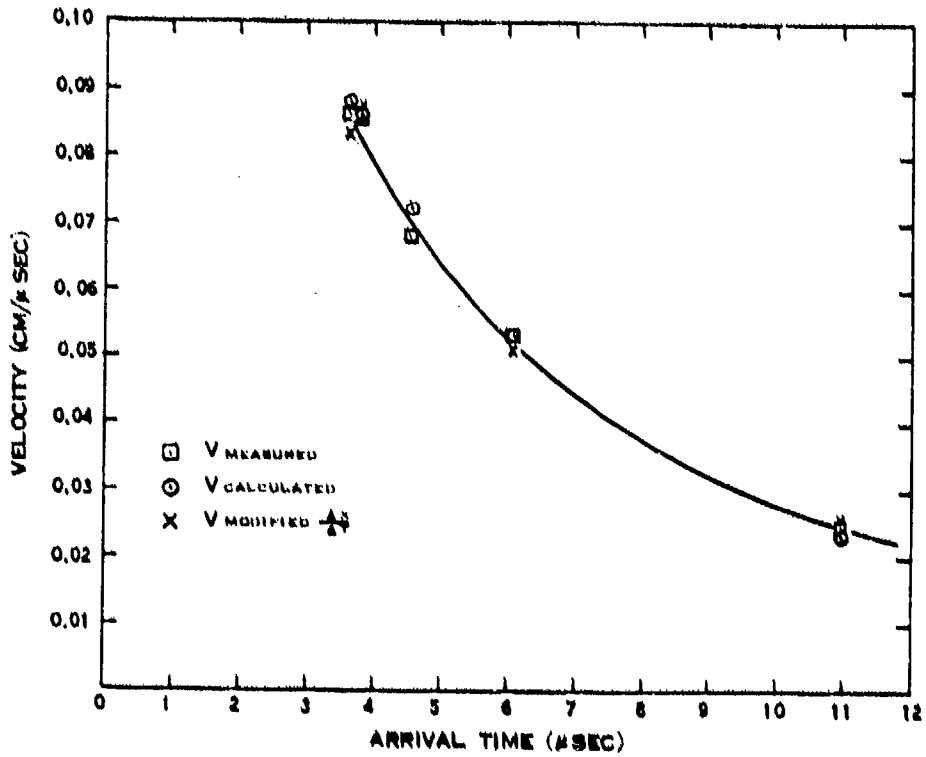

FIGURE 2 0°FLYER VELOCITY VS. ARRIVAL TIME (FLUSH AND OFFSET PIN SWITCH DATA)

FIGURE 3 CURRENT WAVEFORM RECORDING

FIGURE 4 OFFSET PIN SWITCH RECORDING

move radially inward and away from the flyer assembly at 0^{o}. Shortly afterwards the combined breathing and flexural response of the ring causes it to expand radially outward at $\pm 90^{o}$. The ring expands such that it impacts the load coil before the rigid body displacement can remove the ring from the load coil extremities. Structural response of the ring can be suppressed in addition to the point loading induced by the ring-coil impact.

Adiprene shock blocks 1.27 cm wide were placed around all samples in order to provide lateral constraints to effect a quasi-one-dimensional strain condition in the material during the initial shock wave transits. To the extent that the adiprene shock impedance matches that of the test sample, the effect of the adiprene shock blocks is to approximate a one-dimensional strain condition and suppress lateral release waves from traveling into the sample during the shock wave transits. The shock blocks also prevent undue side loads resulting from flyer plate edge curl. These shock blocks are also self-releasing from the arc holder such that the sample is released immediately upon flyer impact. These criteria are thought to be extremely important for prompt shock damage evaluation. The adiprene shock blocks were therefore used on both the arc and ring samples. The shock blocks used on the ring samples were of identical width as those used for the arcs. They extended around the ring such that 160^{o} of arc was subtended, protecting the ring from flyer edge curl, and were also self releasing from the ring. Small amounts of vacuum grease were used to join the shock blocks to either the arc or ring to insure intimate fit on all contact surfaces.

2.5 SAMPLE SUPPORT/RELEASE SCHEMES

The last eight arcs were impacted with the arc supported in an aperture plate. The arc sample, time of arrival pin, and the adiprene shock blocks were placed in the aperture of this fixture. The sample was then attached to the aperture plate by gluing small, hollow glass rods across the top and bottom of the adiprene shock blocks and also gluing the rods to the fixture. The glass rods provide enough support to hold the sample in the target holder without any sag; however, the shock pulse from the flyer impact shatters the glass and the arc sample is released after one shock wave transit time through the adiprene shock block thickness.

The arc holding scheme is devised so that the flyer-target spacing can be set very precisely. With the target placed on the flyer plate, six micrometer heads are used to raise the sample and aperture plate until the appropriate free run is attained. The proper orientation between the target surface and flyer surface is maintained by noting that the readings on the micrometer heads are identical.

The ring holding scheme uses many of the same principles developed for the arc holder. Glass rods are used to support the ring, and when these rods are impacted by the flyer, they shatter and release the ring. The ring-flyer plate spacing and orientation is controlled by exactly the same techniques described for the arc holding scheme.

2.6 INSTRUMENTATION AND DATA RECORDING

Current waveforms, time-of-arrival, sample velocity, arc sample pressure-time histories, and ring sample strain-time histories were recorded on this program. These parameters were measured to provide data for momentum calculations, for front surface and transmitted shock wave profiles, and for ring structural response calculations.

Carbon gages were used to record the near front surface signatures on lucite samples as well as the transmitted wave profiles at the rear surface of 3DQP arc samples. A Pulsar Instruments resistive gage power supply was used to excite the gages. The carbon gages were a special order Dynasen gage designed for use in magnetic field environments.

The Dynafax framing camera was used to record the displacement-time histories of the arcs after impact with the flyer plate. The lighting technique was a backlight scheme in which a floodlamp, through a Fresnel lens, shines directly into the objective lens of the camera. The arc interrupts the light as it flies across the field of view of the camera and the image is exposed on the film. Knowing the distance the sample travels during each frame of film, and knowing the time interval between frames, allows calculation of the late-time sample velocity. From the sample velocity the late-time impulse of the sample can be obtained.

An electronically integrated Rogowski coil is used to record the current waveform while time-of-arrival is measured with PZT pins.

All electronic instrumentation were recorded in an electrically isolated screen room. The isolation was obtained by lifting the double-walled screen room 6 inches off the floor

onto insulating pads and powering the recording instrumentation with a motor generator which is also electrically floating. The purpose of this elaborate isolation is to insure that the instrumentation sees a minimum of electromagnetic interference.

The current waveforms from the Rogowski coils and the pressure waveforms from the carbon gages were recorded on fast oscilloscopes, hand digitized using a traveling microscope, then submitted to Veldet and Mandat computer codes, respectively. These codes apply amplitude and time base calibrations to the current and pressure traces and then print and plot the data.

Table 3 presents a summary of the instrumentation and data recording techniques used on this program.

TABLE 3 INSTRUMENTATION AND DATA RECORDING TECHNIQUES

EVENT TO BE RECORDED	SENSOR	RECORDING INSTRUMENTATION	DATA REDUCTION PERFORMED
TOA	PZT Pins	Oscilloscopes	Hand digitize with traveling microscope, submit data to VELDET code to obtain TOA
Current Waveform	Rogowski Coil		Hand digitize with traveling microscope; submit data to VELDET or Mandat computer code to obtain calibrated current or pressure waveforms
Pressure Waveform	Carbon Gages		
Strain Waveform	Strain Gages	40 kHz bandwidth FM tape recorder	Analog-digital conversion at 2-μsec intervals
Free Flight Velocity	Dynafax Camera	Dynafax Camera	Read negative on film reader, submit data to code

SECTION 3

TEST MATRIX

A methodology was developed for accomplishing facility correlation and UGT simulation which includes detailed test matrices and material cutting diagrams. These matrices were draw up to identify the origin, purpose, and subsequent deposition of each test sample.

3.1 FACILITY CORRELATION STUDY MATERIAL CUTTING DIAGRAM

Material for the Facility Correlation Study was furnished by AWRE in the form of six rings cut from a 50.8-cm diameter cylinder of AVCO produced 3DQP. A cylinder cutting diagram is presented in Figure 5. Two of the six rings were cut into arcs, the remaining four rings divided equally between the KSC and AWRE facilities. Rings designated R3 and R4 were cut into 29 arcs each. The cutting diagram of these two rings is presented in Figure 6.

3.1.1 Facility Correlation Study Test Matrix and Material Description

The test matrix for the Facility Correlation Study was divided into four task areas. These tasks were:

TASK 1 Material Identification and Disposition

TASK 2 Flyer Plate Free Run Determination

TASK 3 Flyer Selection and 1-D Damage on 3DQP Samples

TASK 4 Combined Response Data

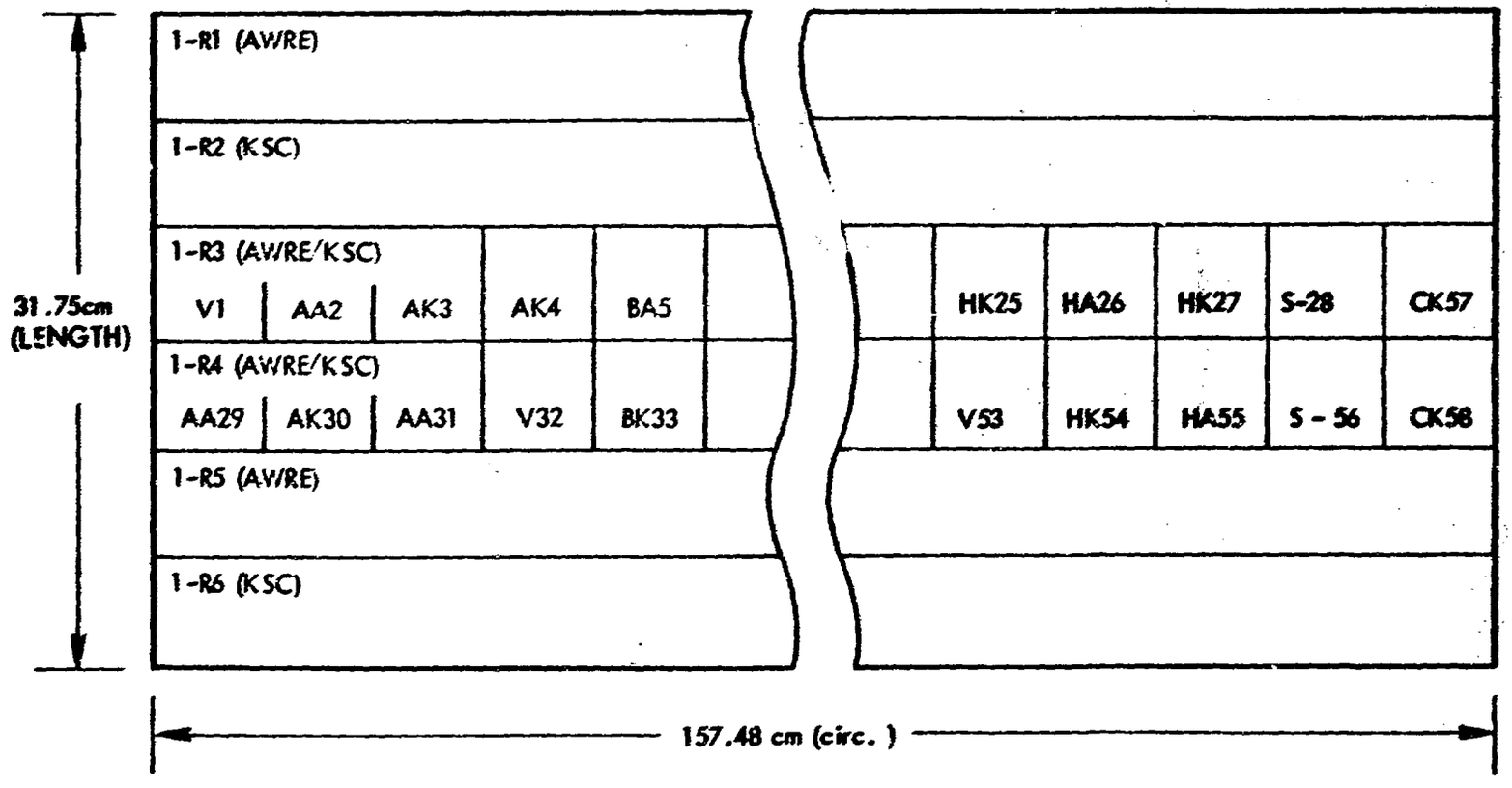

Extract 4 - 5.08cm wide x 1.27cm thick rings and 58 - 5.08cm x 5.08cm x 1.27cm arcs from cylinder.

FIGURE 5 50.8-CM DIAMETER CYLINDER CUTTING DIAGRAM

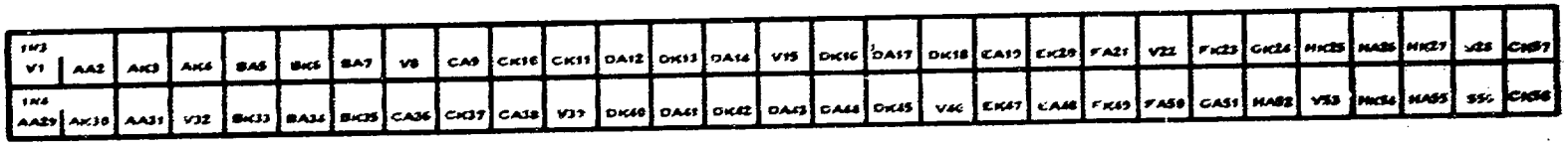

Extract 28 5.08 cm x 5.08 cm x 1.27 arc from each ring

FIGURE 6 50.8-CM DIAMETER RING CUTTING DIAGRAM

The arc and ring test samples allocated for each task are identified in Table 4.

3.2 UGT SIMULATION STUDY TEST MATRIX

The original test matrix is presented in Table 5. The necessary compliment of materials could not be supplied to complete this matrix in full, however. For this reason KSC only impacted 11 arcs and 2 rings in a successful attempt to duplicate the underground effects on Ring Z using advanced capacitor bank discharge techniques. Ring Z was a ring fielded in a known underground test environment and recovered such that its damage modes, damage locations, and early time strain signals were available for study and duplication.

TABLE 4. FACILITY CORRELATION STUDY MATERIAL ALLOCATION AND DISPOSITION.

TEST AGENCY	MATERIAL ALLOCATION				COMMENTS	SHIPPING INFORMATION
	TASK 1	TASK 2	TASK 3	TASK 4		
AWRE	V1,V8,V15,V22,V32, V34,V46,V53				Determine Virgin Properties	KSC to AWRE
SoRI	S28,S56				Determine Virgin Properties	KSC to SoRI
KSC	EME R1 thru R6; cut R3 & R4 into 58 arcs					KSC to Other Agencies
AWRE		1. 4 PMMA Arcs 2. 3 PMMA Arcs			1. Determine Front Surface Impact Conditions at 2.54 mm. Free run with Streak Camera. 2. Determine Front Surface Impact Conditions at 2.54 mm. Free Run with Carbon Gages.	None
KSC		1. 5 PMMA Arcs 2. 4 PMMA Arcs				None
AWRE			BA5,BA7,BA34,CA9, CA36,CA8,AA2, AA29, AA31 + 13 more available		1. Flyer Selection and 1-D Damage Shots. 0.3 mm and 0.64 mm thick aluminum flyer plates. 2. Flyer Selection and 1-D Transmitted Pressure Shots. 0.3 mm and 0.64 mm thick aluminum flyer plates.	1. KSC/AWRE to SoRI 2. SoRI make circ cut on arcs 3. SoRI retains 2.29 cm section of arcs 4. SoRI to AWRE, 2.54 cm arcs
KSC			BK6,BK33,BK35, AK3,AK4,AK30, CK57,CK58,GK24, HK25,CK11,CK37, DK13,DK16,DK18, DK42,DK45,DK40, + 3 more available			
AWRE			E48			AWRE retain all arcs
KSC			FK47,CK10,FK23, FK47			KSC arcs to SoRI
AWRE				1 aluminum ring; 2 3DQP ring and 2 other aluminum rings available	Combined response determination. 0.64 mm thick aluminum flyer plates	AWRE to ship 3DQP ring to SoRI
KSC				3 aluminum rings + 1 3DQP ring have been hit; 1 3DQP ring available		KSC ship 3DQP ring to SoRI

CONFIDENTIAL

TABLE 5 UGT SIMULATION STUDY TEST MATRIX AND MATERIAL REQUIREMENTS

AGENCY	RINGS, ARCS/AGENCY	PURPOSE	ARC THICKNESS
AWRE/SoRI	3	Virgin Properties	1.39 cm
AWRE/KSC	11 { 6 Magnetic Pressure 5 Arc Cushion	Loading Effects on Damage	1.39 cm
AWRE/KSC	5 { 3 Damage 2 Pressure	Damage and Load Verification	1.39 cm 0.76 cm
AWRE/KSC	2	Combined Response	1.39 cm

MATERIAL REQUIREMENTS

LOCATION	DATE REQUIRED	MATERIAL REQUIRED	PURPOSE	MATERIAL THICKNESS
KSC	1/77	1 Ring	Has Been Cut Into 14 Arcs	3.81 cm
AWRE	5/77	{ 1 Ring 1 Ring	Cut Into 14 Arcs	3.81 cm 5.72 cm
AWRE	5/77	4 Rings	4 Rings	3.81 cm

SECTION 4

FACILITY CORRELATION STUDY EXPERIMENTAL RESULTS

4.1 TASK 2 - FLYER PLATE FREE RUN DETERMINATION

The final determination of the flyer plate free run was accomplished by negotiation on the capabilities and test philosophy of the two facilities involved. KSC has historically preferred short free runs to minimize flyer plate buckle and air cushion enhancement while AWRE has traditionally used longer free runs. In short, the free run distance was simply negotiated to be 2.54 mm. Tests were conducted by KSC using streak camera techniques and front surface carbon gages to determine the impact characteristics of both 0.3-mm and 0.64-mm thick aluminum flyer plates at the 2.54-mm free run distance. These data are reported.

4.1.1 Streak Camera Records on PMMA

PMMA arc samples were fabricated to the dimensions of the 50.8-cm diameter 3DQP arc samples and then vapor coated with aluminum to accomplish 5 streak camera measurements. The purpose of these streak camera measurements was to determine the degree of flyer plate buckle. The streak camera technique used to record the flyer plate impact relies on the optical principle that certain materials lose their reflectivity when shock loaded; both aluminum and PMMA possess this property. A streak camera was used to record the light turn off as a result of the flyer plate striking the target. A PMMA target is shown in Figure 7 while the optical test setup is shown in Figure 8.

The results of the streak camera work at the chosen free run of 2.54 mm showed that the 0.3-mm thick aluminum flyer had approximately a 50 nanosecond closure across the 5.08 cm

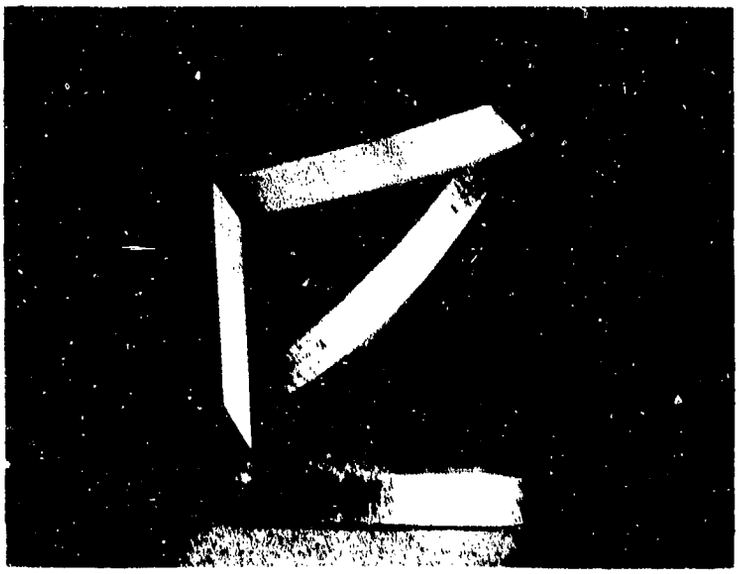

View of Impact Surface of Aluminum Vapor Deposited PMMA Samples

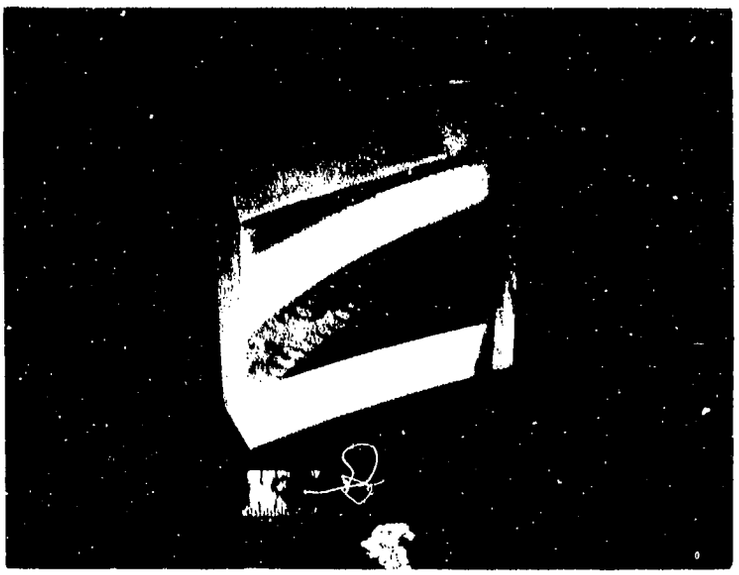

View Through Rear Surface of Aluminum Vapor Deposited PMMA Samples

FIGURE 7 PMMA TARGET FOR STREAK CAMERA MEASUREMENT OF FLYER IMPACT

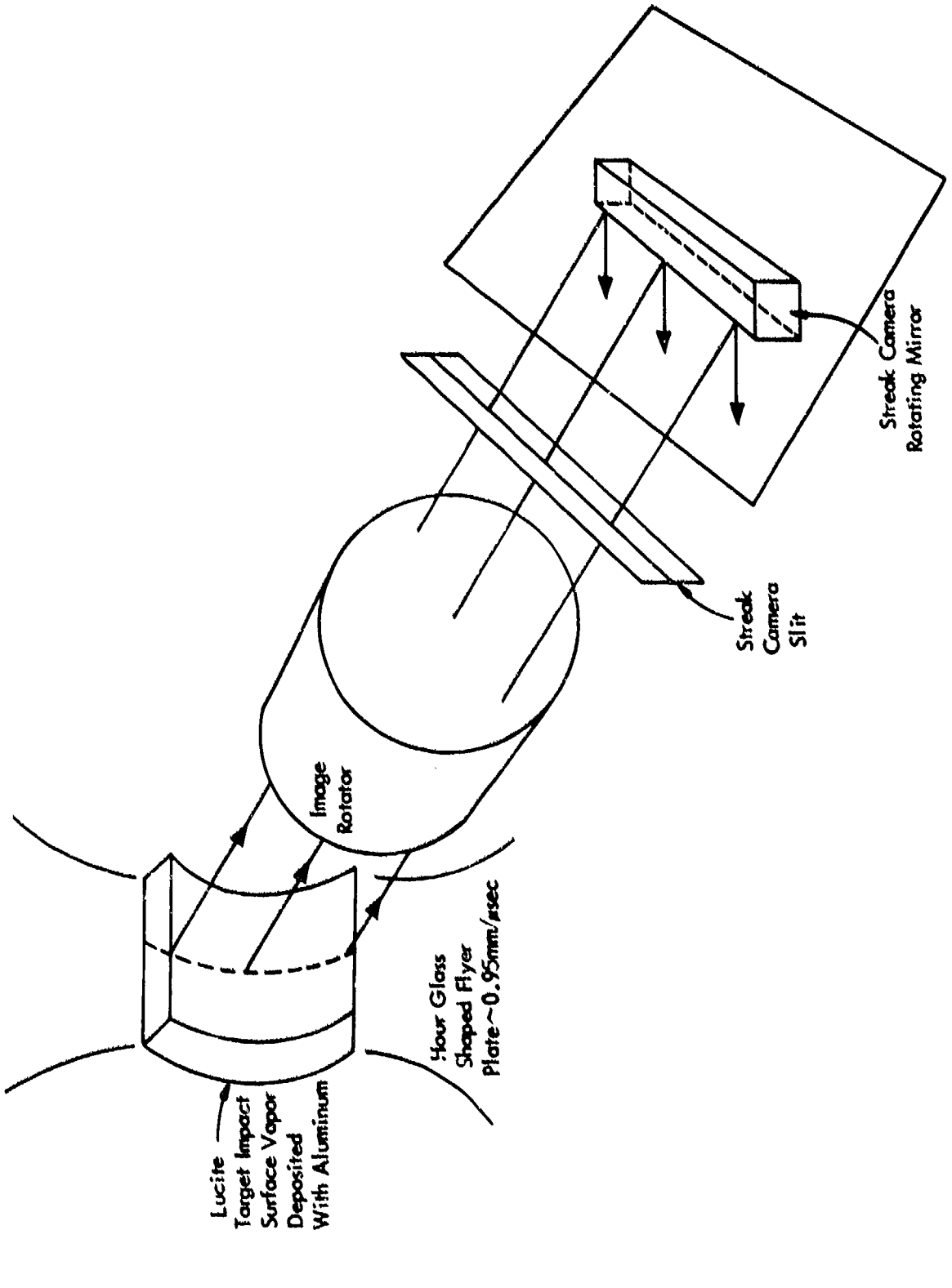

FIGURE 8 STREAK CAMERA OPTICAL SETUP

length sample. The 0.64-mm thick aluminum flyer, however, showed erratic impact behavior. Both the closure time across the PMMA sample and the spatial distribution of the impact varied from shot to shot. For example, the closure time ranged from 75 to 750 nanoseconds while the spatial pattern was completely random. Table 6 lists the impact parameters as measured by the streak technique. Figure 9 is a representation of the time and spatial coordinates of the flyer impact. Figure 9 is not an exact representation of the flyer plate impact because quantitative data reduction techniques could not be utilized on the low contrast streak camera film records; it is thought that this figure presents a fair representation of the lay down of the 0.64-mm thick aluminum flyer plate against the PMMA target, however, since a great deal of care was taken to show the trend of the data.

In order to estimate the effects of a non-planar impact using the 0.64-mm thick aluminum flyer plate against 3DQP, KSC made the following judgments: If the flyer plate were to average 500 nanoseconds non-planar impact, then the initial shock front would travel a distance less than a cell depth into the 3DQP material before the latest shock pulse was initiated at other locations on the impact surface. If the distance between the leading and trailing portions were 1.27 cm or more apart, then the 500 nanosecond asimultaneity would be spread over several cell widths. The shock pulse entering the 3DQP could be postulated as a uniform pressure over several cell widths and less than one cell depth into the 3DQP material. Though not totally comfortable with this reasoning, the 0.64-mm thick aluminum flyer could be judged marginally acceptable for the Facility Correlation Study. One must be careful, however, to hastily apply these results to the UGT Simulation Study since the small radius of curvature used for the UGT Simulation Program may well serve to degrade even further the marginal results of the 0.64-mm thick aluminum flyer plate.

TABLE 6 SUMMARY OF STREAK CAMERA MEASUREMENTS FLYER PLATE IMPACTS ON PMMA TARGETS

SHOT #	FLYER THCK. (mm)	FLYER FREE RUN (mm)	ESTIMATED FLYER CLOSURE PEAK TO VALLEY TIME[1] (nanoseconds)	ESTIMATED FLYER CLOSURE PATTERN PEAK TO VALLEY DISTANCE[1] (mm)
2-231	0.64	2.54	750	26.7
2-232	0.30	2.54	50	6.4
2-233	0.64	2.54	75 350	12.1
2-234	0.64	2.54	1050	33.0
2-235	0.64	2.54	450	14.6

PLOT OF DATA PRESENTED IN TABLE 6

- Four 0.64-mm thick 1100-0 Al Flyer Plates
  One 0.3-mm thick 1100-0 Al Flyer Plate
- 2.54-mm Flyer Plate Free Run
- 8000-fap Flyer Plate Impulse

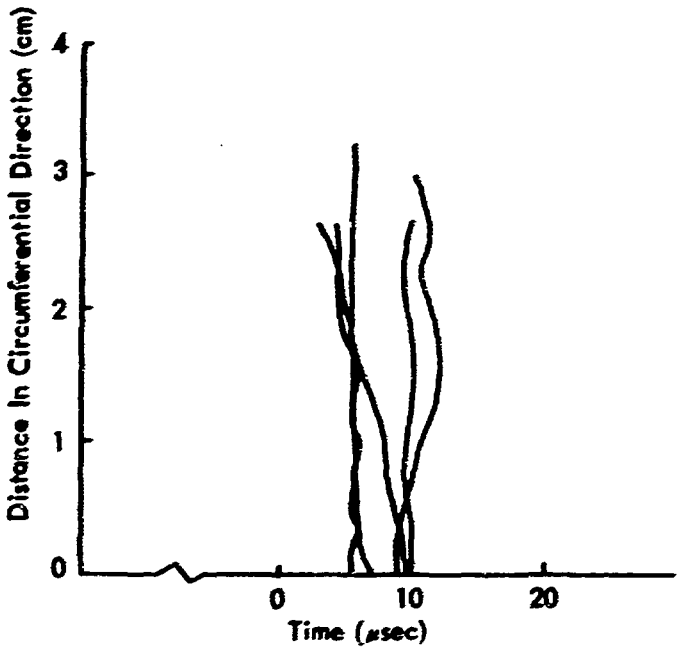

FIGURE 9 REPRESENTATION OF FLYER PLATE IMPACT CHARACTERISTICS AS DETERMINED BY STREAK CAMERA DIAGNOSTIC

CONFIDENTIAL

4.1.2 Front Surface P-t Records on PMMA

Four shots were performed with a number of carbon gages placed on the front surface of PMMA targets fabricated to the 50.8-cm diameter dimensions of the 3DQP samples. The reasons for placing the gages on the front surface of PMMA were to

1. Measure any discernable flyer plate buckle
2. Measure any discernable air cushion momentum enhancement.

All four shots were performed with 0.64-mm thick aluminum flyer plates. The free run standoffs were varied, however, the first two shots being performed at 1.27 mm and the latter two at 2.54 mm distance, respectively. These distances allowed a cursory examination of the effects of free-run distances on flyer plate buckle or air curshion. The placement of the carbon gages on the PMMA samples is shown in Figure 10.

The results of the front surface carbon gage shots are presented in Table 7. The front surface pressure-time historics are presented in Figures 11 through 14. As can be seen from comparison of the measured and calculated peak pressure columns from Table 7, the impact pressure measured with the carbon gages seems in agreement with theory. The calculation ignores air cushion. Since the other measured peak pressures seem to match the calculated values, these data seem to indicate that the air cushion does not affect peak pressure.

A thought to the contrary would be that since the gages are placed directly on the front surface of the lucite, then they protrude approximately 0.127 mm in front of the lucite

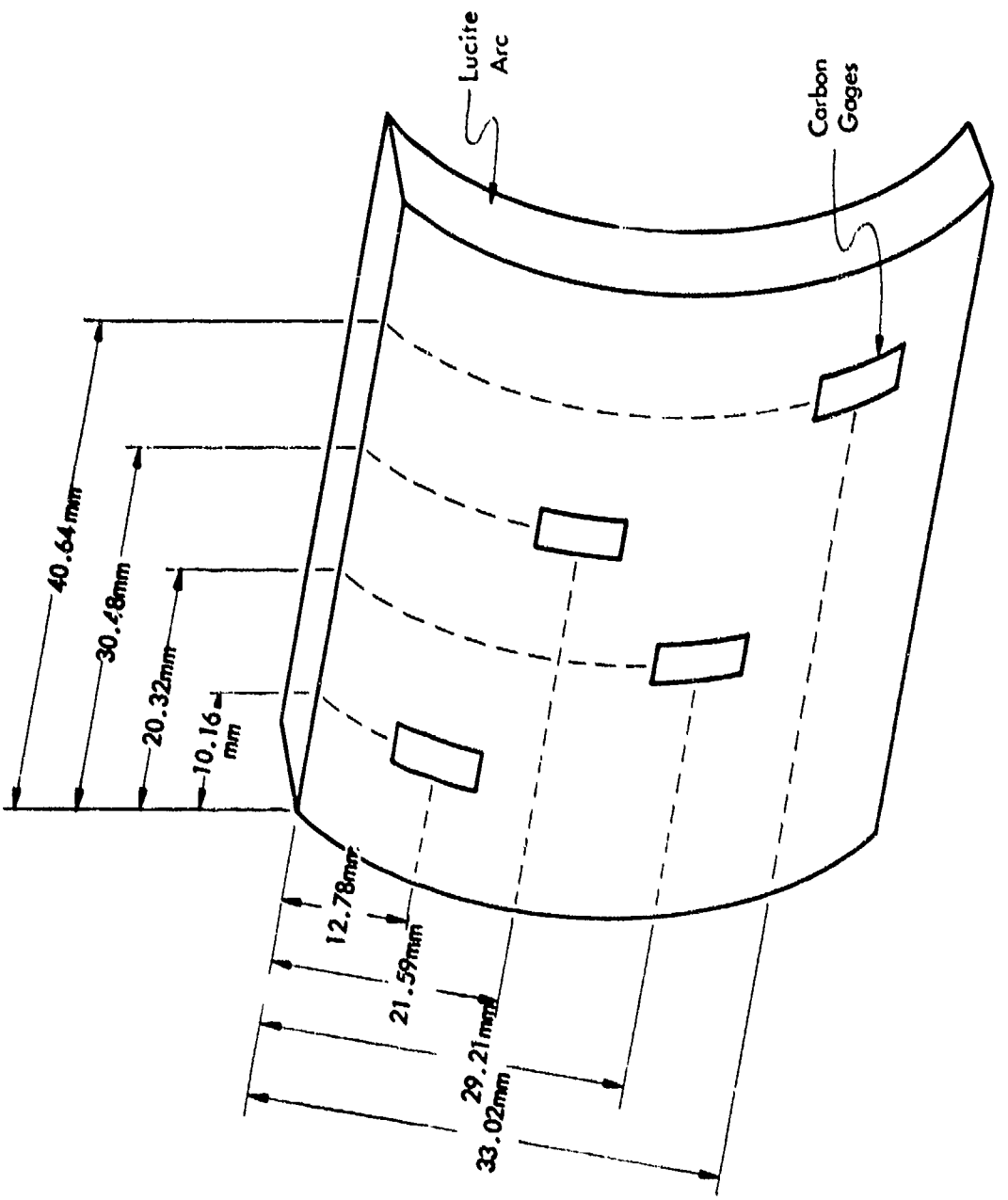

FIGURE 10 FRONT SURFACE PRESSURE MEASUREMENT GAGE GEOMETRY

TABLE 7 SUMMARY OF FRONT SURFACE CARBON GAGE MEASUREMENTS ON PMMA TARGETS

SHOT/GAGE #	FLYER PLATE THICKNESS (mm)	FREE RUN DISTANCE (mm)	PEAK PRESSURE (kilobars)		MOMENTUM (kilotaps)		
			GAGE	CALCULATED	VELDET[1]	VELDET[2] AIR CUSHION	GAGE
2-209							
1	0.64	1.27	12.6	12.8	7.4	8.0	9.0
2			14.0				10.5
2-210							
1			14.3*				7.3
2	0.64	1.27	16.5*	12.5	7.4	8.0	8.6
3			----				8.7
4			14.9*				---
2-211							
1			14.5*				
2	0.64	4.06	18.4*	13.2			8.2
3			----		7.5	9.1	8.8
4			----				---
2-212							
1	0.64	4.06	13.8	13.2	7.5	9.1	8.7
2			14.8				---

[1]This momentum value includes flyer plate + post-impact magnetic push impulse.

[2]The air cushion value is taken from the aluminum/3DQP impacts and is, therefore, not a measured value for aluminum/PMMA impacts.

CONFIDENTIAL

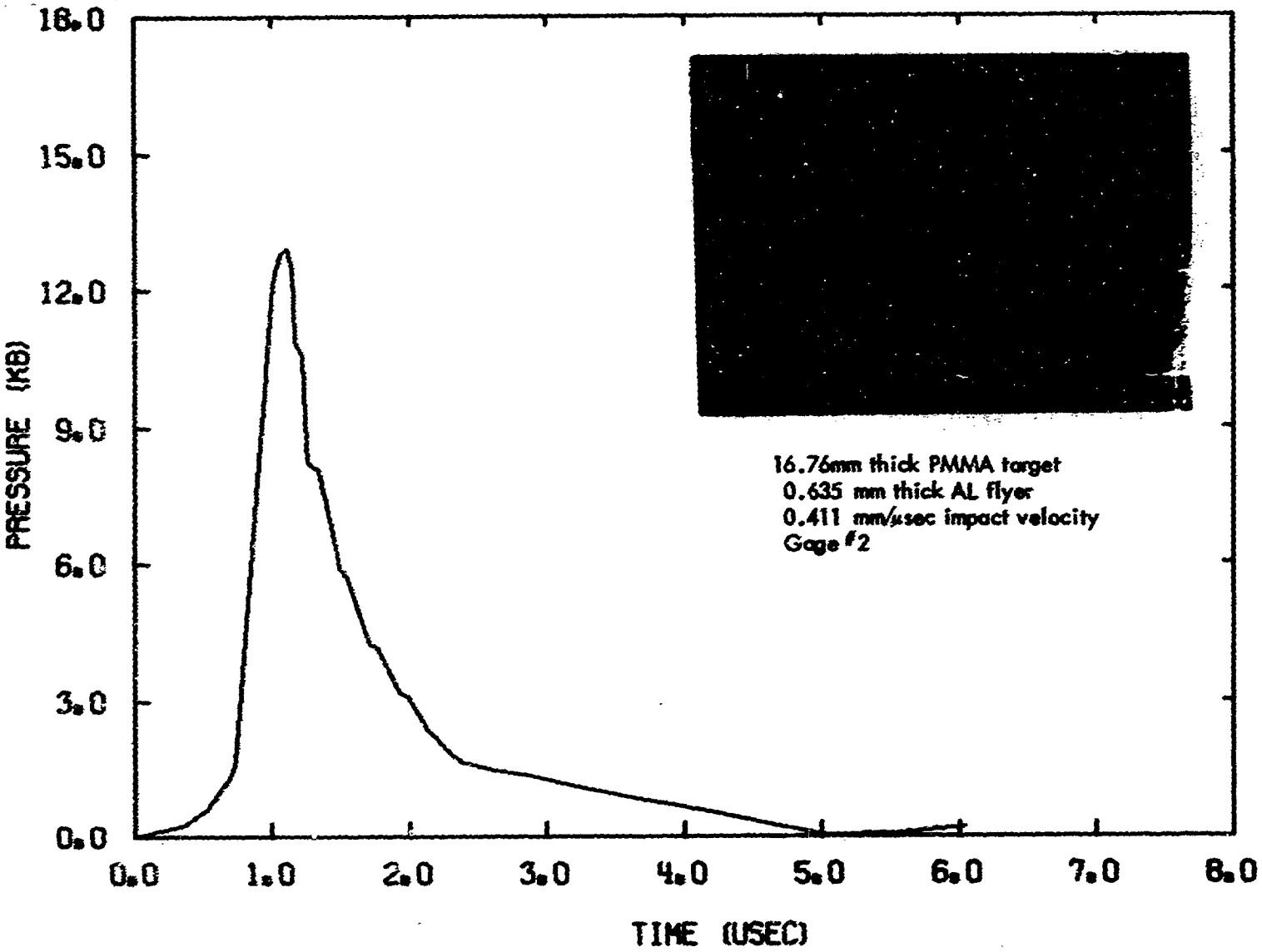

FIGURE 11 CARBON GAGE RECORD OF FRONT SURFACE PRESSURE FOR SHOT 2-209

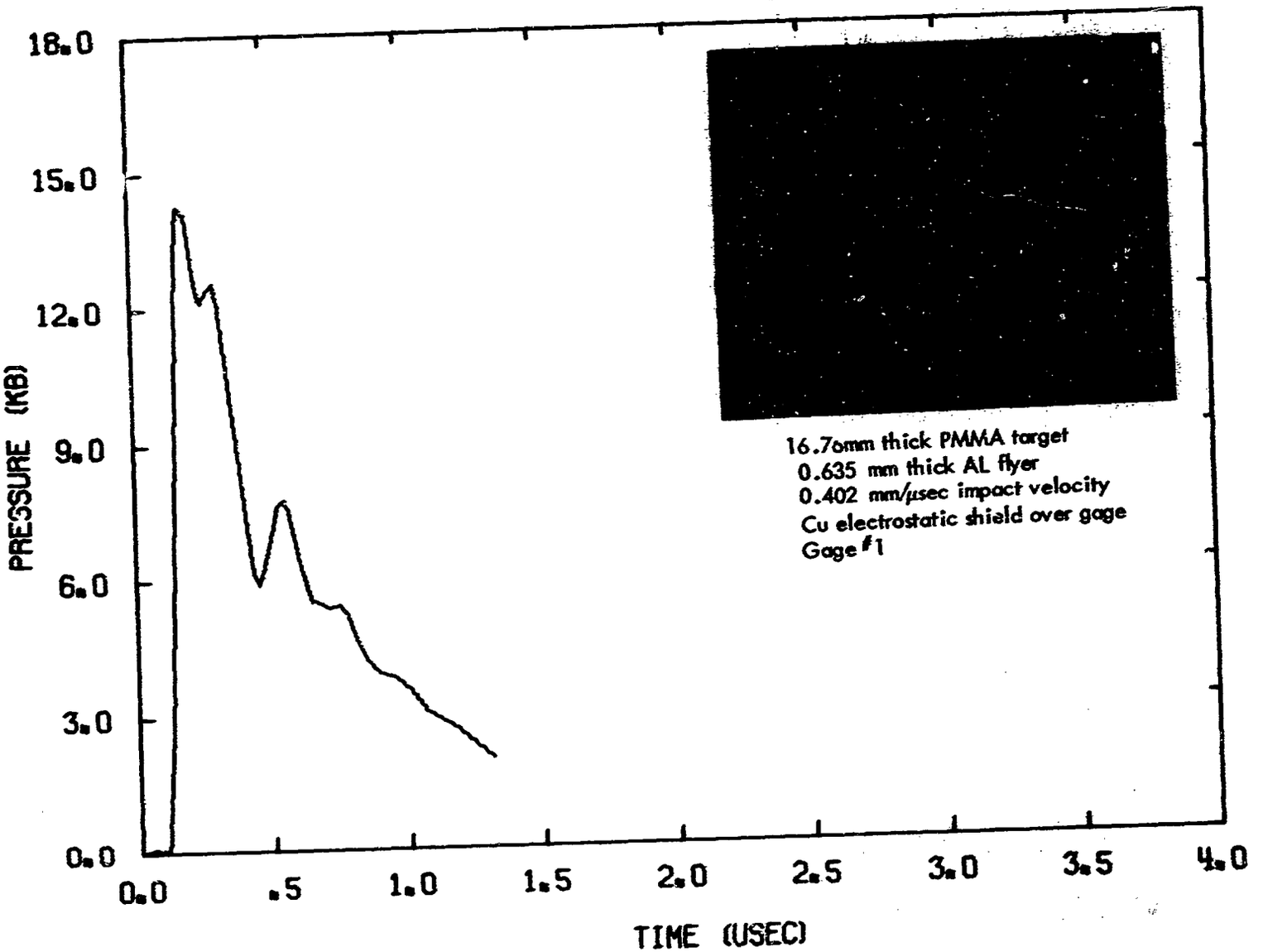

FIGURE 12 CARBON GAGE RECORD OF FRONT SURFACE PRESSURE FOR SHOT 2-210

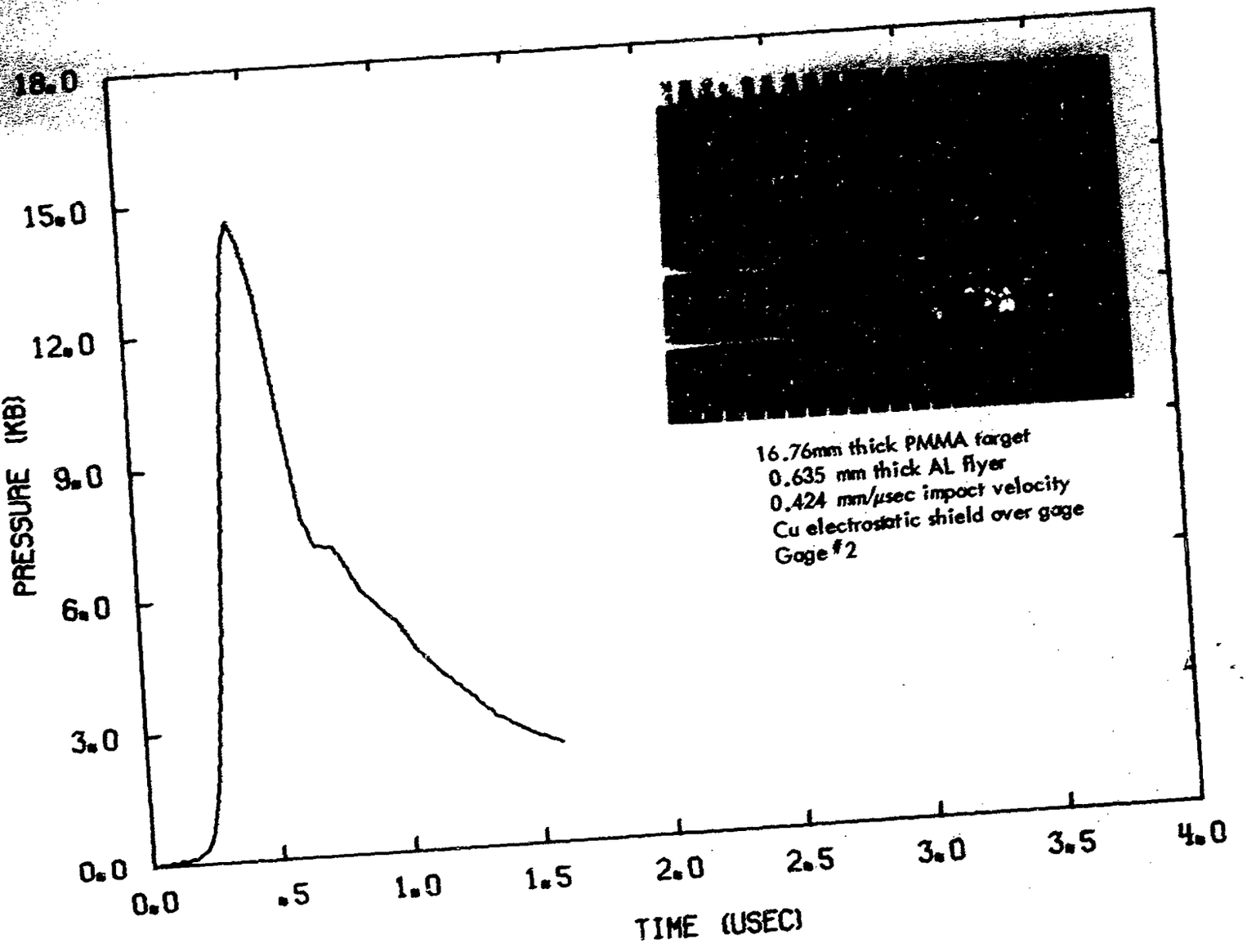

FIGURE 13 CARBON GAGE RECORD OF FRONT SURFACE PRESSURE FOR SHOT 2-211

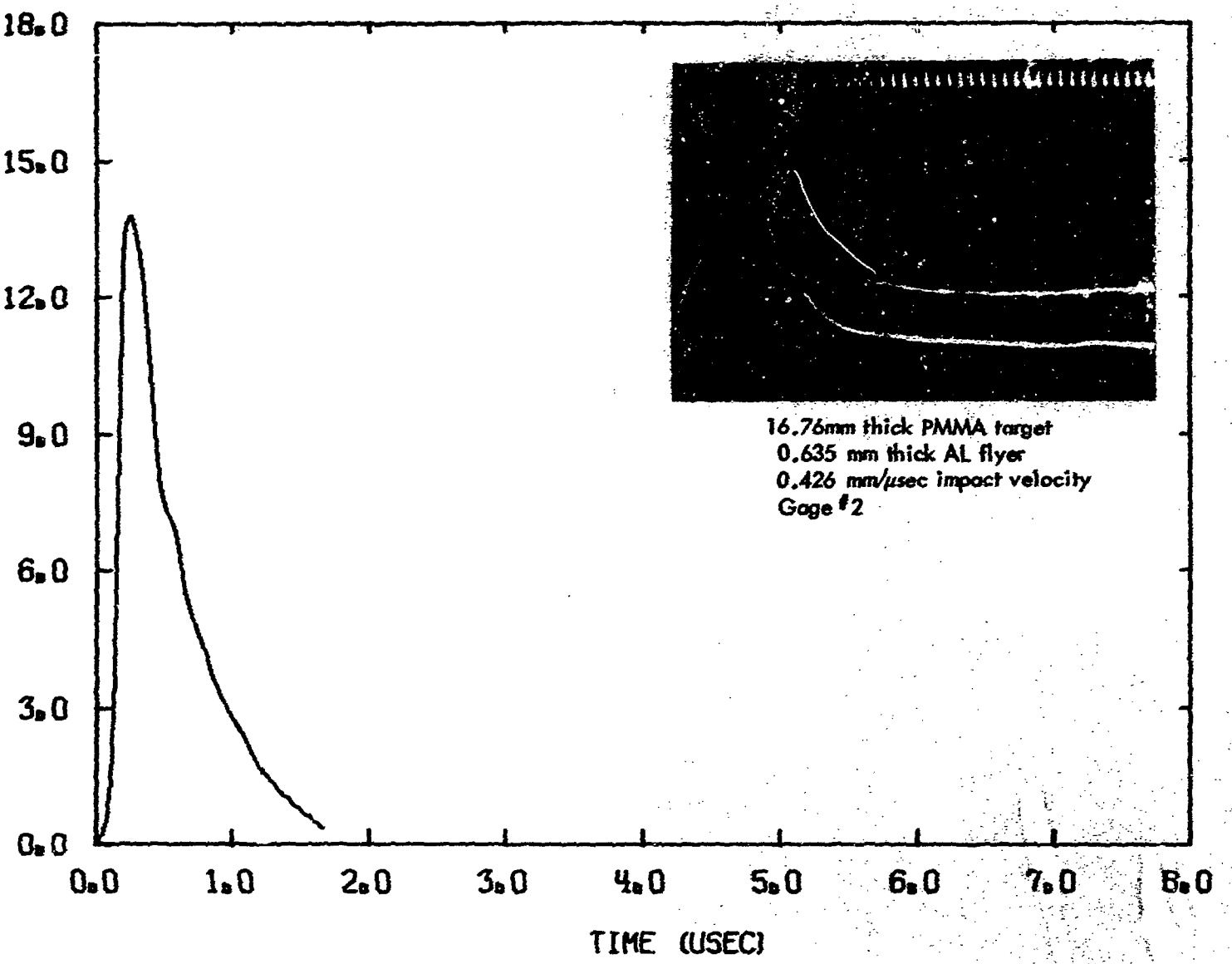

FIGURE 14 CARBON GAGE RECORD OF FRONT SURFACE PRESSURE FOR SHOT 2-212

surface allowing the air to rush off the gage surface as the flyer approached. If the air could escape prior to impact, then the measured and calculated values should indeed match because an air layer would not exist between the flyer and the gage surfaces. To check this theory a WONDY code calculation was made for an 0.64-mm thick aluminum flyer traveling at 0.047 mm/μsec with 8 kilotaps flyer plate impulse. The computer runs were made for both 1.27 mm and 4.05 mm free run distances and the predicted P-t waveforms are shown in Figure 15. The predicted stress-time waveform for both free-run distances were almost identical and were in quite good agreement with shot 2-212, in addition. From these data, one could conclude that the free-run distance does not significantly alter the front surface pressure-time waveforms seen by the target. Since the WONDY calculation also matched shot 2-212 experimental data, one might conclude that the air did not rush past the carbon gage and, therefore, that the experimental reading measured on shot 2-212 included the effects of air cushion.

A final thought concerning the front surface pressure measurements is that while the peak pressure recorded by the gage agreed nicely with various anlaytical predictions of peak pressure, the integrated momentum from the pressure measurement did not typically agree with either the flyer momentum or the flyer momentum added to the apparent air cushion momentum. This trend has been seen by KSC when using carbon gages to measure pressure-time waveforms. Since the peak pressure measured usually agrees with the analytical predictions, both the experimental test configuration and the impact planarity of the flyer against the gage surface is assumed to meet the necessary standards to properly record the pressure-time waveform. Again, however, even when the proper experimental standards seem to have been met, often

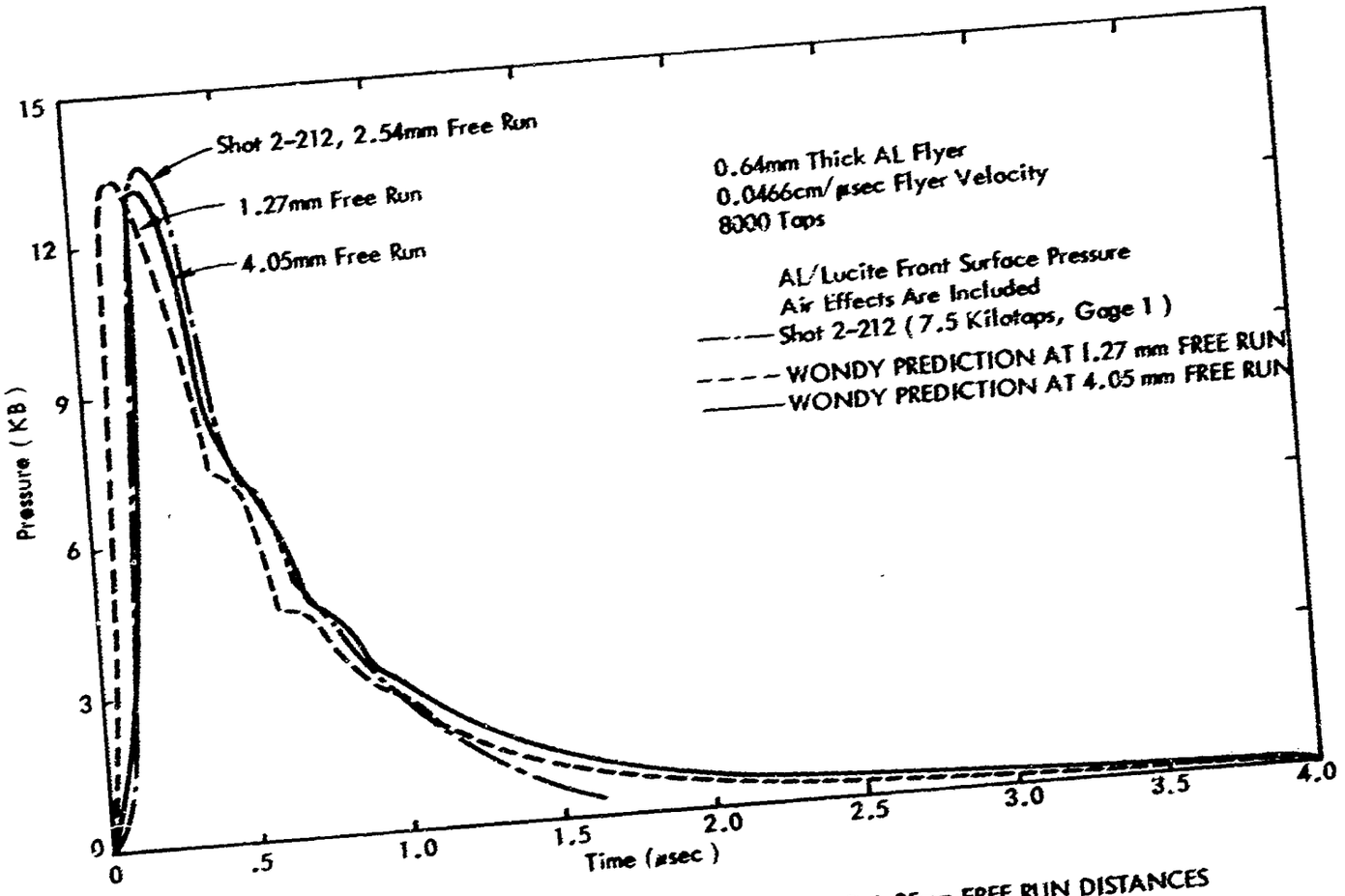

FIGURE 15 FRONT SURFACE P-T CALCULATION FOR 1.27mm AND 4.05mm FREE RUN DISTANCES OVER PLOTTED AGAINST CARBON GAGE DATA FROM SHOT 2-212

the integrated momentum of the waveform is measured too high. A thorough explanation for this fact cannot be offered at this time.

4.2 TASK 3: FLYER SELECTION AND 1-D DAMAGE ON 3DQP SAMPLES

4.2.1 Flyer Selection

The 0.64-mm thick aluminum flyer plate was chosen as the flyer which would be used for the Facility Correlation Study testing. Several shots were performed with 0.3-mm thick aluminum flyers, but it was mutually agreed that this flyer would melt at impulse values above 10-12 kilotaps. For this reason, it was futile to suggest that either the Facility Correlation Study or the UGT Simulation Program should be strongly tied to this particular flyer. Several shots were performed with the 0.3-mm thick flyer, however, and relatively strong differences can be shown between sample damage obtained with this flyer and damage caused by 0.64-mm thick flyer plate. These data will be reported in Section 4.2.3, 3DQP Arc Shots.

4.2.2 Momentum Verification

An objective of this program is the correlation between the KSC and AWRE magnetically driven flyer plate facilities. Paramount to this correlation is the accuracy of the impulse values delivered to the test samples. KSC has undertaken an examination of the test techniques used by our facility to determine the impulsive load value. The results of the examination were that independent measurements made on each and every shot provided the most accurate assessment of the final impulse value. These independent measurements provide a cross-check against which the other diagnostics can be compared; major differences between any of the techniques, of course, raises concern about the accuracy of the experiment.

Two independent impulse diagnostics[1] were conducted on each and every shot for this program. These diagnostics were:

1. Veldet Impulse - Calibrated Rogowski Coil
2. Time of Arrival Impulse - TOA Pin Mounted to Sample.

A third technique, a streak camera measurement of the flyer plate velocity, was performed on two shots. The results are that each of these diagnostics are in agreement with one another to better than ±7.5% for the 0.64-mm thick aluminum flyers used as the primary flyer for both the Facility Correlation Study and the UGT Simulation Study.

An important diagnostic of the Veldet technique is the measurement of the current waveform and, through a calibration factor, a calculation of the peak current can be made. As has been described in Table 1 and Figure 1, Section 2.2 of this report, the scatter in the peak current measurement was only ±2%, while the scatter in the impulse was only ±5%. Because extra care was taken to make the capacitor bank operate in a repeatable manner, both the peak current and the Veldet impulse made a consistent set of data.

The time of arrival pin technique is an independent check on the Veldet impulse. Rather than relying on a calibrated current waveform to determine impulse, the TOA pin technique relies on making a measurement of the position of the flyer plate during its flight to impact the sample (for simplicity, the pin is supported on the side of the sample, its sensing element located at the impact plane of the target and flyer plate). Time-of-arrival of the flyer plate at a known distance in space is a single valued function of the flyer plate impulse. Therefore, this measurement provides an

independent determination of impulse. Figure 16 presents the TOA impulse plotted against the Rogo impulse. If the two techniques produced exactly the same impulse values, then all the data points would fall on a 45° line. As can be discerned from this plot, the TOA impulse and the Rogo impulse for 0.64-mm thick aluminum flyer agree to better than ±7.5% for 11 of the 13 data points. This agreement between the two independent impulse diagnostic techniques is thought to be good. The agreement between the TOA impulse and Rogo impulse for the 0.3-mm thick aluminum is not as good, ranging from +7.5% to +11%. This bias is believed to be due to excessive edge effects associated with the thinner flyer.

A streak camera measurement was made to determine the flyer plate impulse for both a 0.3-mm and 0.64-mm thick flyer in order to compare a third diagnostic against the Veldet impulse technique. The streak camera technique yielded data which agreed with the Veldet technique to better than ±5%. These streak camera data are overplotted against the Rogo impulse and TOA impulse data presented in Figure 16. The streak camera data is another independent measurement of flyer plate impulse which correlated well with the Veldet technique. The agreement of this impulse diagnostic in addition to the other two diagnostics is thought to verify the overall accuracy of the impulse to ±7.5%.

The two streak camera measurements were made by watching the motion of the image of a wire suspended above the moving flyer. The streak camera photographs are shown in Figure 17. The digitized records for these photographs are shown in Figures 18 and 19. A least-squares fit to the digitized data yielded a cubic equation describing the distance-time points of the flight of the flyer plate. The slope of this equation, evaluated at 2.54 mm, yielded the velocity and thus the impulse of the flyer plate.

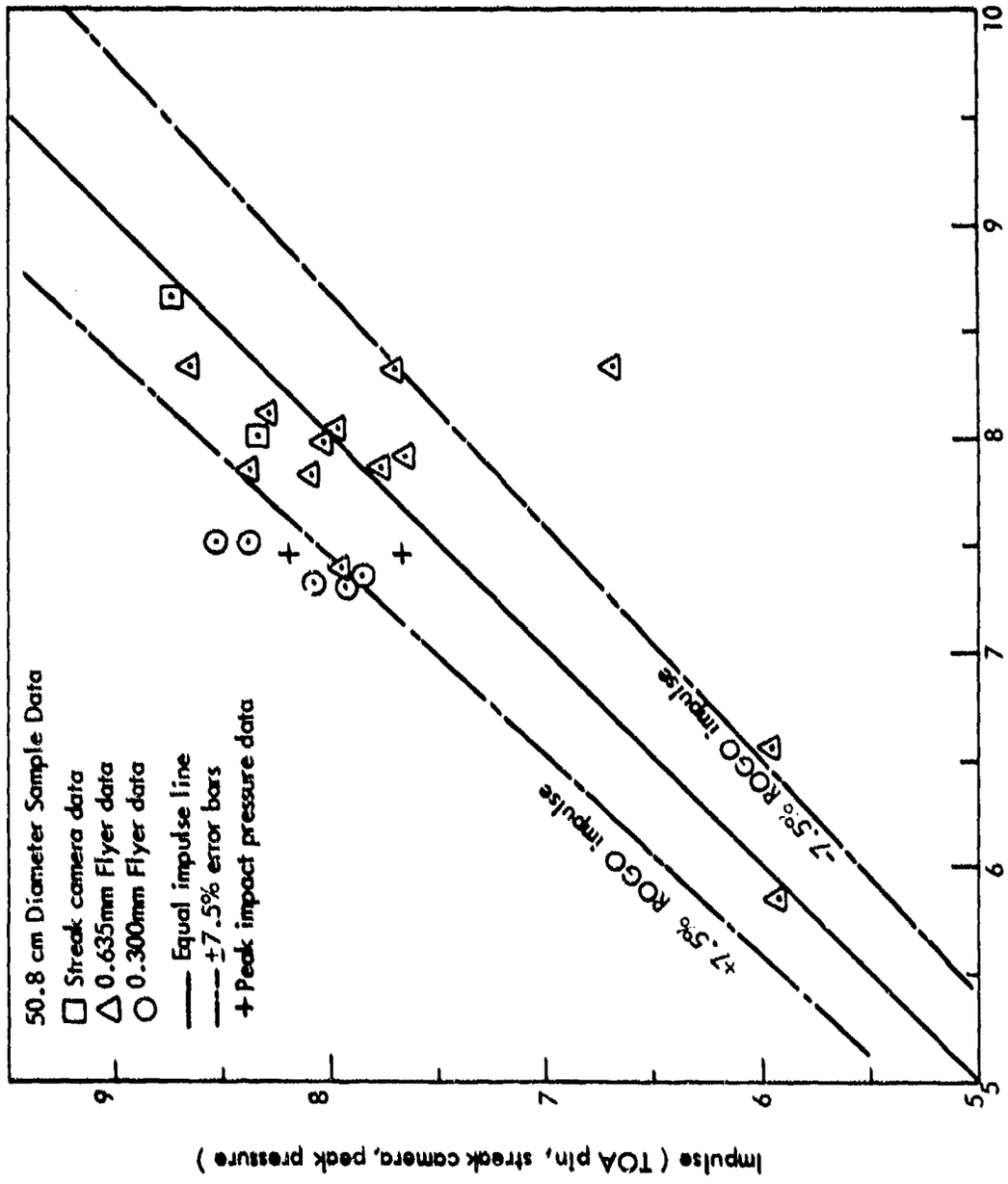

FIGURE 16 ROGO COIL IMPULSE VS TOA PIN IMPULSE, STREAK CAMERA IMPULSE, AND PEAK PRESSURE IMPULSE.

SHOT 2-304 0.64mm THICK AL FLYER PLATE

SHOT 2-306 0.3mm THICK AL FLYER

FIGURE 17 STREAK CAMERA MEASUREMENT OF 0.64mm AND 0.3mm THICK ALUMINUM FLYER PLATES

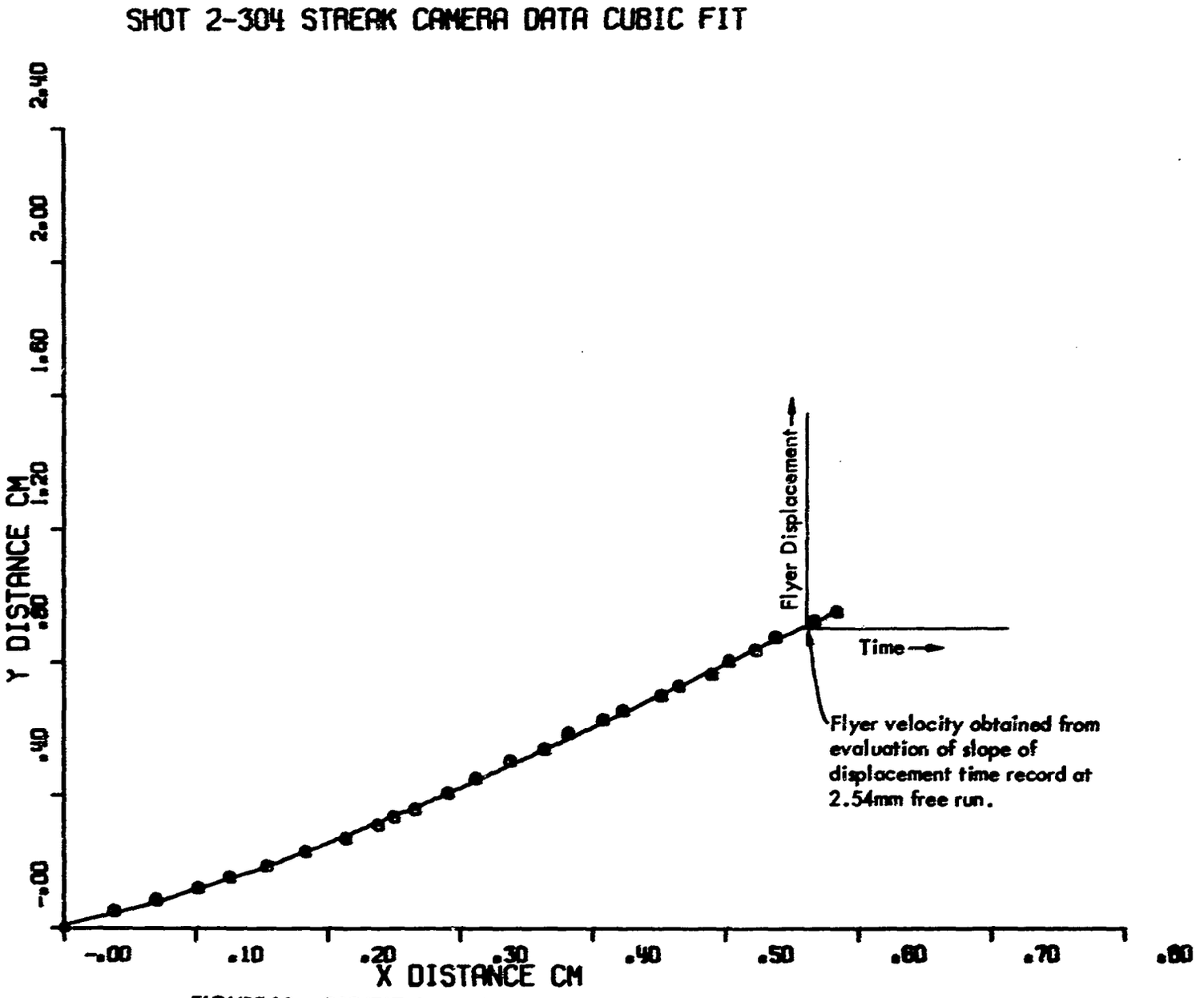

FIGURE 18 DIGITIZED RECORD OF STREAK CAMERA MEASUREMENT, SHOT 2-304

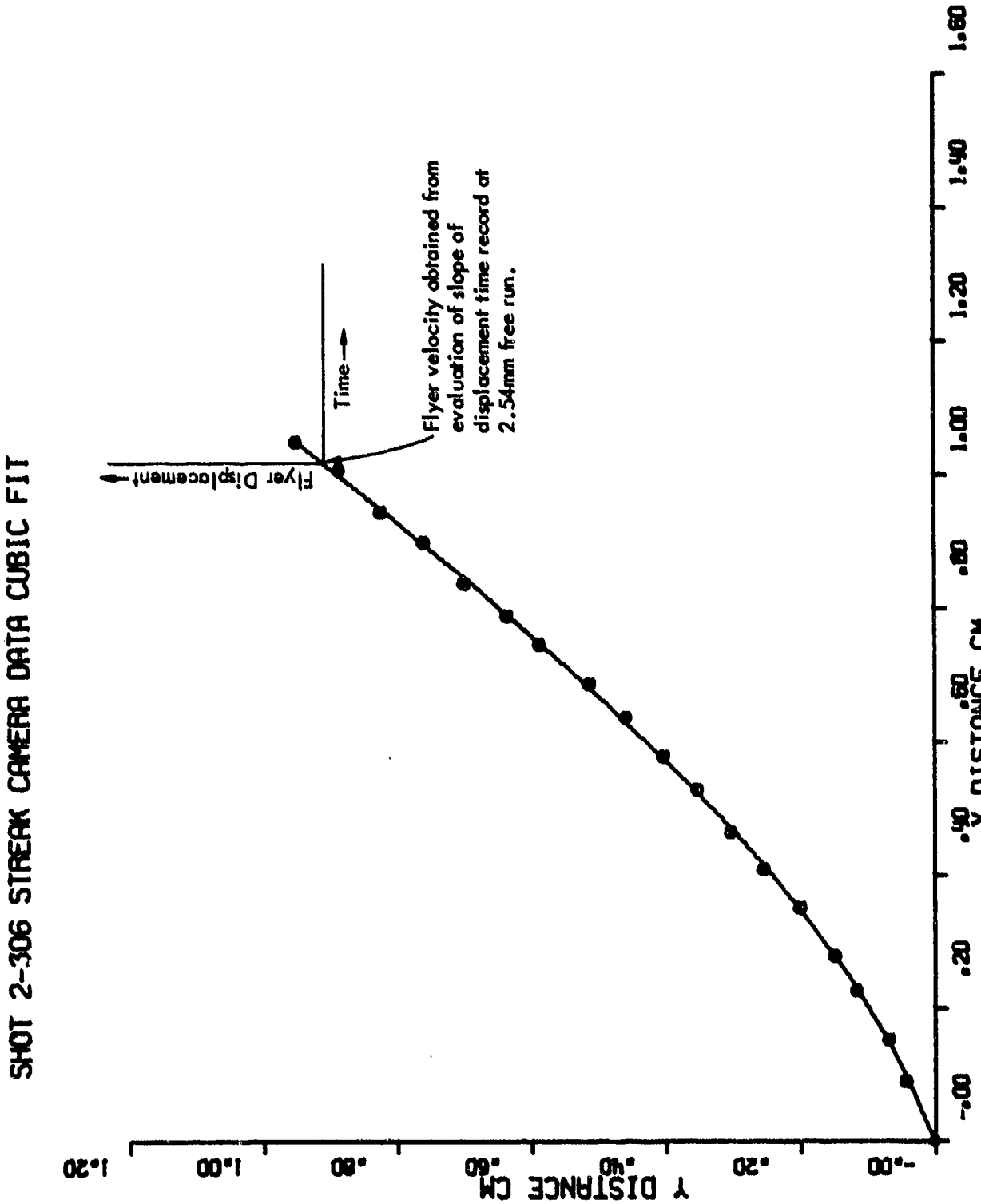

FIGURE 19 DIGITIZED RECORD OF STREAK CAMERA MEASUREMENT, SHOT 2-306

4.2.3 3DQP Arc Shots

Eighteen arcs were impacted by KSC to evaluate the 1-D stress wave damage of 3DQP for comparison with the AWRE facility results. Eighteen shots were performed for damage as a function of flyer thickness and/or free run; thirteen shots being performed with 0.64-mm thick aluminum flyer and 5 shots being performed with 0.3-mm thick aluminum flyers. Four shots were performed to obtain the transmitted pressure waveform at the rear surface of the 12.7-mm thick 3DQP samples, two waveforms being obtained with each flyer plate thickness.

The arc samples were machined from the ring with a radial side cut such that they measured 5.08-cm wide and 1.27-cm thick with a chord length of 5.08 cm. The material had an A_R/A_T ratio of .55[2], bulk density of 1.60 gm/cm^3 [2], and an open porosity of 7%[2].

Evaluations of damage suffered by each of the 3DQP arcs were based on the following criteria:

1) Damage Mode
2) Post-Test Sample Growth
3) Post-Test Sound Speed
4) Post-Test Open Porosity
5) Post-Test % Retained Modulus Property
6) Pre- and Post-Test Radiographs.

The post-test sound speed, open porosity, and % retained modulus data were supplied to KSC by SoRI.

The 1-D stress wave damage modes suffered by the 18 3DQP arcs were relatively large cracks found at the mid-plane location and cracks at the rear surface which formed together to cause rear surface lift of the circumferential and axial fibers at the higher loading levels. In addition, a number of

smaller cracks or near delaminations occurred near the front of the sample. Quite surprisingly, this damage description fits "A" process 3DQP very accurately, and is quite atypical of "C" process 3DQP failure. Further investigation suggests that a number of other characteristics of this 50.8-cm diameter 3DQP are common to "A" process but not to "C" process. These parameters are listed in Table 8. Further, Figure 20 shows a comparison of the failure modes typical of four pedigreed 3DQP materials. The 50.8-cm diameter material supplied by AWRE suffered "A" process damage modes at impulse levels nearly identical to those listed in Figure 20. A pre- and post-test radiograph is shown in Figure 21 to emphasize typical 1-D stress wave damage mode experienced by these samples. Based on the comparisons of the material properties shown in Table 7 and the dynamic failure mode as shown by Figures 20 and 21, the 50.8-cm diameter material is clearly more typical of "A" process 3DQP. This material still serves an important purpose for the correlation of the AWRE and KSC facilities, however, even though it was not of "C" process vintage.

The post-test sample growth, sound speed, open porosity, and P/Δ% retained data for the 27 KSC and AWRE shots are listed in Table 9. These four parameters yield an accurate insight to the post-test state of the 3DQP samples and, indeed, form the basis of the facility correlation. These data are plotted against impulse level in Figures 22 through 25. The data presented in these plots are obtained from impacts with 0.64-mm thick aluminum flyer plates only as this flyer will form the basis for all future work. Data produced by both the KSC and AWRE facilities are plotted in these figures.

TABLE 8 MATERIAL PROPERTY CHARACTERISTICS OF THE 50.8 CM DIAMETER 3DQP TEST SAMPLES COMPARED TO PEDIGREED 3DQP

MATERIAL IDENTIFICATION	CUTSIDE DIAMETER (cm)	A_R/A_T	OPEN POROSITY (%)	RADIAL VELOCITY (mm/μsec)	ATTENUATION (db)	PLIES/CM
50.8 cm Diameter	50.8	0.55	7	0.476	26	33
AHP "A"	22.9	0.48	8.5	0.500	29	32
CRS "C"	25.4	0.61	1.4	0.475	10	39

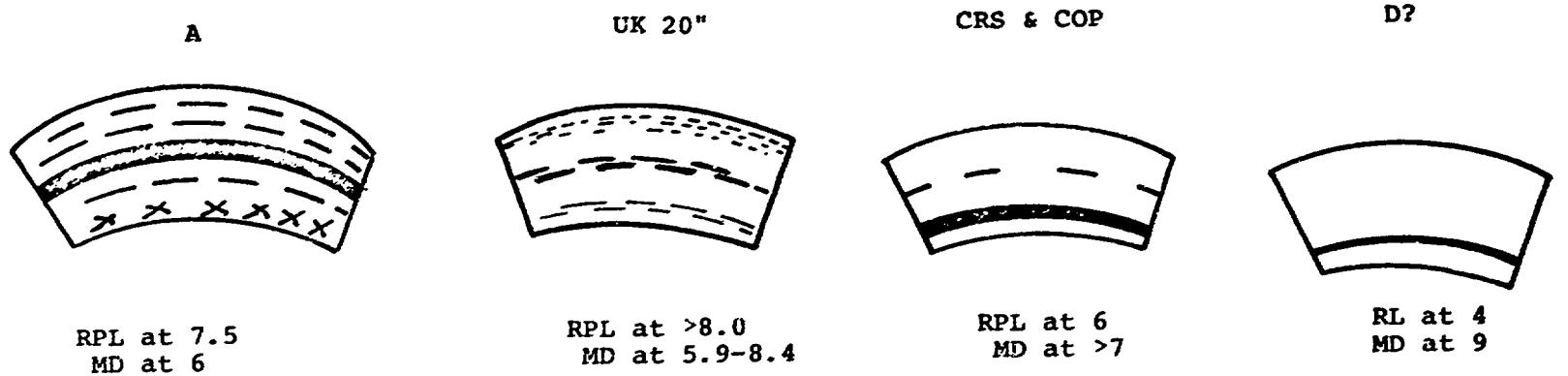

FIGURE 20 DAMAGE MODES OF FOUR PEDIGREED 3DQP MATERIALS
(Data furnished by SoRI)

PRETEST RADIOGRAPH

BK 35

POSTTEST RADIOGRAPH

FIGURE 21 TYPICAL PRE AND POST-TEST RADIOGRAPHS OF 50.8cm DIAMETER 3DQP ARC SAMPLE

TABLE 9 POST-TEST MATERIAL PROPERTIES OF ARCS IMPACTED BY KSC AND AWRE

SHOT #	SAMPLE / FACILITY[1]	FLYER THICKNESS (mm)	FREE RUN (mm)	IMPULSE (kilotaps)	SAMPLE GROWTH[2] (mm)	SOUND SPEED[2] (cm/μsec)	OPEN POROSITY[2] (%)	P/L[2] % RETAINED
2-290	BK6	0.64	2.54	8.0	0.429	0.431	10.0	39
2-291	BK33	0.64	2.54	8.0	0.424	0.428	10.9	38
2-292	BK35	0.64	2.54	7.9	0.622	0.427	10.0	49
2-293	AK3	0.30	2.54	7.5	0.767	0.421	11.1	38
2-294	AK4	0.30	2.54	7.3	0.950	0.419	13.0	32
2-295	AK30	0.30	2.54	7.4	0.996	0.411	12.2	34
2-300	CK57	0.64	2.54	3.1	0.551	0.429	10.8	63
2-301	CK58	0.64	2.54	7.4	0.437	0.442	10.5	56
2-302	GK24	0.64	2.54	6.6	0.229	0.456	8.6	66
2-303	HK25	0.64	2.54	5.9	0.163	0.465	7.6	69
2-323	CK11	0.64	2.54	7.9	0.320			
2-324	CK37	0.64	2.54	8.4	0.582			
2-325	DK13	0.64	5.08	7.8	1.308			
2-326	DK16	0.64	5.08	8.4	0.686		3	
2-327	DK18	0.64	1.27	8.4	1.100			
2-328	DK40	0.64	1.27	8.3	0.394			
2-329	DK42	0.30	2.54	8.1	1.443			
2-330	DK45	0.30	2.54	7.9	0.902			
	BA5	0.67	2.54	6.9	0.178	0.460	8.6	50
	BA7	0.67	2.54	6.9	0.197	0.457	8.4	47
	BA34	0.67	2.54	6.9	0.191	0.467	8.8	53
	AA2	0.30	2.54	6.2	0.137	0.445	8.5	51
	AA29	0.30	2.54	6.2	0.142	0.459	8.5	61
	AA31	0.30	2.54	6.2	0.152	0.464	8.2	54
	CA9	0.67	2.54	8.2	0.203			
	CA36	0.67	2.54	8.2	0.343		3	
	CA8	0.67	2.54	8.2	0.290			

[1]Second letter, either K or A, designates KSC or AWRE facility.

[2]Data used by permission of SoRI.

[3]Data not available from SoRI at present time.

CONFIDENTIAL

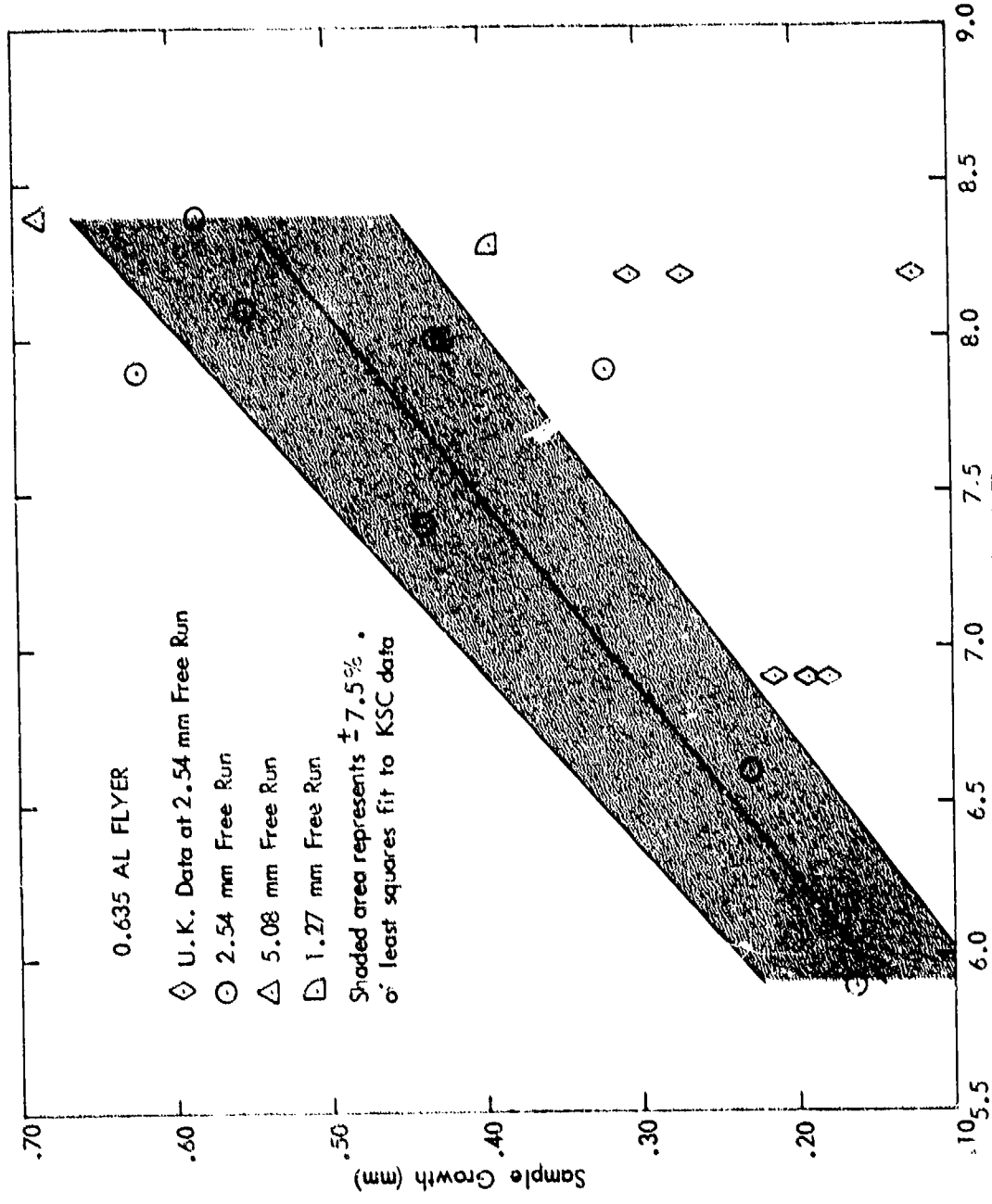

FIGURE 22 POST-TEST SAMPLE GROWTH VERSUS IMPULSE, 50.8-cm DIAMETER 3DQP

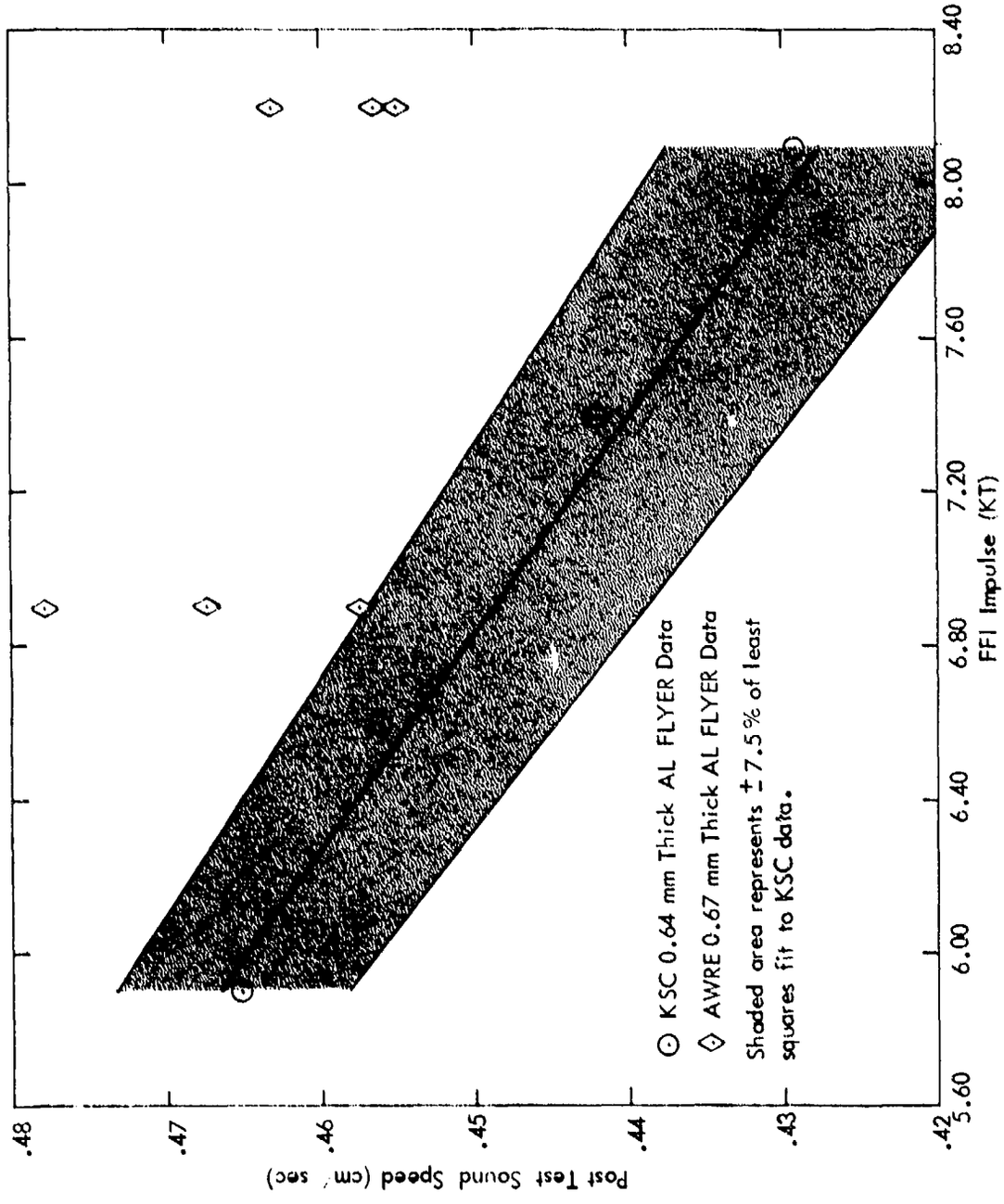

FIGURE 23 POST-TEST ULTRASONIC VELOCITY VERSUS IMPULSE, 50.8-cm DIAMETER 3DQP

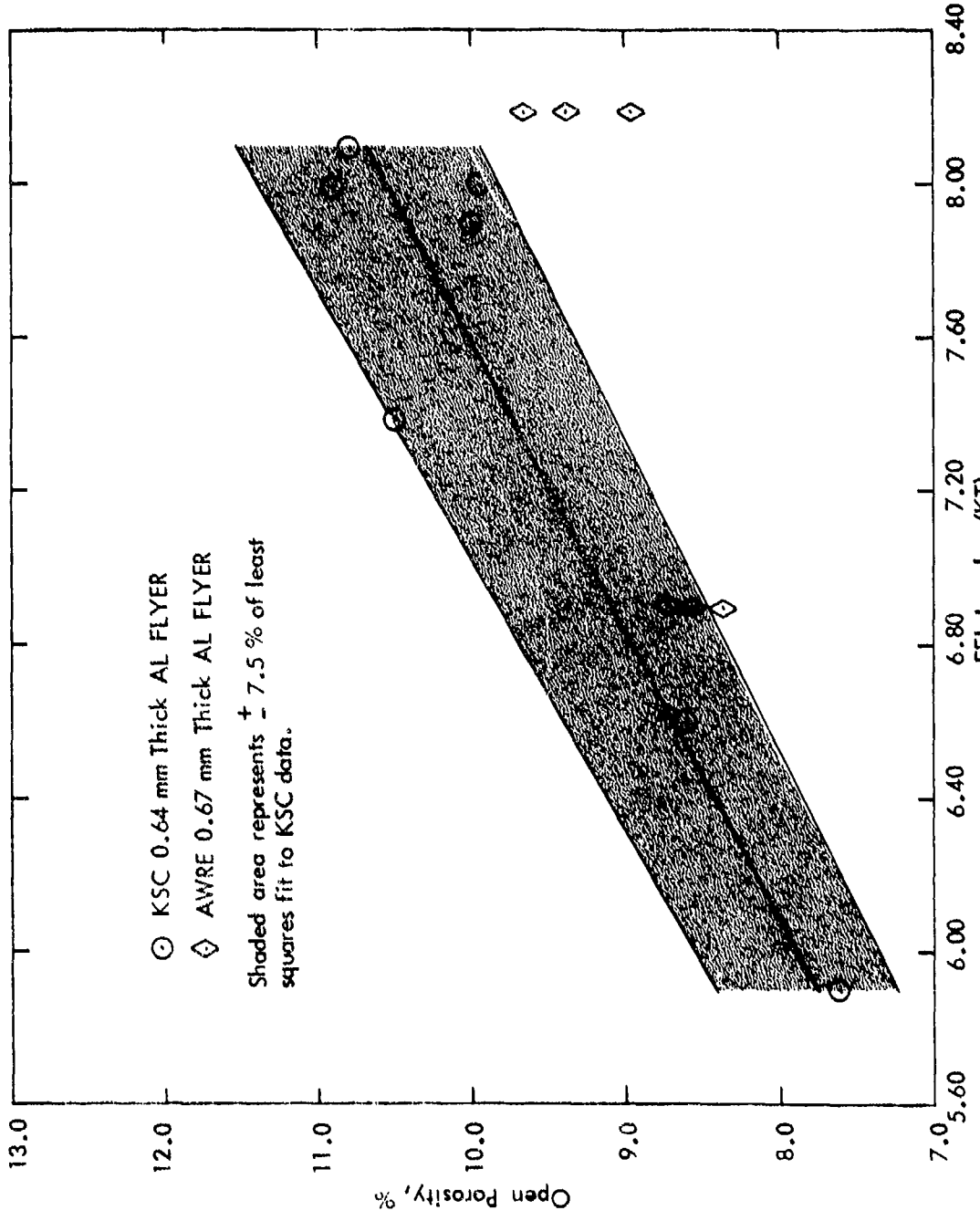

FIGURE 24 POST-TEST OPEN POROSITY VERSUS IMPULSE, 50.8-cm DIAMETER 3DQP

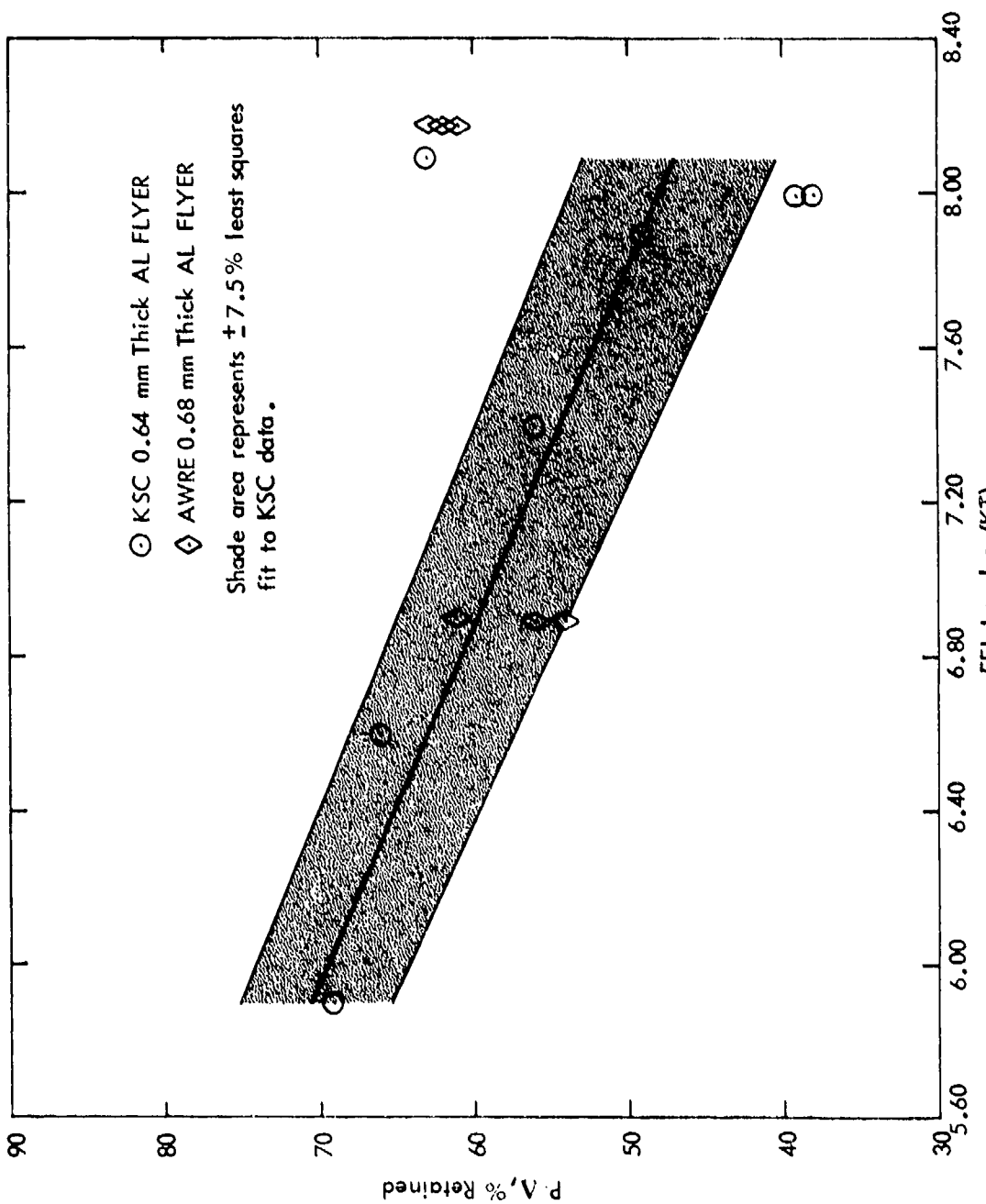

FIGURE 25 POST-TEST P.A.% RETAINED VERSUS IMPULSE, 50.8-cm DIAMETER 3DQP

For the four parameters plotted in Figures 22 through 25, each of the KSC data points are marked with error bars showing the possible range of KSC impulse values. Considering the range of KSC impulse values, the AWRE data falls within 10% of the KSC data for P/Δ % retained properties, and sample growth. For ultrasonic velocity, three AWRE data points fall within the range of KSC data; three other data points do not, however. For open porosity, three AWRE points measured within the range of the KSC data; open pososity data for the final three AWRE impacted samples are not yet available.

From these data KSC concludes that the two facilities are equivalent within approximately 10% in their ability to produce 1-D stress wave damage in arc samples.

KSC data indicated that significantly more damage was produced by the thinner 0.3 mm aluminum flyer than by the 0.64-mm thick flyer for an equivalent impulse level. The damage mode suffered by the 3DQP arc samples remained the same for each flyer thickness, the difference being that the 0.3-mm thick flyer produced more severe mid-plane cracking and rear surface fiber lifting. Post-test radiographs offer a visual representation of the damage from each thickness flyer. Radiographs typical of the damage produced by each flyer are shown in Figure 26.

The more severe damage produced by the 0.3-mm thick aluminum flyer may be explained by the fact that the thinner flyer produced a significantly more planar impact and that it may also produce a higher peak pressure transmitted through the thickness of the 3DQP arc samples. Obviously, the peak pressure at the impact surface is higher for the thinner flyer because it has approximately twice the velocity at impact. However, because of the highly dispersive nature of 3DQP, it was not clear that the pressure-time signature

DK 45

0.03mm THICK AL FLYER DAMAGE

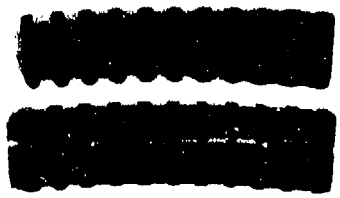

BK 33

0.64mm THICK AL FLYER DAMAGE

FIGURE 26 POSTTEST DAMAGE CAUSED BY 0.3MM AND 0.64MM THICK ALUMINUM FLYER IMPACTING 50.8CM DIA., 1.27CM THICK, 3DQP ARCS.

at the rear surface would be different for either flyer plate. For this reason, two transmitted pressure shots were conducted for each flyer thickness. The sample and gage geometry for the transmitted pressure waveforms are shown in Figure 27.

The four transmitted pressure waveforms are shown in Figures 28 through 31 and the pertinent data from these shots are summarized in Table 10. As seen from Table 10, the kilobar/kilotap value is approximately 25% higher for the thinner 0.3-mm thick aluminum flyer. The 0.3-mm thick flyer also produces more absolute pressure than the thicker flyer as the thin flyer produces almost 6 kilobars peak pressure while the thick flyer produces about 5 kilobars.

The combination of higher peak pressure transmitted through the entire sample thickness and a more planar impact by the thinner flyer produce stress wave conditions which are more likely to cause severe damage. For these reasons the thinner 0.3-mm thick flyer causes more damage as graphically shown by the radiographs in Figure 26. A plot of post-test sample growth also demonstrates the more severe stress wave damage produced by the thinner flyer. The sample growth data for the 0.3-mm thick flyer is shown in Figure 32. As shown in this graph, the sample growth is much larger at an equivalent impulse for the thin flyer as compared to sample growth produced by a thick flyer (see Figure 22).

Six shots were performed with 0.64-mm thick aluminum flyers impacting 3DQP arc samples to judge the effects of free run on 1-D stress wave damage. At varied free runs impulse momentum enhancement due to air cushioning and flyer plate buckling are variables which typically grow larger at longer free runs and may have a significant effect on damage.

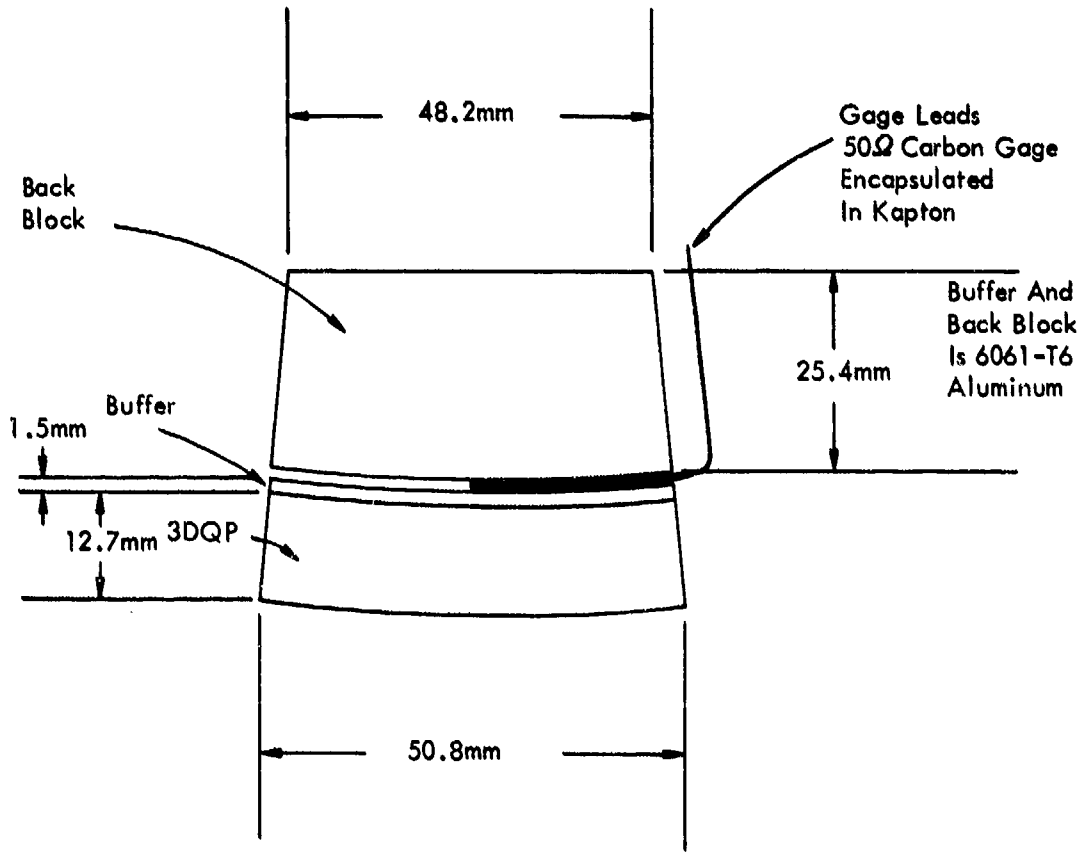

FIGURE 27 SAMPLE AND GAGE GEOMETRY FOR TRANSMITTED PRESSURE WAVEFORM SHOTS

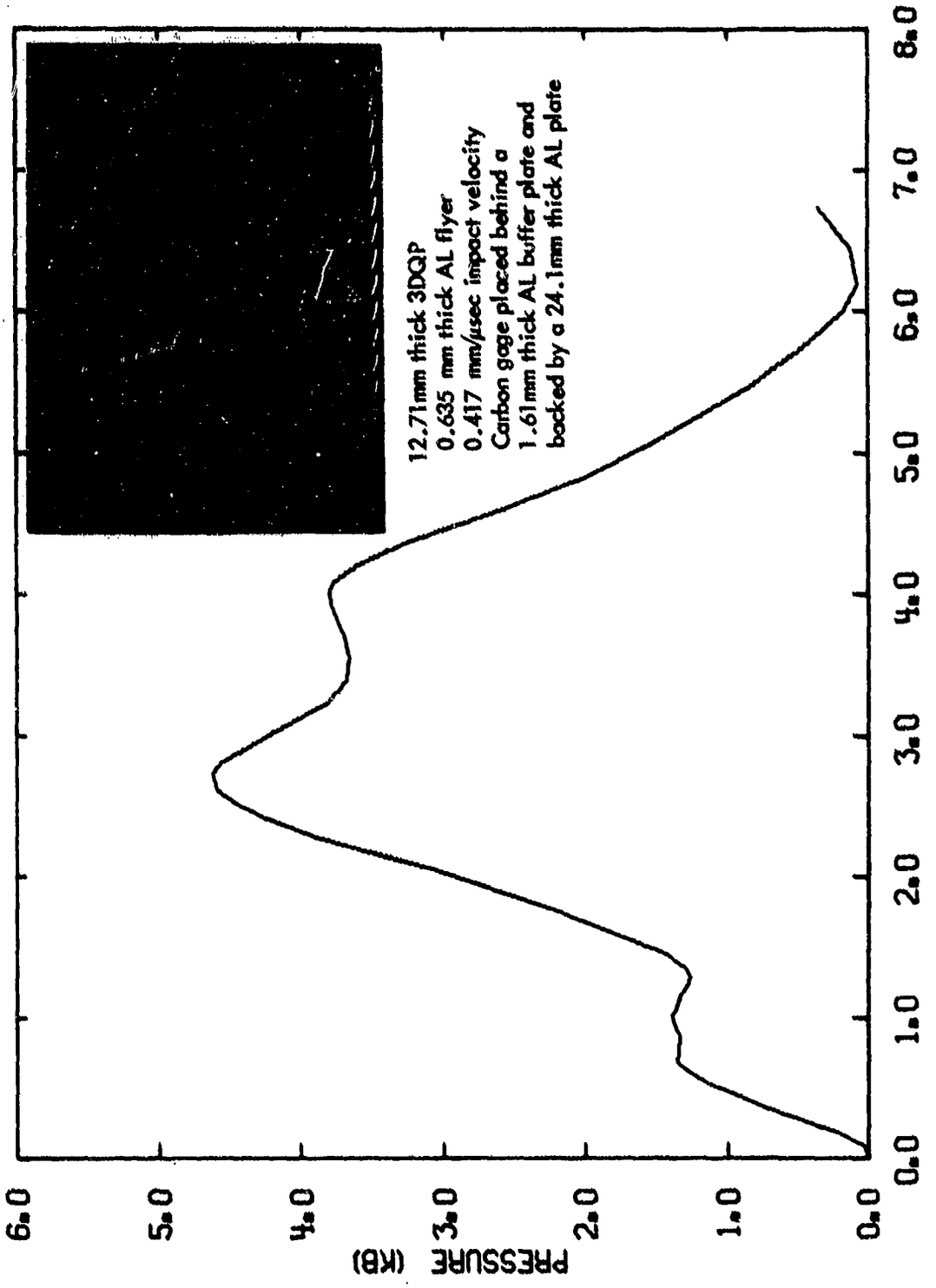

FIGURE 28 3DQP TRANSMITTED PRESSURE WAVEFORM SHOT 2-296

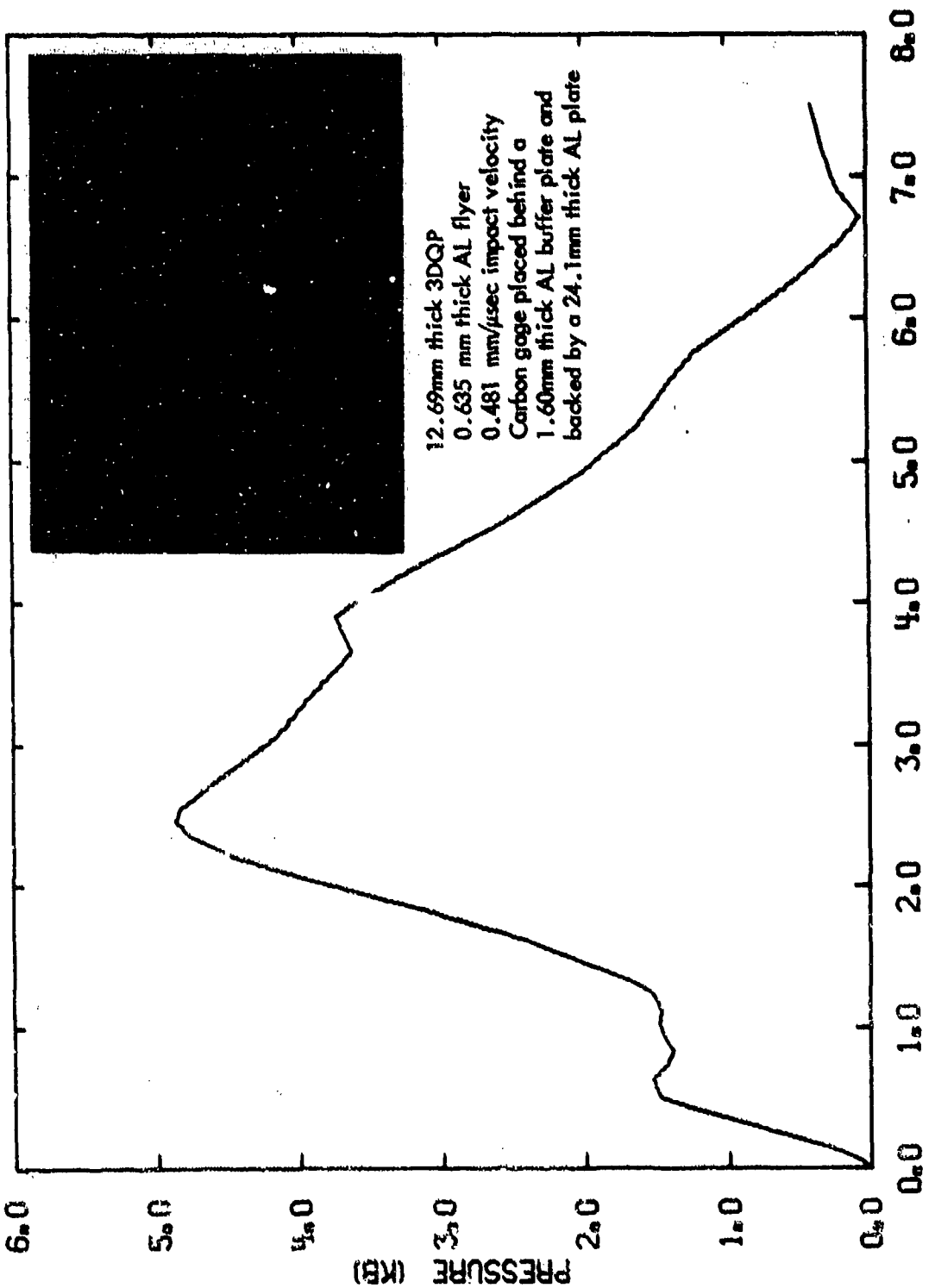

FIGURE 29 3DQP TRANSMITTED PRESSURE WAVEFORM SHOT 2-297

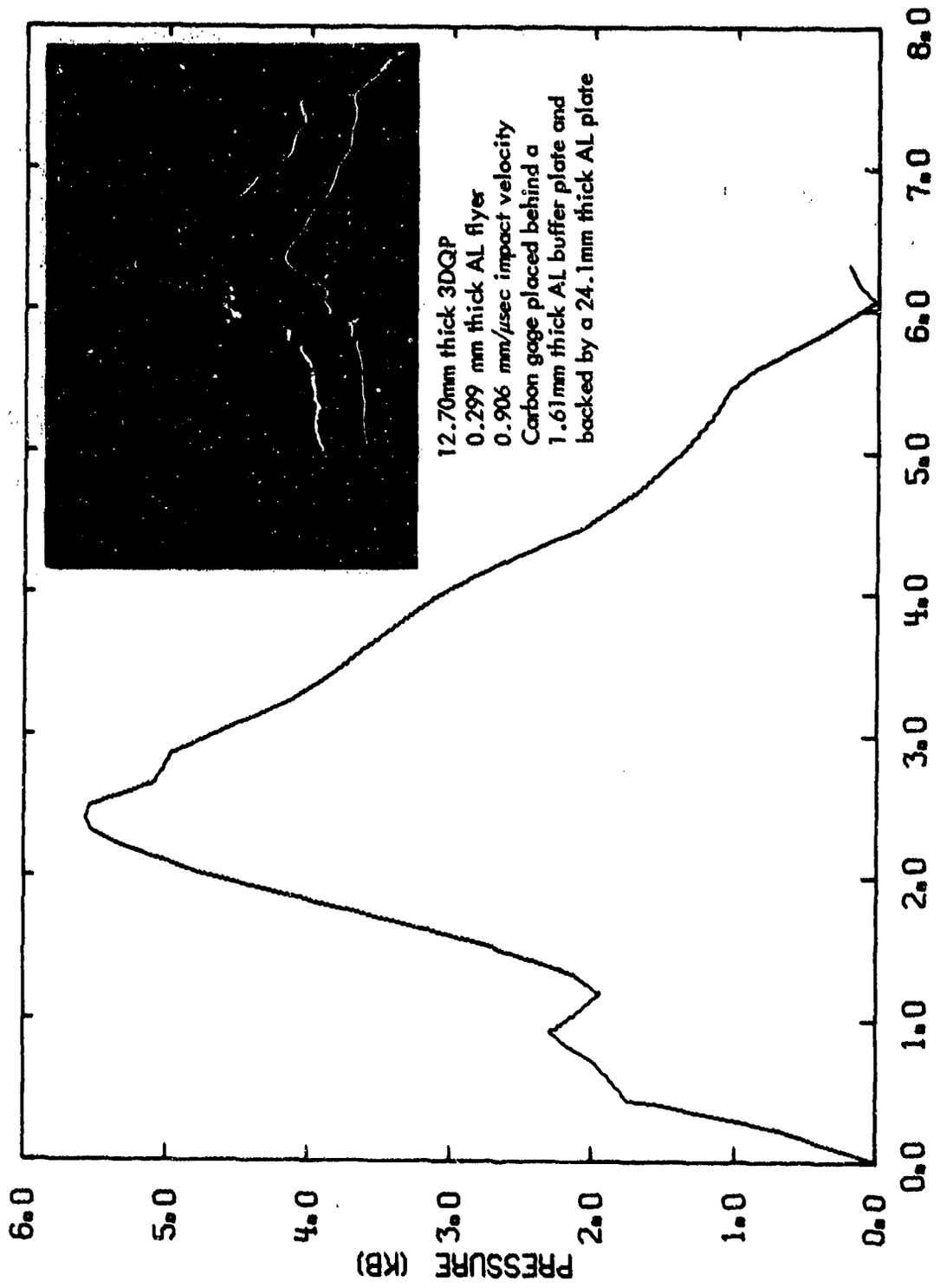

FIGURE 30 3DQP TRANSMITTED PRESSURE WAVEFORM SHOT 2-298

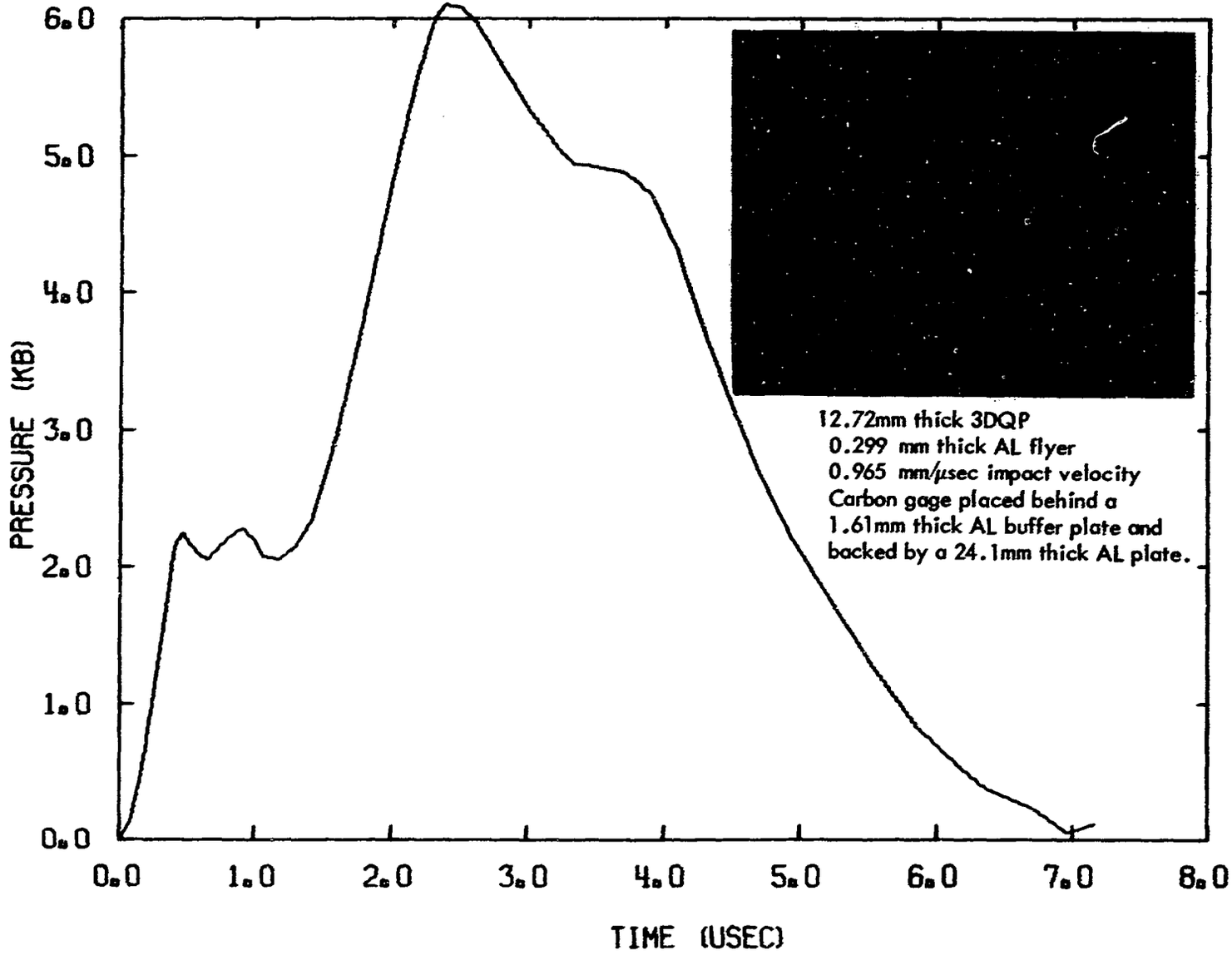

FIGURE 31 3DQP TRANSMITTED PRESSURE WAVEFORM SHOT 2-299

TABLE 10 3DQP TRANSMITTED PRESSURE WAVEFORM SHOT SUMMARY

SHOT #	SAMPLE #[1]	FLYER THICKNESS (mm)	PEAK PRESSURE IN ALUMINUM (kilobars)	PEAK PRESSURE[2] IN SAMPLE (kilobars)	IMPULSE[3] (KILOTAPS)	KILOBARS/ KILOTAPS
2-296	FK47	.635	4.6	3.0	7.2	.42
2-297	CK10	.635	4.9	3.2	8.3	.39
2-298	FK23	.300	5.5	3.6	7.3	.49
2-299	FK49	.300	6.1	4.0	7.8	.51

[1]Thickness of 3DQP samples was 1.27 cm.

[2]Peak pressure at rear surface of 3DQP; because of impedance mismatch between sample and aluminum, $P_{3DQP} = .65\ P_{Al}$.

[3]Prompt impulse as determined from Veldet.

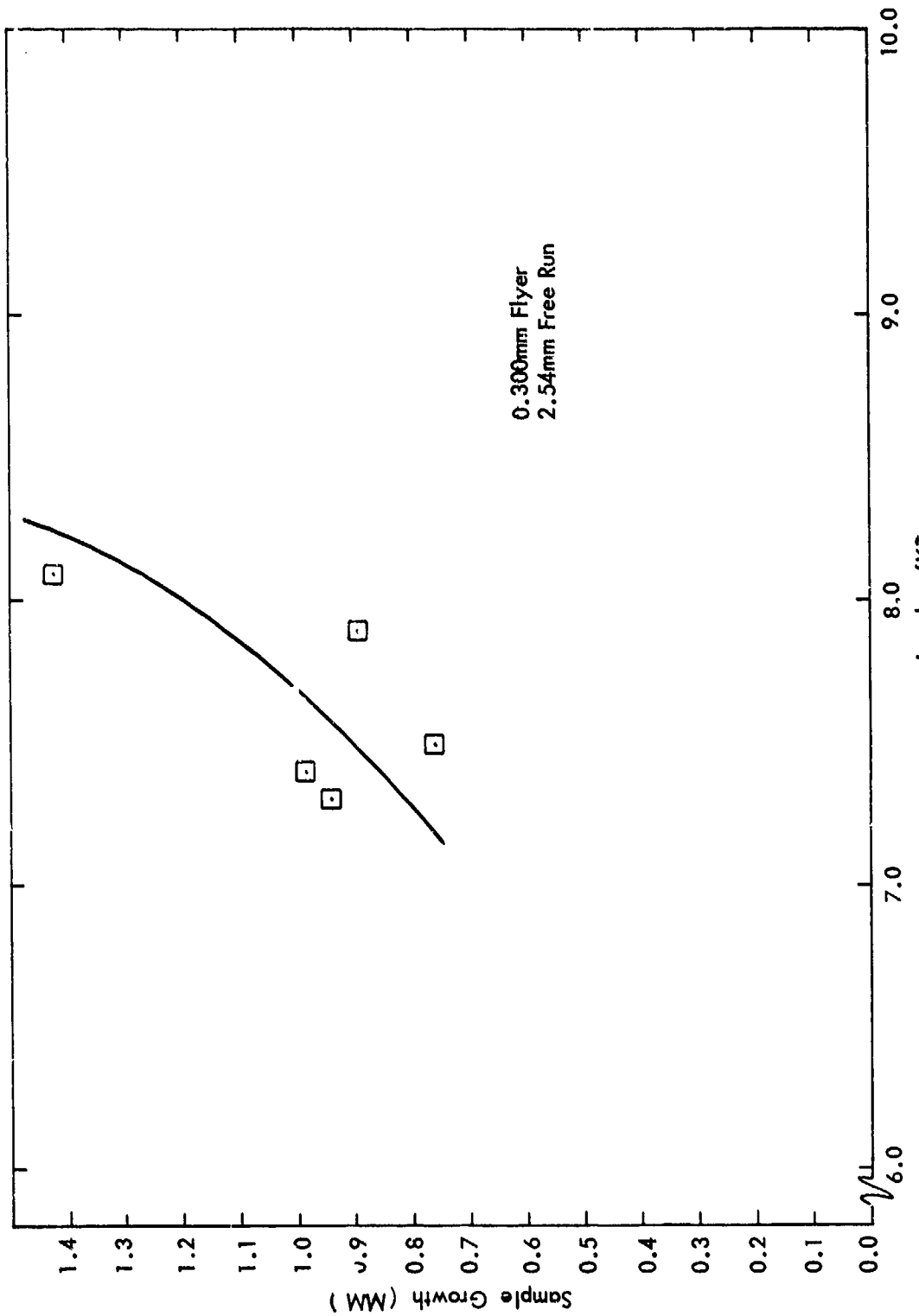

FIGURE 32 SAMPLE GROWTH VS IMPULSE DATA FOR 0.3MM THICK ALUMINUM FLYERS IMPACTING 50.8CM DIA., 1.27CM THICK, 3DQP ARCS.

To examine these factors, shots were performed at target standoff distances of 1.27 mm, 2.54 mm, and 5.08 mm.

Unfortunately, the results of the free run study were inconclusive. An examination of sample growth data would indicate that the arcs hit at the longer free runs did not suffer significantly more growth than those hit at shorter free runs. For example, the sample growth data recorded at all free run distances fall within the expected scatter (as can be seen in Figure 22). However, a plot (see Figure 33) of all sample growth data as a function of free run is inconclusive because large scatter of a few data points tends to make a definite conclusion impossible. Perhaps the statement that can be made is that the 1-D damage is not significantly altered as a result of either air cushion momentum enhancement or flyer plate buckle. It should be remembered in the case of flyer plate buckle, however, that the radius of curvature of the flyer plate was relatively large because of the large diameter of the test samples. The initial large radius of curvature of the flyer would tend to minimize flyer buckle over the free run distances involved in the Facility Correlation Study. In the UGT Simulation Study, the initial radius of curvature of the flyer is small, however, and the effects of flyer buckle must be addressed for the free run distance to be used in that study.

4.2.4 Air Cushion Momentum Enhancement

Shots conducted at three free run distances offered an opportunity to measure the momentum enhancement delivered to the sample as a result of air cushion. The momentum enhancement was measured with the aid of the Dynafax high-speed camera. The Dynafax camera measures the total impulse delivered

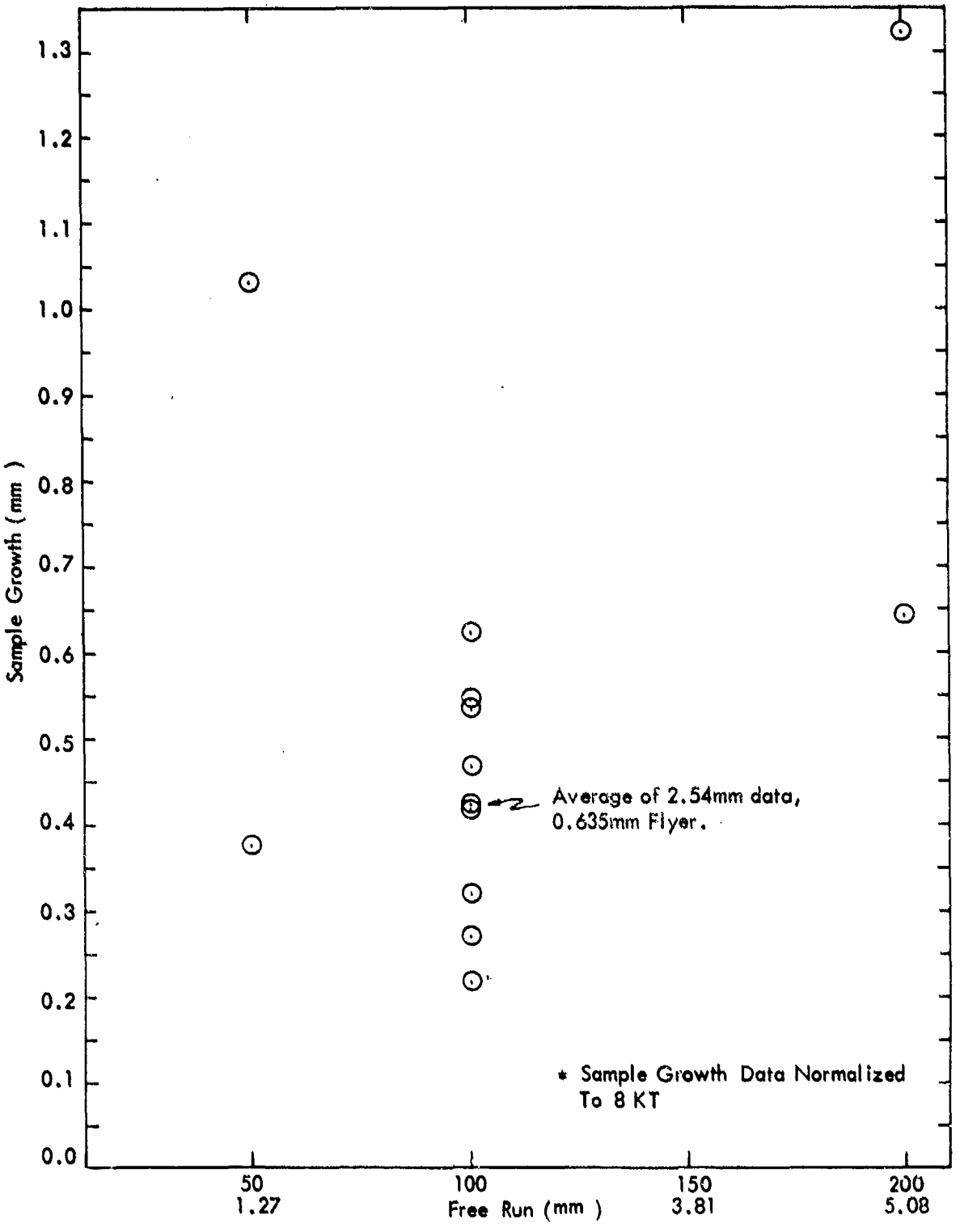

FIGURE 33 SAMPLE GROWTH*VS FREE RUN FOR 0.64MM THICK ALUMINUM FLYERS IMPACTING 50.8CM, 1.27CM THICK, 3DQP ARCS.

to the sample. The difference between the Dynafax impulse value and the impulse delivered by the flyer plate and post-impact magnetic push determines the impulse due to air cushion.

The air cushion data obtained from the six shots conducted with a 0.64-mm thick aluminum flyer are presented in Table 11. These data are plotted in Figure 34. In this figure the apparent momentum enhancement, measured simply as the difference between the Dynafax impulse and the flyer plate plus magnetic push impulse, is plotted against the free run distance for which the data were obtained. As shown in the figure, an increasing impulse is imparted to the sample as the free run grows longer. A second representation of the data is also shown in Figure 34. In this representation, the air cushion momentum is divided by the free run distance and expressed as momentum/unit distance. As shown in Figure 34 this numerical representation of enhancement is more nearly a constant value, approximately 5 taps/cm, over all free run distances.

Interestingly, the KSC enhancement data nicely fit a theory proposed in H10.1 Data Report No. 39[3] which was written by AWRE personnel. The AWRE air cushion analysis predicts the air cushion momentum enhancement for 3DQP samples as a function of the specific kinetic energy of the flyer plate and the free run distance. The momentum enhancement is expressed as the total sample impulse (as measured by Dynafax) divided by the flyer and post-magnetic push impulse, resulting in an expression of the enhancement as a percentage increase in momentum (momentum enhancement factor). The AWRE theoretical values and the KSC experimental values are shown plotted in Figure 35. The agreement is quite good.

TABLE 11 APPARENT AIR CUSHION MOMENTUM ENHANCEMENT SHOT SUMMARY

SHOT #	FLYER PLATE THICKNESS (mm)	FREE RUN (mm)	VELDET IMPULSE[1] (kilotaps)	DYNAFAX IMPULSE (kilotaps)	AIR CUSHION[2] (kilotaps)
2-323	0.64	2.54	7.9	9.2	1.3
2-324	0.64	2.54	8.4	9.6	1.2
2-325	0.64	5.08	7.9	9.6	1.7
2-326	0.64	5.08	8.4	10.4	2.0
2-327	0.64	1.27	8.5	8.9	0.4
2-328	0.64	1.27	8.4	9.1	0.7

[1]This value includes contribution of post-impact magnetic push.

[2]This value of air cushion is reported for aluminum impacting 3DQP samples. Different flyer or target materials could yield different values at these free runs because the shock impedances of the impacting materials are important.

CONFIDENTIAL

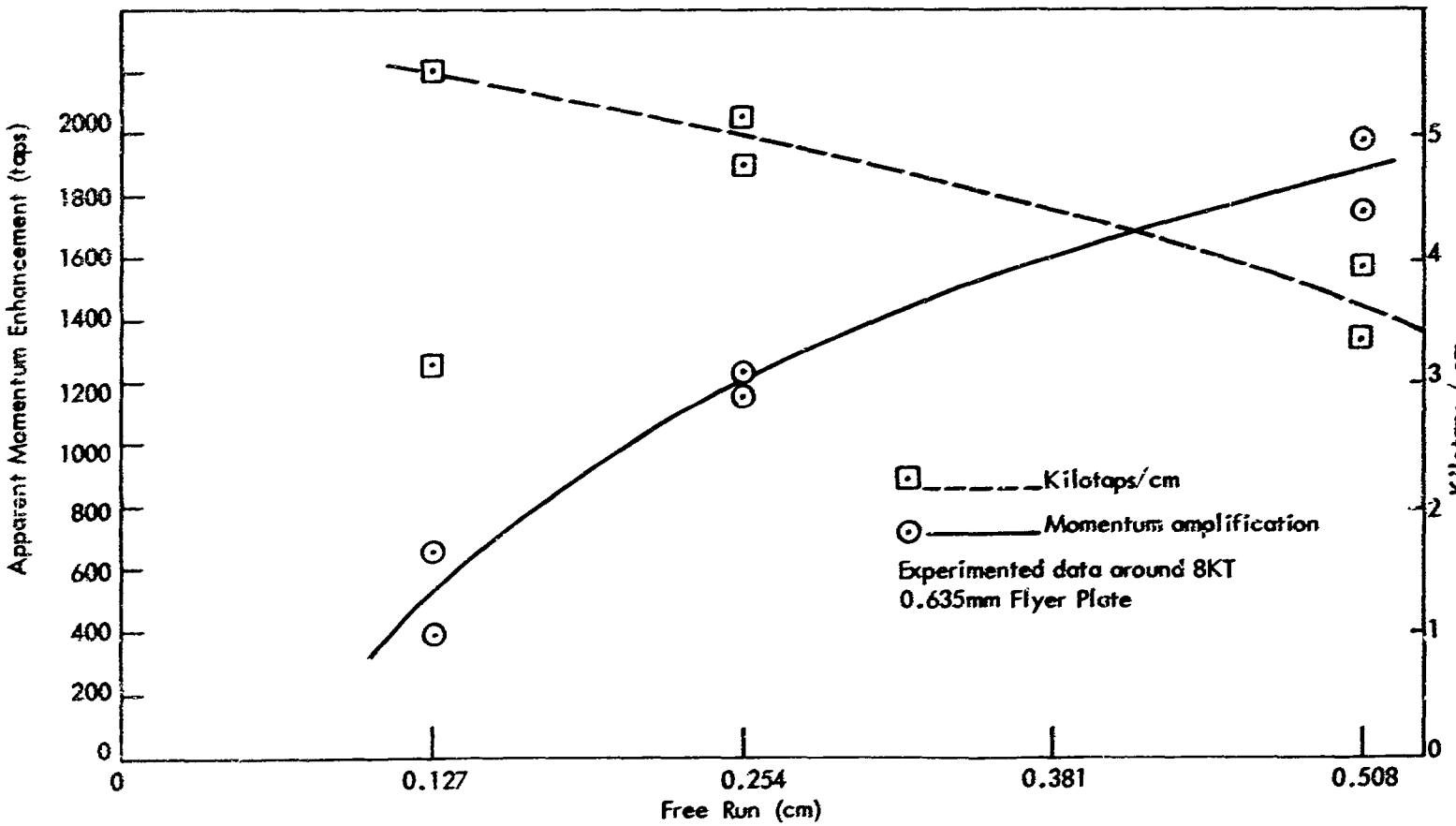

FIGURE 34 APPARENT MOMENTUM ENHANCEMENT VERSUS FREE RUN

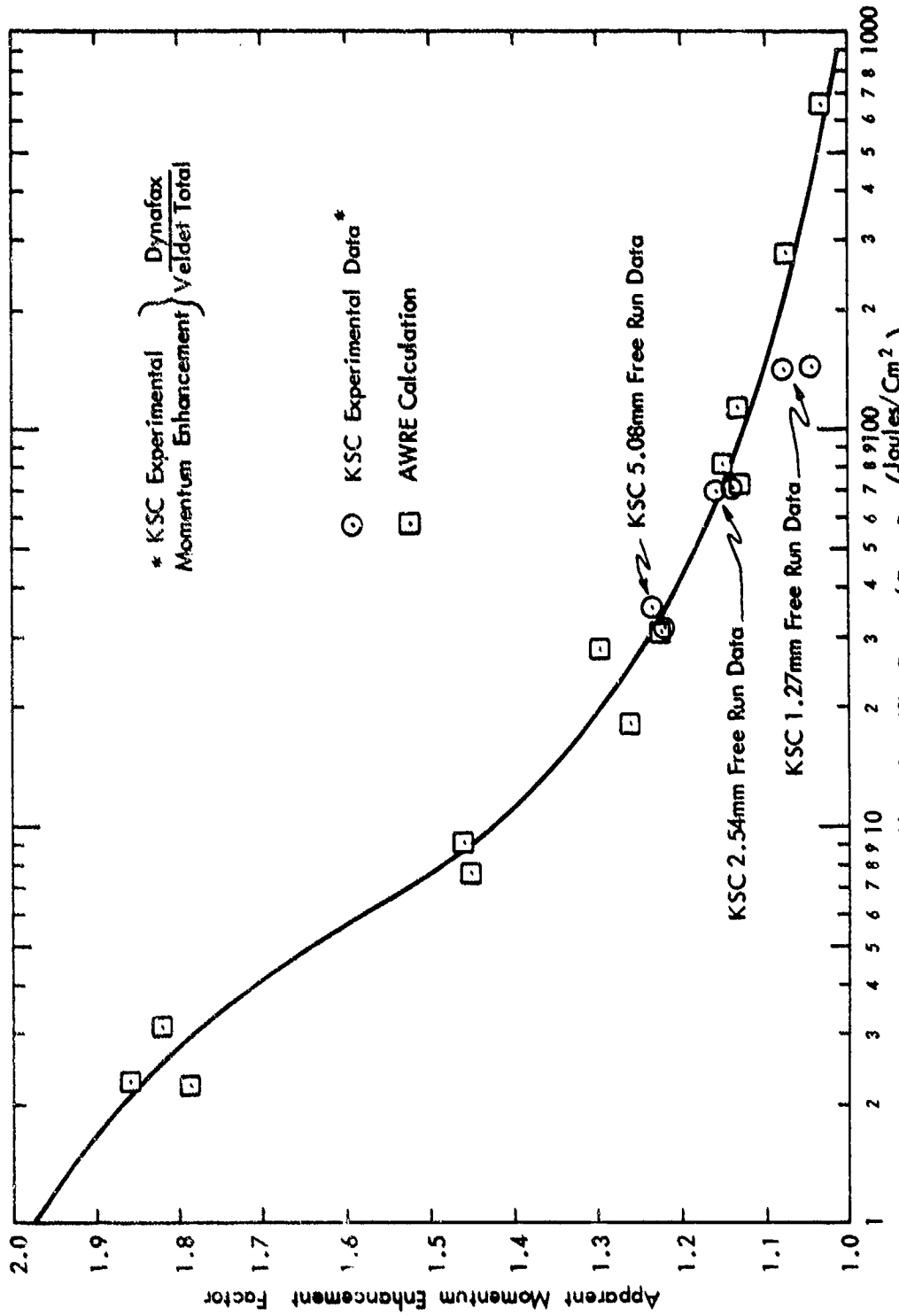

FIGURE 35 MOMENTUM ENHANCEMENT FACTOR VS FLYER PLATE PARAMETERS

4.3 TASK 4: COMBINED RESPONSE DATA

Combined shock and structural response data were obtained by impacting instrumented aluminum and 3DQP rings with 0.635-mm aluminum flyer plates. All of the rings had 50.8-cm O.D.'s and were 5.08 cm wide. The impulsive loads were applied with a half-cosine spatial distribution. In order to verify the adequacy of the experimental procedures and infer mechanical property data, measured strains were correlated with theoretical predictions of the KSC TWORNG code.

4.3.1 Aluminum Rings

Three 6061-T6 aluminum rings were instrumented with strain gages according to the scheme shown in Figure 36. Each ring had a wall thickness of 8.94 mm. The relevant shot numbers, maximum flyer free runs (δ_o), and peak impulses (I_o) are shown in the table below.

		I_o (ktaps)		
Shot No.	δ_o (mm)	Prompt	Total (w/o Air Cushion)	Total (w/Air Cushion)
2-311	2.54	5.6	5.7	6.5
2-312	2.54	7.9	8.0	8.8
2-320	0.66	8.3	13.3	13.5

Prompt and total impulses without air cushioning were determined from Veldet calculations. The effect of air cushioning on aluminum was accounted for by including an impulse of approximately 315 taps per mm of flyer free run. Structural response calculations were based on loads which included the air cushioning impulse.

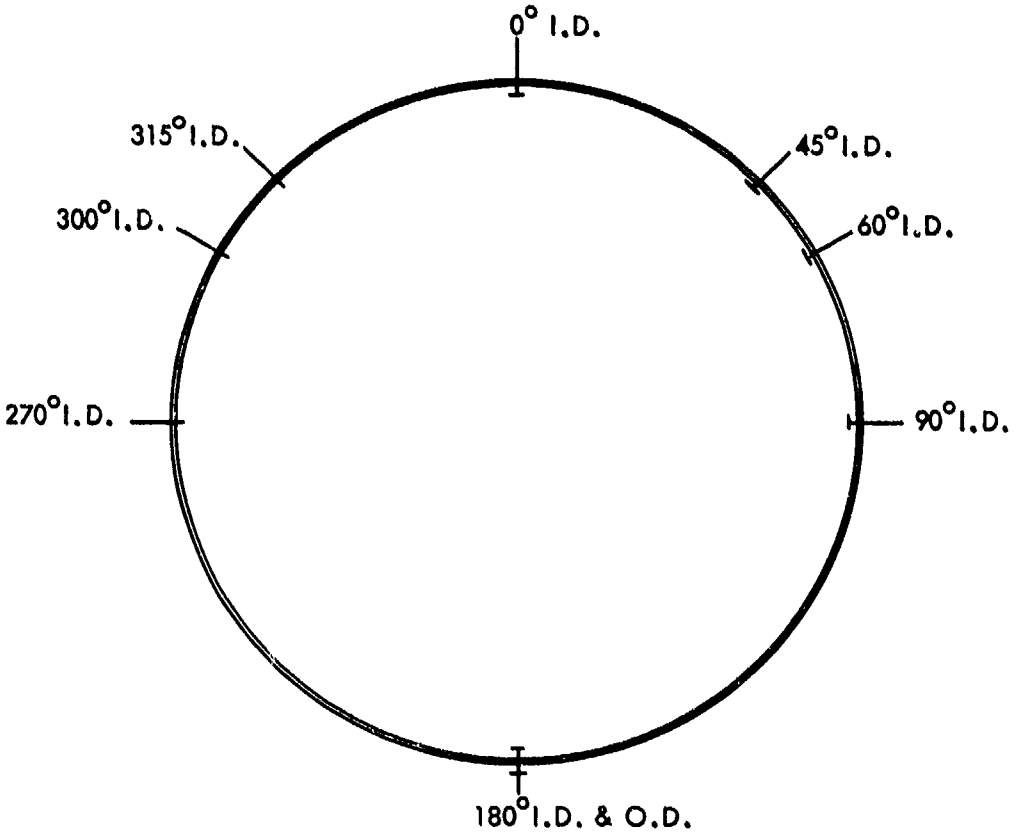

FIGURE 36 STRAIN GAGE LOCATIONS FOR 50.8cm 6061-T6 ALUMINUM RINGS

The theoretical strain predictions were obtained numerically through the use of the TWORNG code. This finite-difference ring code was originated several years ago by KSC and is continuously being updated to incorporate new and refined material models and associated phenomena.

TWORNG treats the dynamic response of single-layer or soft-bonded, double-layer rings to impulsive or thermal shock loads. The rings may have variable thickness due to the effects of spall, and the materials may be quite generally nonlinear and spatially nonuniform. Only bond materials, however, are allowed to have finite shear rigidity, and the kinematics (strain-displacement relations) are based on linear theory.

TWORNG provides approximately for the geometric effects associated with moderately thick rings ($h/R \approx 10$). Initial fracture or fracture incurred during structural response is also accounted for. Kelvin type damping may be independently specified for extensional and flexural motions.

Predictions for the aluminum rings were based on 8 integration stations through the thickness and 24 finite difference grid points around the circumference in the interval $0 \leq \theta \leq \pi$. For stability and ease of interpretation, a time step of 5 μsec was chosen.

The material parameters used in the aluminum ring calculations are shown below.

$$\rho = 2.71 \times 10^{3} \text{ kg/m}^3 \quad (2.71 \text{ gm/cc})$$

$$E = 72.4 \times 10^{9} \text{ N/m}^2 \quad (10.5 \times 10^{6} \text{ psi})$$

$$\sigma_y = 0.276 \times 10^{9} \text{ N/m}^2 \quad (40.0 \times 10^{3} \text{ psi})$$

$$E_p = \begin{cases} 0.621 \times 10^9 \text{ N/m}^2 \ (90.0 \times 10^3 \text{ psi}) \text{ in tension} \\ 1.034 \times 10^9 \text{ N/m}^2 \ (150.0 \times 10^3 \text{ psi}) \text{ in compression} \end{cases}$$

$$\eta = \begin{cases} 0.05\% \text{ extension and flexure (shot nos. 2-311 \& 2-312)} \\ 0.60\% \text{ extension and flexure (shot no. 2-320)} \end{cases}$$

Young's modulus (E), yield strength (σ_y), and plastic or secondary modulus (E_p) were taken from available published data. The critical damping ratio (η) was based on values used in previous aluminum structural response correlations performed by KSC.

Predicted and measured strains for the low impulse test (shot no. 2-311) are presented in Figures 37(a) and 37(b). Correlations for the edge gage at 0° are not shown here or in the sequel because this gage continually malfunctioned during the Task 4 test series. Excellent load symmetry is demonstrated by comparing measured outputs at $\pm 45^\circ$, $\pm 60^\circ$, and $\pm 90^\circ$. The measured responses at these locations are shown in Figures 38, 39, and 40 respectively.

With regard to frequencies and waveforms, the correlations for shot no. 2-311 are reasonably good at all circumferential locations, particularly on the back half of the ring. All of the aluminum ring correlations would have improved had structural damping been selected a posteriori rather than a priori. Minor correlation improvements would also have resulted from refined analytical modeling of the impulsive load spatial distribution, which is not identical to a half-cosine in practice.

Predicted and measured first compressive peaks on the front half of the shot no. 2-311 ring, particularly at 0° and 45°, are not in good agreement. Some of the difficulty could be due to inaccurate analytical modeling of the stress-strain

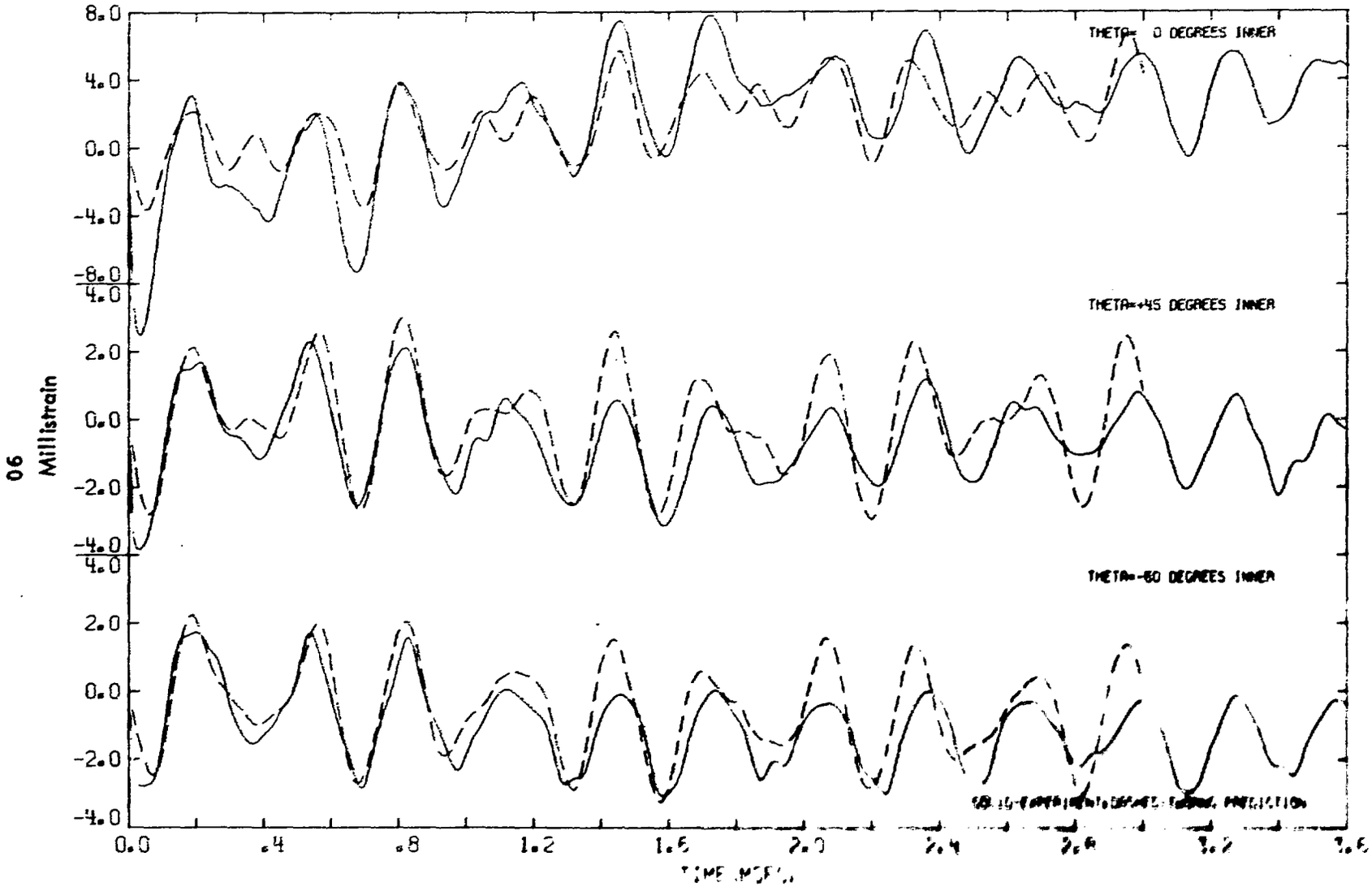

FIGURE 37a DYNAMIC RESPONSE CORRELATION FOR A 50.8CM O.D. ALUMINUM RING (SHOT 2-311)

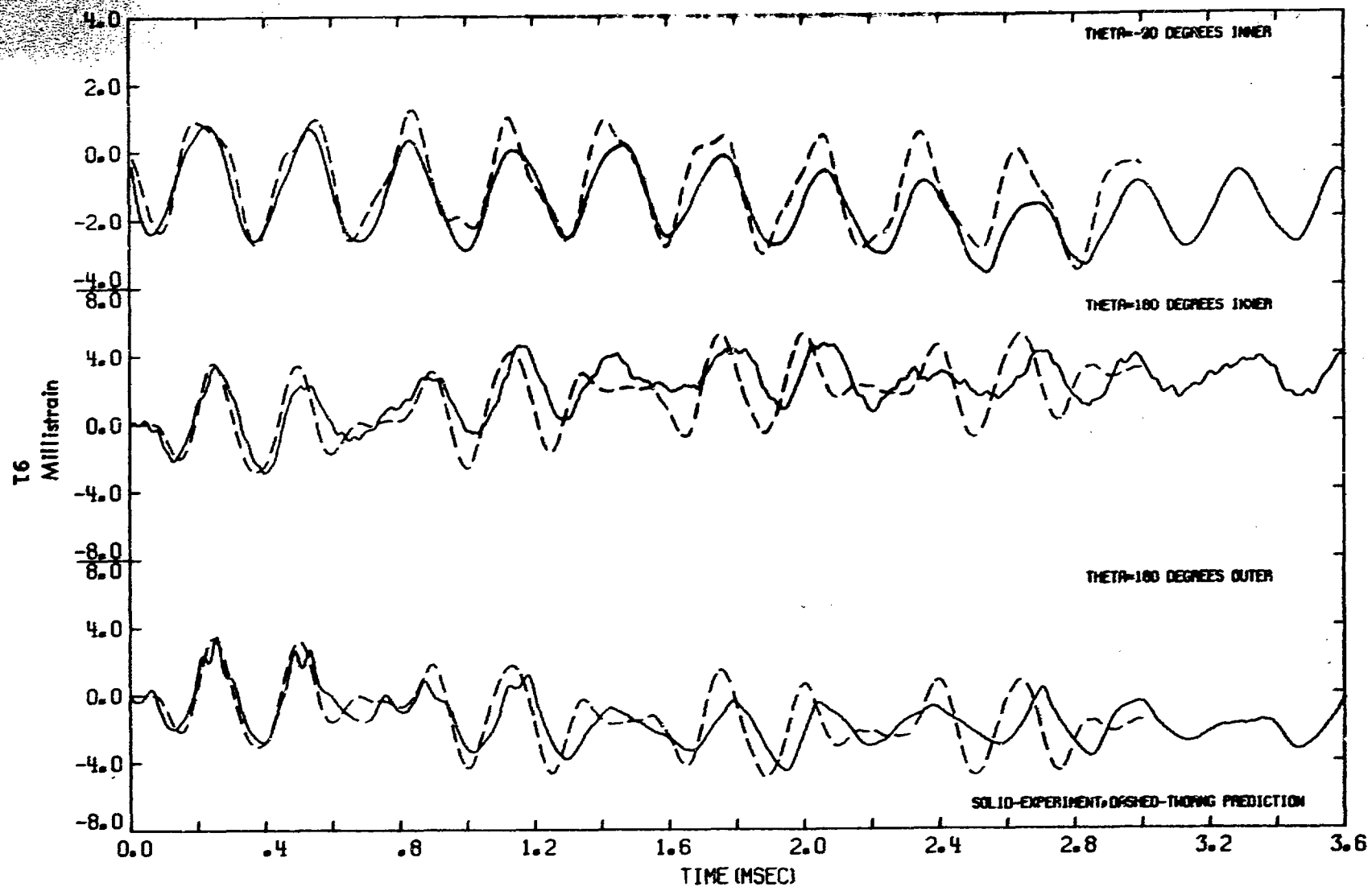

FIGURE 37b DYNAMIC RESPONSE CORRELATION FOR A 50.8CM O.D. ALUMINUM RING (SHOT 2-311)

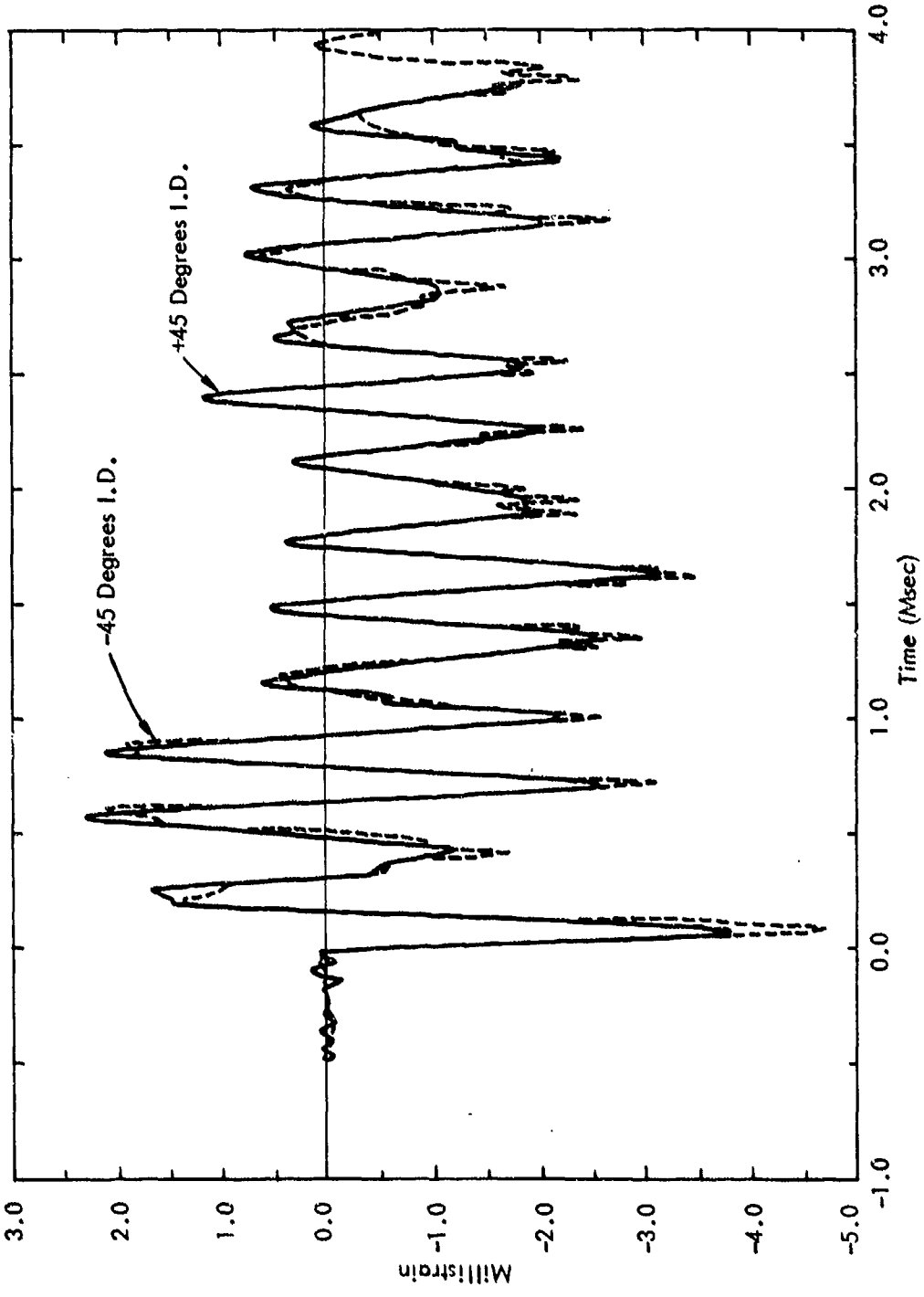

FIGURE 38 MEASURED STRAIN AT ±45 DEGREES FOR SHOT 2-311

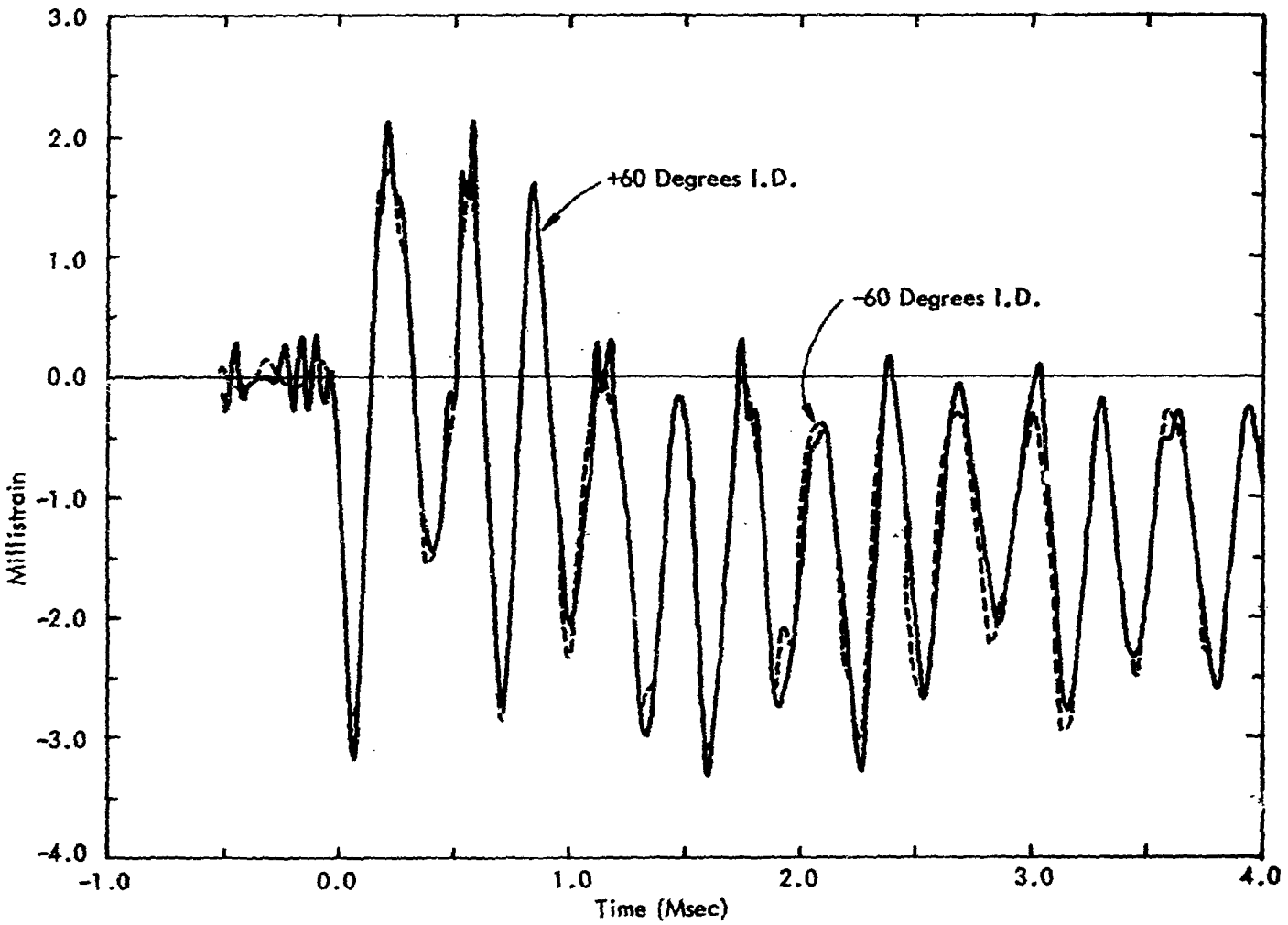

FIGURE 39 MEASURED STRAIN AT ±60 DEGREES FOR SHOT 2-311

CONFIDENTIAL

FIGURE 40 MEASURED STRAIN AT ±90 DEGREES FOR SHOT 2-311

curve near the yield point, but it is not likely that this would account for the discrepancy at 0^{o}. Since there is no visual evidence of gage lifting or spall due to prompt shock effects, it seems possible that the ring experienced a higher total impulse than that used for the theoretical predictions, i.e., 6.5 ktaps. Because shot no. 2-311 prefired, it was impossible to experimentally verify the total impulse with Dynafax motion measurements at 180^{o}.

Had a total impulse of 8.8 ktaps been used in the shot no. 2-311 analysis, the predicted first compressive peak at 0^{o} would have been about 6 millistrain; still well below the measured value. On shot no. 2-312, an experimentally-verified total impulse of 8.8 ktaps (7.9 ktaps prompt) led to visually observable incipient spall in the neighborhood of 0^{o}. Since there was no evidence of any spall in shot no. 2-311, we conclude that the total impulse must have been less than 8.8 ktaps, and the primary reason for the discrepancy between predicted and measured first compressive peaks at 0^{o} and 45^{o} remains in the realm of speculation. Difficulties like this emphasize the need for performing at least some low impulse level (below yield) tests when correlating different facilities. Analytical and experimental uncertainties seem to be directly proportional to load level.

The TWORNG predictions for shot no. 2-311 indicate that yield occurs (ε > 3.8 millistrain) at relatively late times at 0^{o} and 180^{o}. Confirmation that yielding did indeed occur is afforded by the observation that the ring was permanently deformed as a result of the impulsive loading. Measured permanent diameter changes for shot no. 2-311 (ring #3) are plotted in Figure 41. The similarity in amplitudes of the 3DQP and the aluminum ring #3 permanent deformations is largely coincidental.

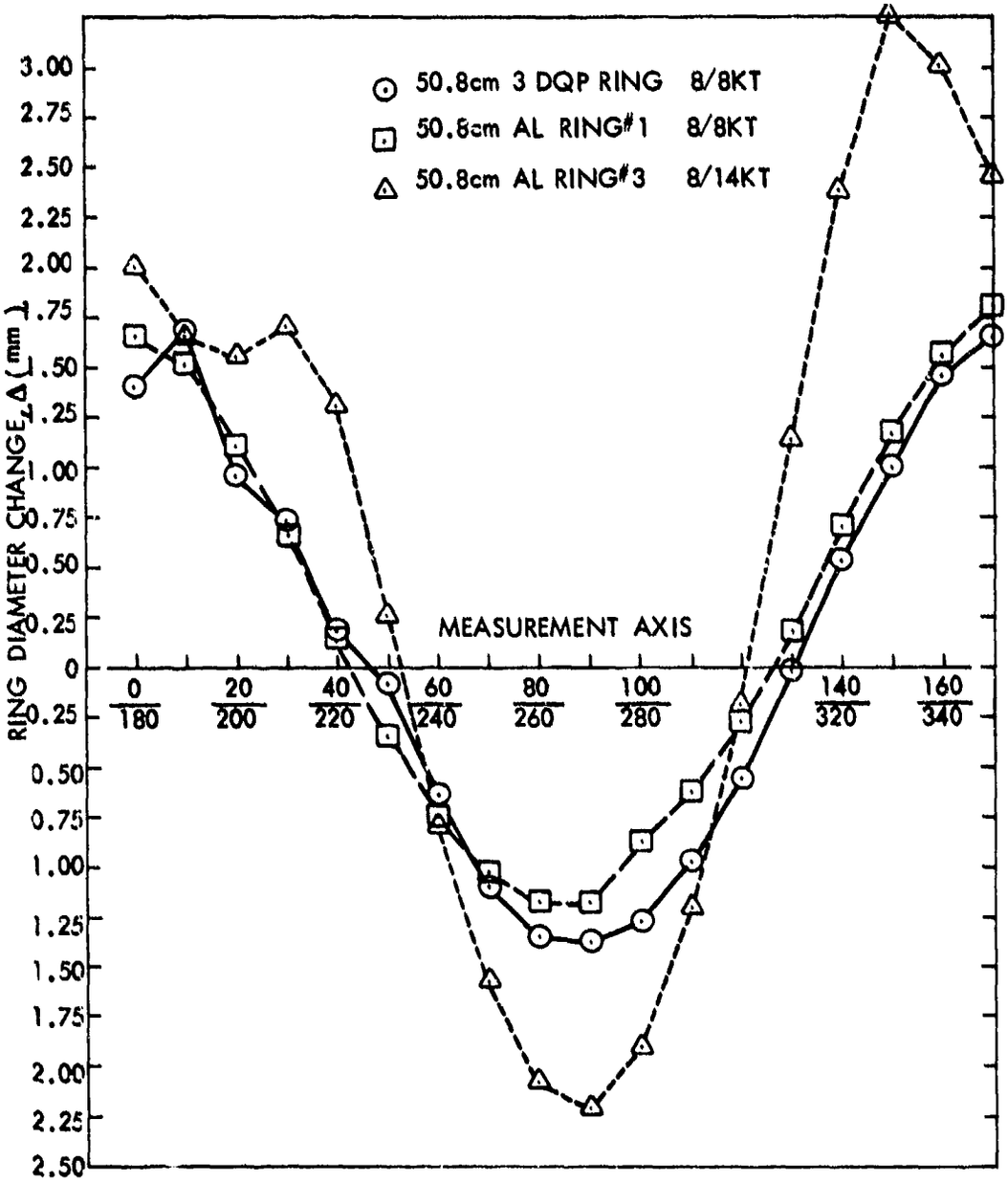

FIGURE 41 RING DIAMETER CHANGE, Δ VS θ

Correlations for the intermediate level impulse test (shot no. 2-312) are given in Figures 42(a) and 42(b). As mentioned previously, there was incipient spall in this ring at 0°, and the gages at $\pm 45^{\circ}$ failed, so only theoretical predictions are presented at these locations. Excellent load symmetry is again demonstrated by the measured strain outputs at $\pm 60^{\circ}$ and $\pm 90^{\circ}$. These outputs are shown in Figures 43 and 44 respectively.

The peak total impulse used for the shot no. 2-312 analytical predictions was 8.8 ktaps. This impulse was verified experimentally to within 5% by Dynafax motion measurements at 180°. Nevertheless, the correlations for shot no. 2-312 are somewhat poorer than those for the previous shot, especially on the back half of the ring.

Measured and predicted peaks, waveforms, and frequencies are in fair agreement for shot no. 2-312, but it is rather disturbing that the first compressive strain peak is underpredicted at 60° and overpredicted at the other locations. Again, the correlations would be improved to some extent by more careful analytical modeling of load distribution, yield point behavior, and damping. Permanent diameter change measurements were not made on this ring.

Predicted and measured strains for the high impulse test (shot no. 2-320) are given in Figures 45(a), 45(b), and 45(c). This ring spalled completely up to about ± 30-40°. Maximum material removal was about 1.27 mm at 0°. The spall was unsymmetric with respect to 0°, extending to 38° in the positive circumferential direction and to 28° in the negative circumferential direction. The lack of symmetry is reflected in the measured strain outputs at -60° (Figure 45(a)) and $+60^{\circ}$

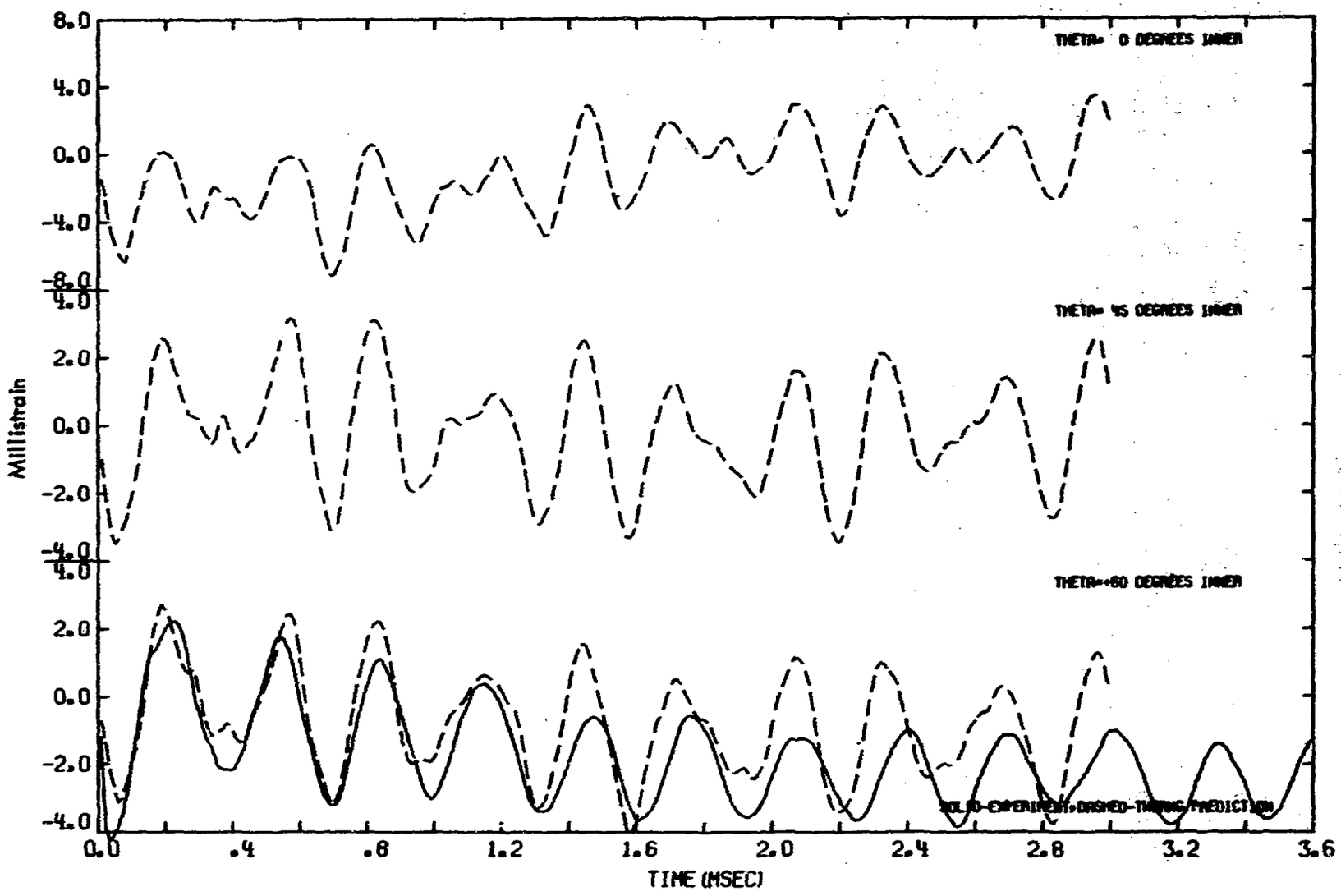

FIGURE 42(a) DYNAMIC RESPONSE CORRELATION FOR A 50.8CM O.D. ALUMINUM RING (SHOT 2-312)

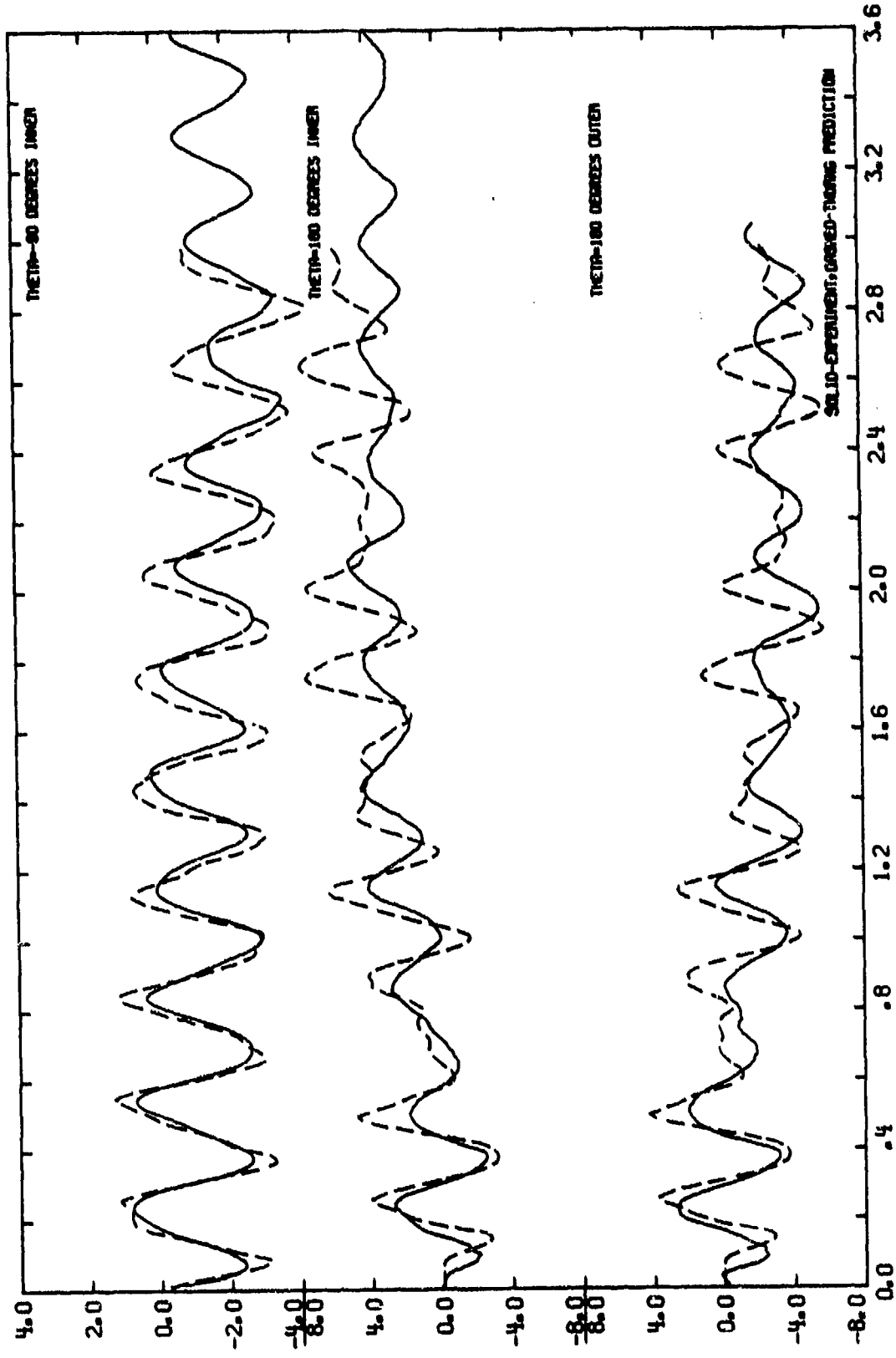

FIGURE 42(b) DYNAMIC RESPONSE CORRELATIONS FOR A 508CM O.D. ALUMINUM RING (SHOT 2-312)

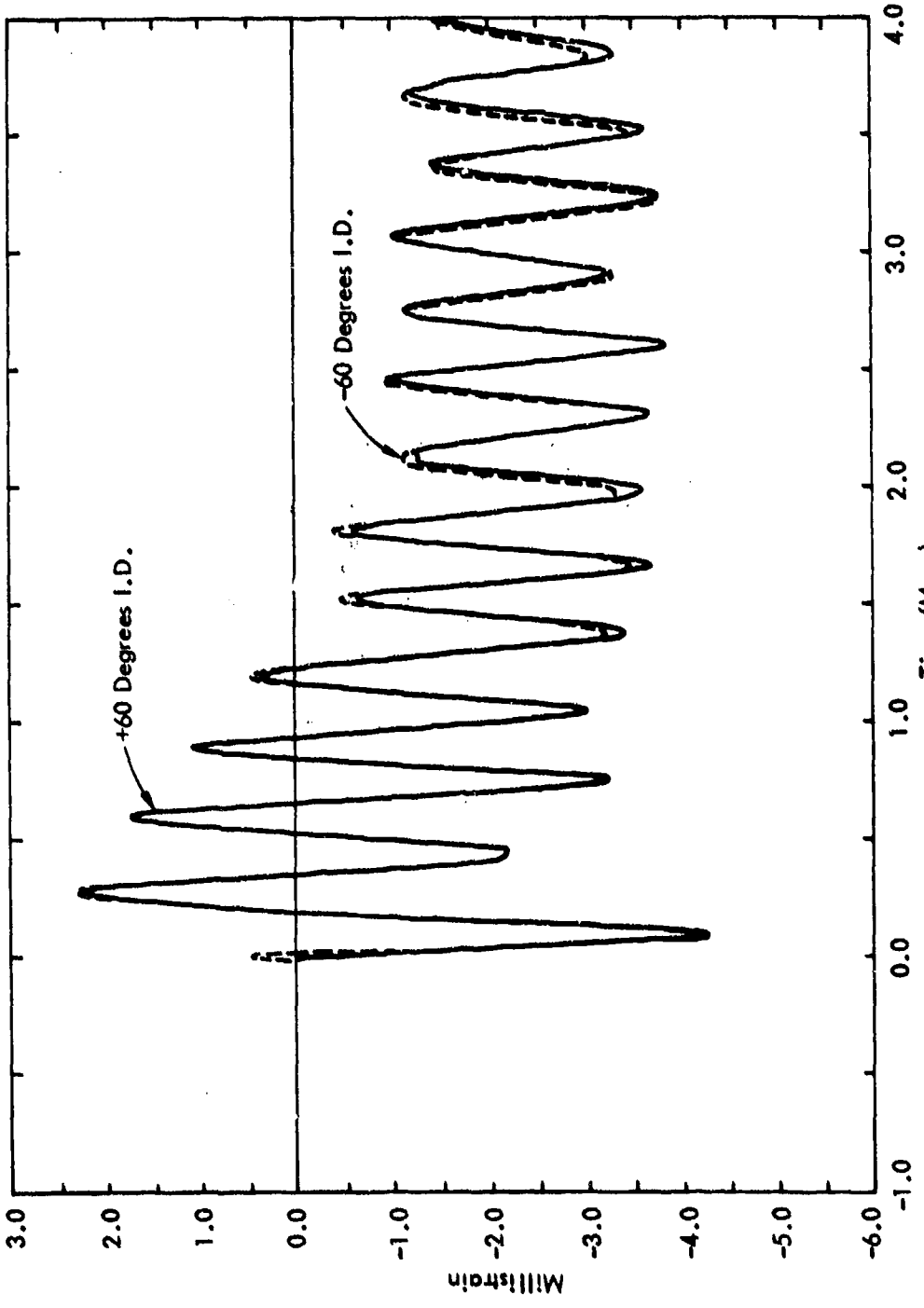

FIGURE 43 MEASURED STRAIN AT ±60 DEGREES FOR SHOT 2-312

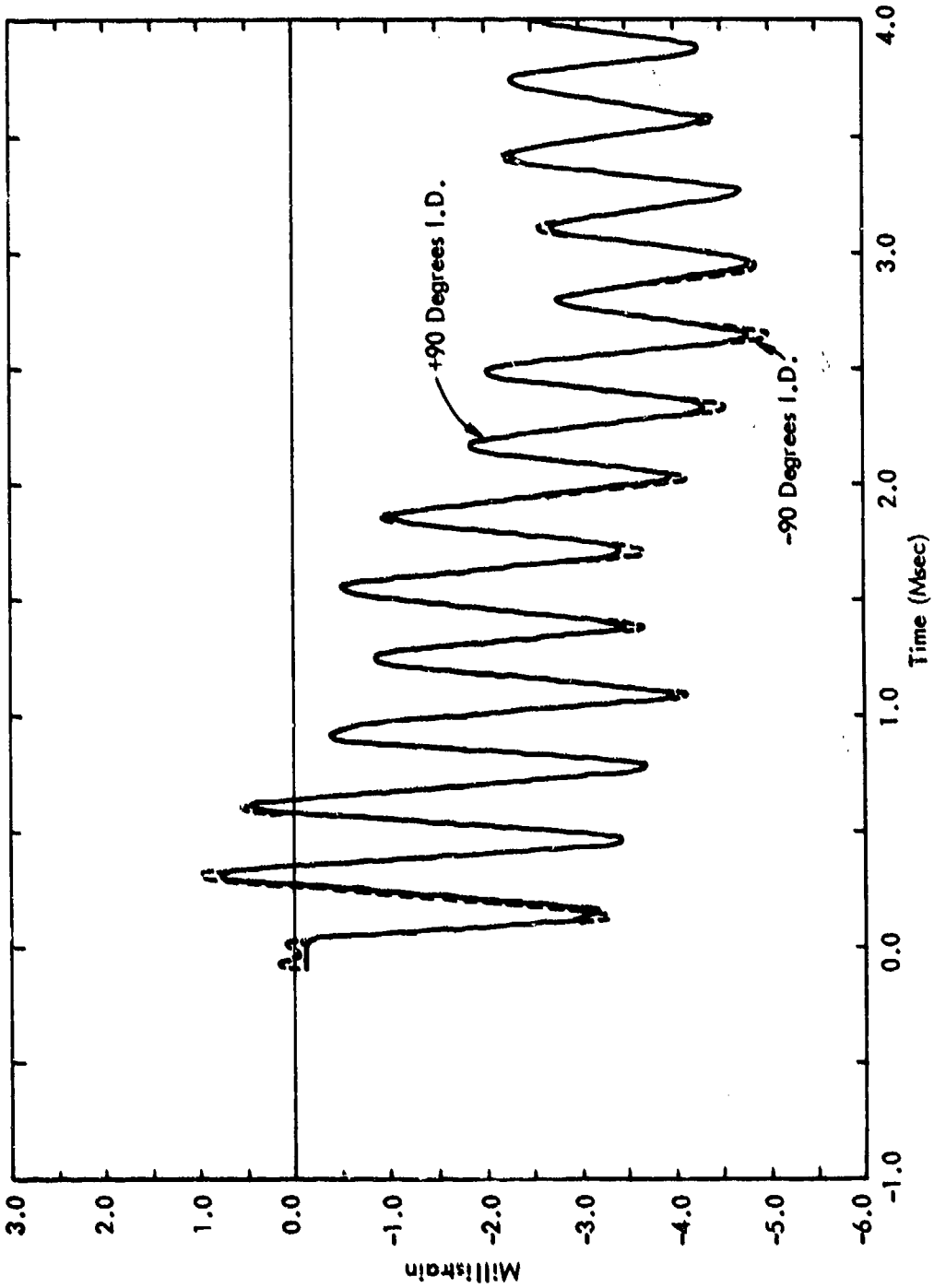

FIGURE 44 MEASURED STRAIN AT ±90 DEGREES FOR SHOT 2-312

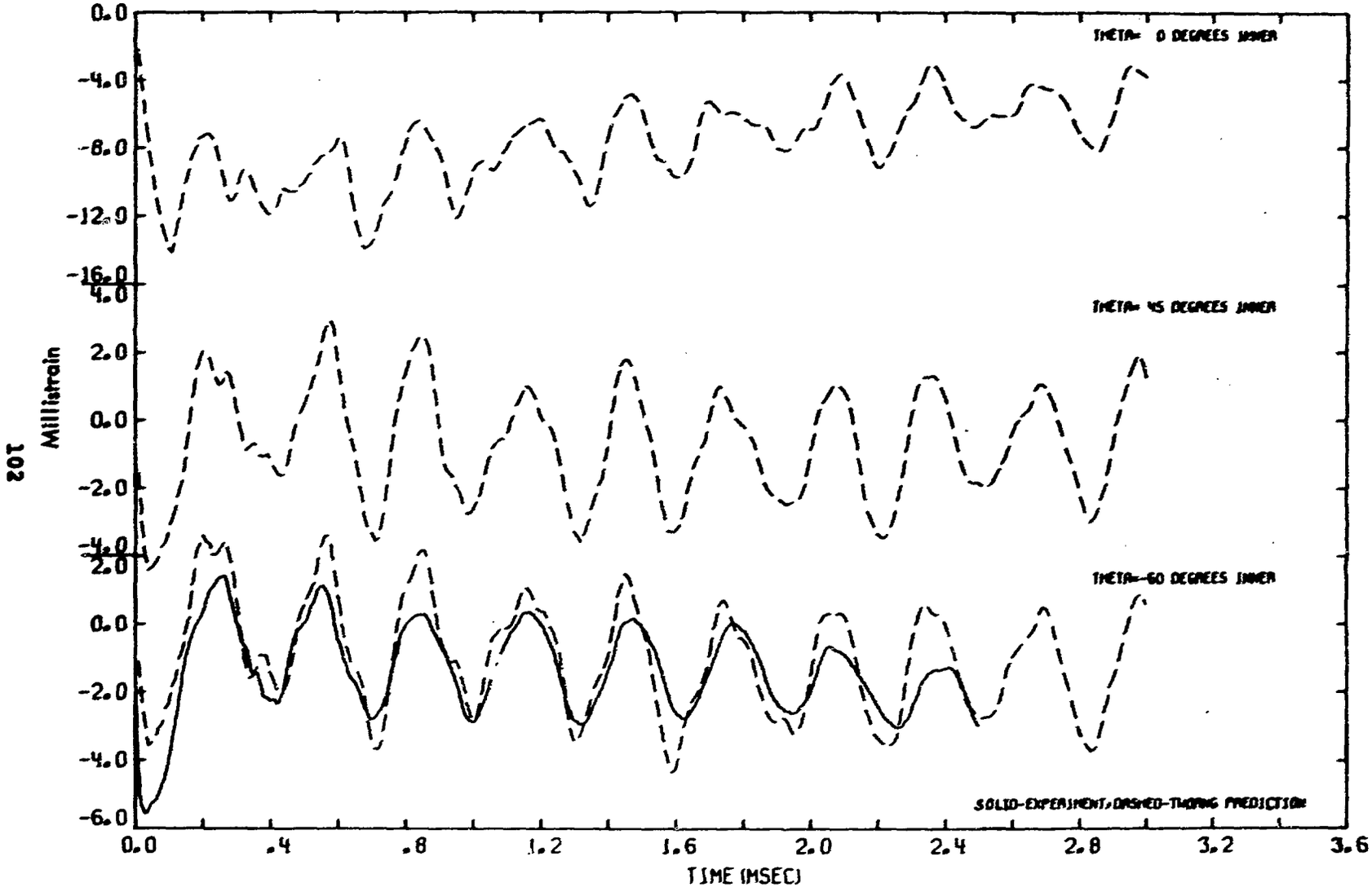

FIGURE 45(a) DYNAMIC RESPONSE CORRELATIONS FOR A 50.8CM O.D. ALUMINUM RING (SHOT 2-320)

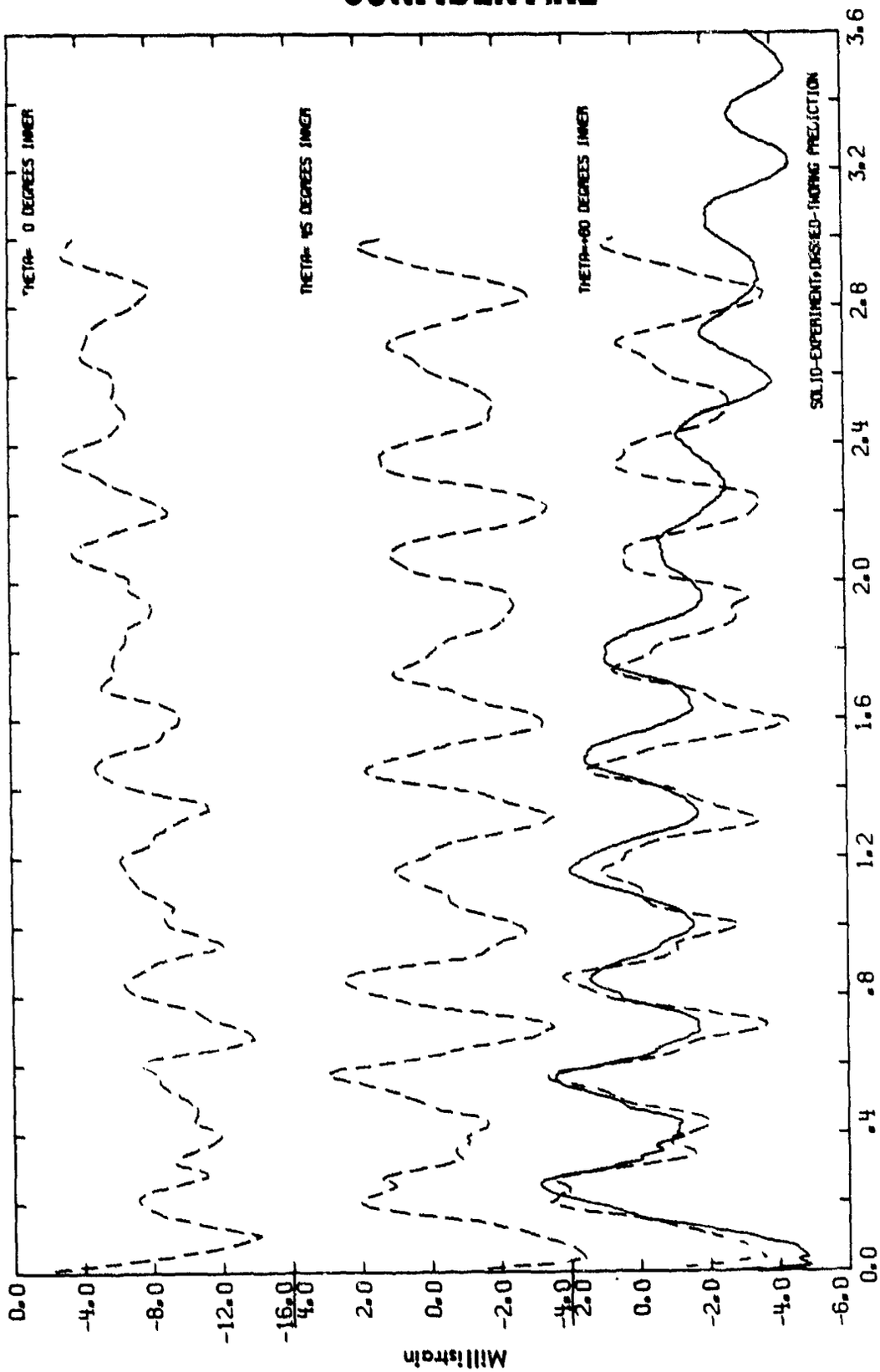

FIGURE 45(b) DYNAMIC RESPONSE CORRELATIONS FOR A 508CM O.D. ALUMINUM RING (SHOT 2-320)

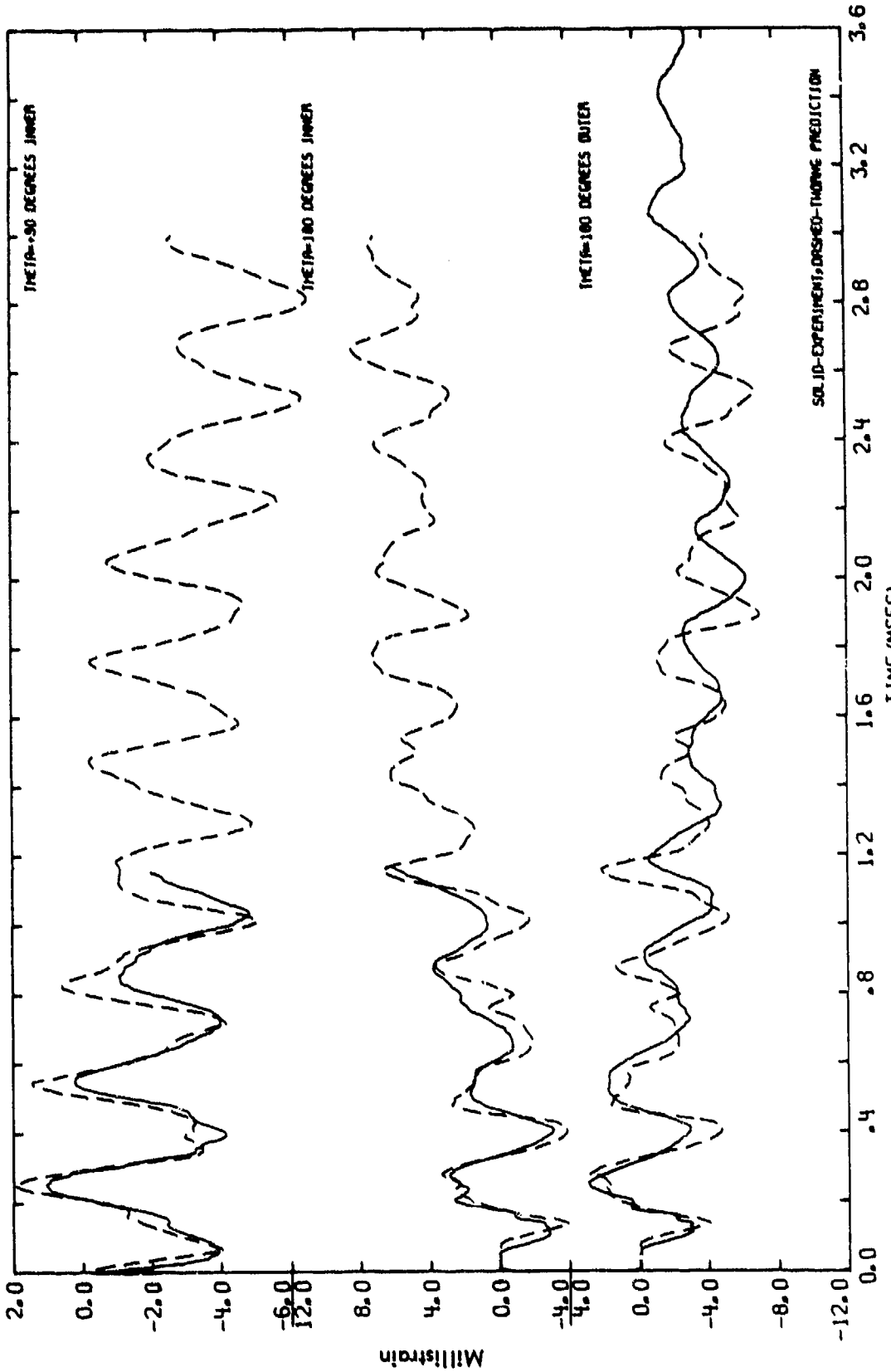

FIGURE 45(c) DYNAMIC RESPONSE CORRELATIONS FOR A 5.08CM O.D. ALUMINUM RING (SHOT 2-320)

(Figure 45(b)). Gages at 0°, $\pm 45^{\circ}$, and -90° were lost immediately, and the gages at $+90^{\circ}$ and 180° I.D. failed after about 1 millisecond.

Predictions for shot no. 2-320 were based on a peak total impulse of 13.5 ktaps. This impulse could not be conclusively verified experimentally because the Dynafax motion measurements did not exhibit the proper and expected flexural frequency content. The analytical model neglected the material removal due to the spall, but damping was increased to 0.6% in an effort to factor in some of the lessons learned from the prior aluminum ring correlations.

Even though material removal was neglected in the analytical model, the correlations for shot no. 2-320 are only of slightly lower quality than the previous aluminum ring correlations. Measured and predicted peaks, frequencies, and waveforms are still in fair agreement, although it appears that even more extensional damping is required at this impulse level. As with the intermediate level test, it is at least mildly disconcerting that first compressive strain peaks are underpredicted at $\pm 60^{\circ}$ but overpredicted at 180°. This may indicate a material modeling, rather than a load problem.

Yield is predicted at all locations for shot no. 2-320. Permanent diameter changes were measured for this ring (#1) and are plotted in Figure 41. The unsymmetric and rather peculiar deformed shape of ring #1 is thought to be related to the spall. Note that the permanent diameter change on the 90°-270° axis scales almost exactly with total impulse for the aluminum rings.

4.3.2 3DQP Ring

One 50.8-cm O.D. 3DQP ring was instrumented according to the same scheme used for the aluminum rings. The 3DQP ring had a wall thickness of 1.27 cm, and the impact conditions utilized a maximum flyer free run of 2.54 mm. Peak total impulse (including air cushioning) on the 3DQP ring was determined from Dynafax motion measurements to be 11.3 ktaps. This impulse is much higher than what would be expected from the Veldet calculations, i.e., 7.6 ktaps magnetic (7.4 ktaps prompt) plus 0.5 ktaps (approximately 197 taps per mm of flyer free run) for air cushioning. Reasons for the discrepancy between the Veldet calculations and the Dynafax measurements are not yet clear, but the higher (Dynafax) total impulse level was found to yield much better strain correlations.

Visual examination of the ring subsequent to the test revealed a line of failure (buckled and sheared hoop fibers) starting at about 8° on the outer surface and extending diagonally to about 28° on the inner surface. This failure, henceforth called a compression crack, was equally noticeable on both sides of the ring. Several small circumferential cracks or delams were also noticeable on both sides of the ring, indicating that the load was axially uniform. Permanent deformations and thickness changes were also measured and are reported in Figures 41 and 48, respectively.

The TWORNG predictions of 3DQP ring response were based on 8 integration stations through the thickness, 24 finite difference grid points in the half-circumference, and a 5 μsec time step. Since there was no rear surface material removal, a constant thickness was used.

The compressive and tensile Young's modulii, E_C and E_T, of the 3DQP were assumed to degrade linearly with impulse, both at the same rate. Virgin Young's modulii were determined from pre-test natural frequency measurements on the ring, using the KSC electromagnetic excitation (EME) facility. For a material with different modulii in tension and compression, it can be shown that natural frequencies are related to an effective modulus, E_e, given by

$$E_e = \frac{4\ E_T E_C}{E_T + 2\ \sqrt{E_T E_C} + E_C}$$

By using this expression in conjunction with the measured natural frequencies, and assuming $E_C \cong 0.725\ E_T$, in accordance with the SoRI static measurements on "A" process 3DQP described in Reference 5, the dynamic virgin Young's modulii were determined to be:

$$E_T = 27.4 \times 10^9\ N/m^2\ (3.97 \times 10^6\ psi)$$

$$E_C = 19.9 \times 10^9\ N/m^2\ (2.88 \times 10^6\ psi).$$

In tension, the 3DQP stress-strain behavior was taken as linear up to failure, but in compression the material was modeled as bilinear, with E_C governing for strains less than 1%, and $E_C^P = 0.90\ E_C$ governing for strains greater than 1%. This modeling also reflects static measurements on 3DQP. The compressive plastic or secondary modulus, E_C^P, was assumed to degrade linearly with impulse at the same rate as the primary modulii.

Material density was determined from the ring weight to be $1.622 \times 10^3\ kg/m^3$ (1.622 gm/cc), but property degradation at 0^o and damping parameters were determined a posteriori by essentially trial and error methods. It was found that the

measured strain data were best fit by assuming 20% degradation (80% retained modulii) at 0° and using 0.75% of critical damping in extension and zero flexural damping.

Predicted and measured strains for the 3DQP combined response test (shot no. 2-316) are shown in Figures 46(a) and 46(b). The gage at 0° lifted, and the gage at -90° failed, but load symmetry is amply demonstrated by the measured strains at $\pm 60^{\circ}$, shown in Figure 47.

Returning to Figures 46(a) and 46(b), it can be seen that predicted and measured strains are generally in excellent agreement with respect to peaks and waveforms, and are in good agreement with respect to frequencies. As mentioned previously, the correlation at 0° should not be taken too seriously because the strain gage at this location lifted as a result of early time stress wave propagation. There may also be some prompt shock effects on the 45° gages, as indicated by the post-test thickness change profile plotted in Figure 48. As a point of interest, it should be noted that the large thickness change at $+15^{\circ}$ does not correlate with any other measures of prompt shock material damage.

At locations less sensitive to prompt shock effects, i.e., 60°, 90°, and 180°, the first compressive peaks are slightly overpredicted. These discrepancies might be resolved, and the general quality of the correlations upgraded still further, by more careful analytical modeling of the load distribution, the nonlinear stress-strain behavior, and the degradation laws. Such effort does not appear to be warranted, however, in light of the fact that the discrepancies are generally within the experimental error bounds. The small differences between measured and predicted high (extensional) frequencies may be due to slight nonlinearities in the 3DQP

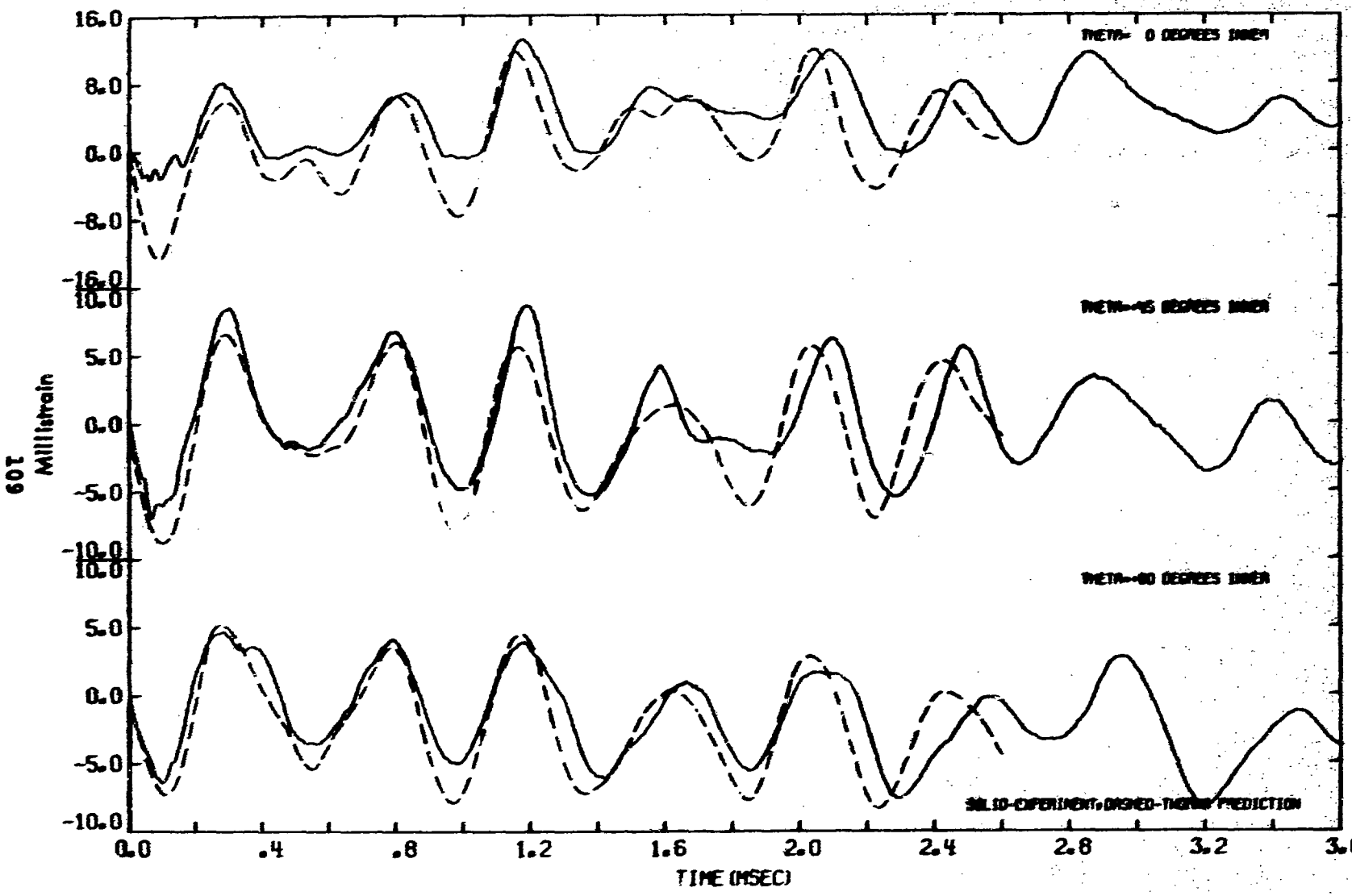

FIGURE 46(a) DYNAMIC RESPONSE CORRELATIONS FOR A 50.8CM O.D. 3DQP (SHOT 2-316)

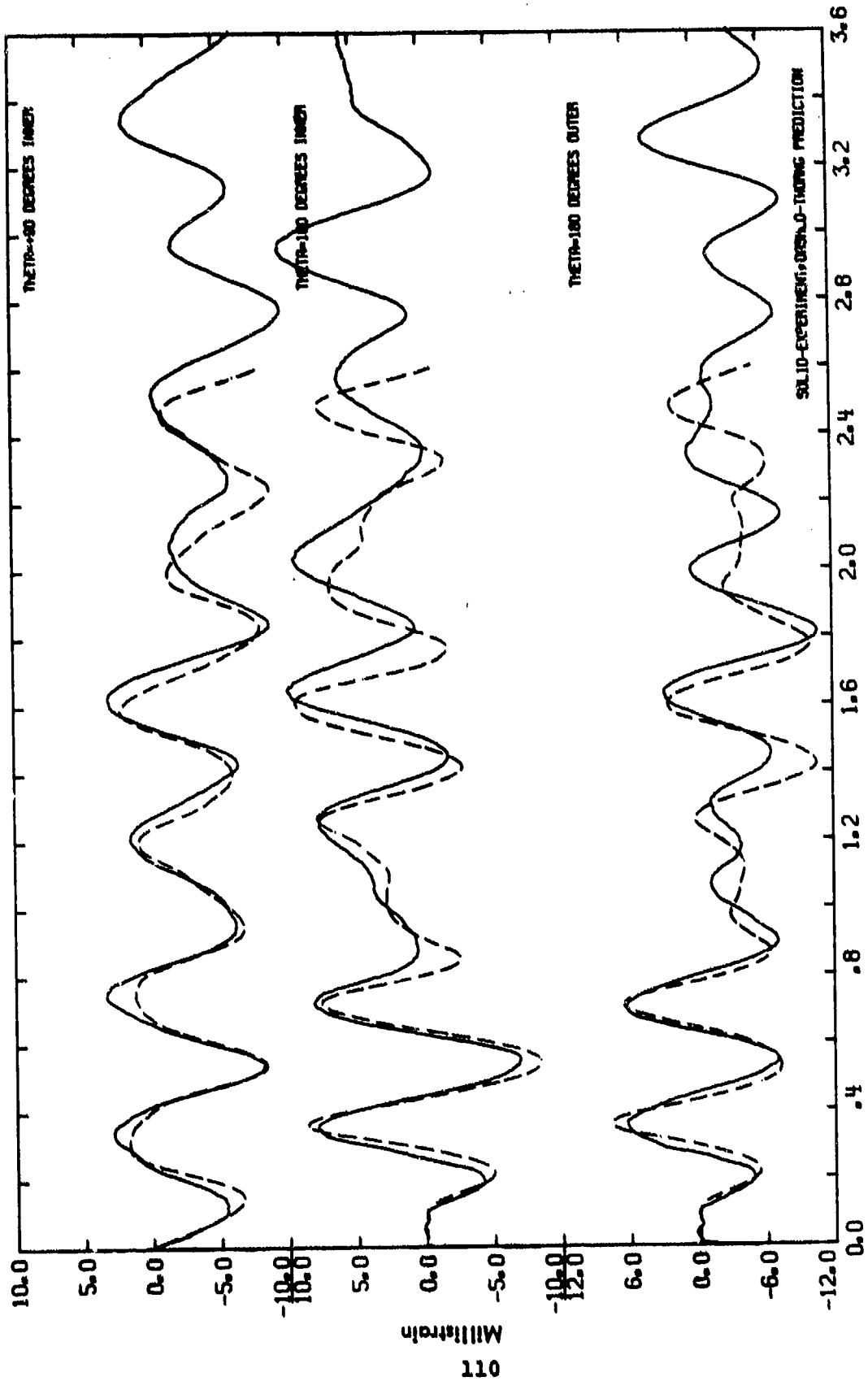

FIGURE 46(b) DYNAMIC RESPONSE CORRELATIONS FOR A 50.8CM O.D. 3DQP (SHOT 2-316)

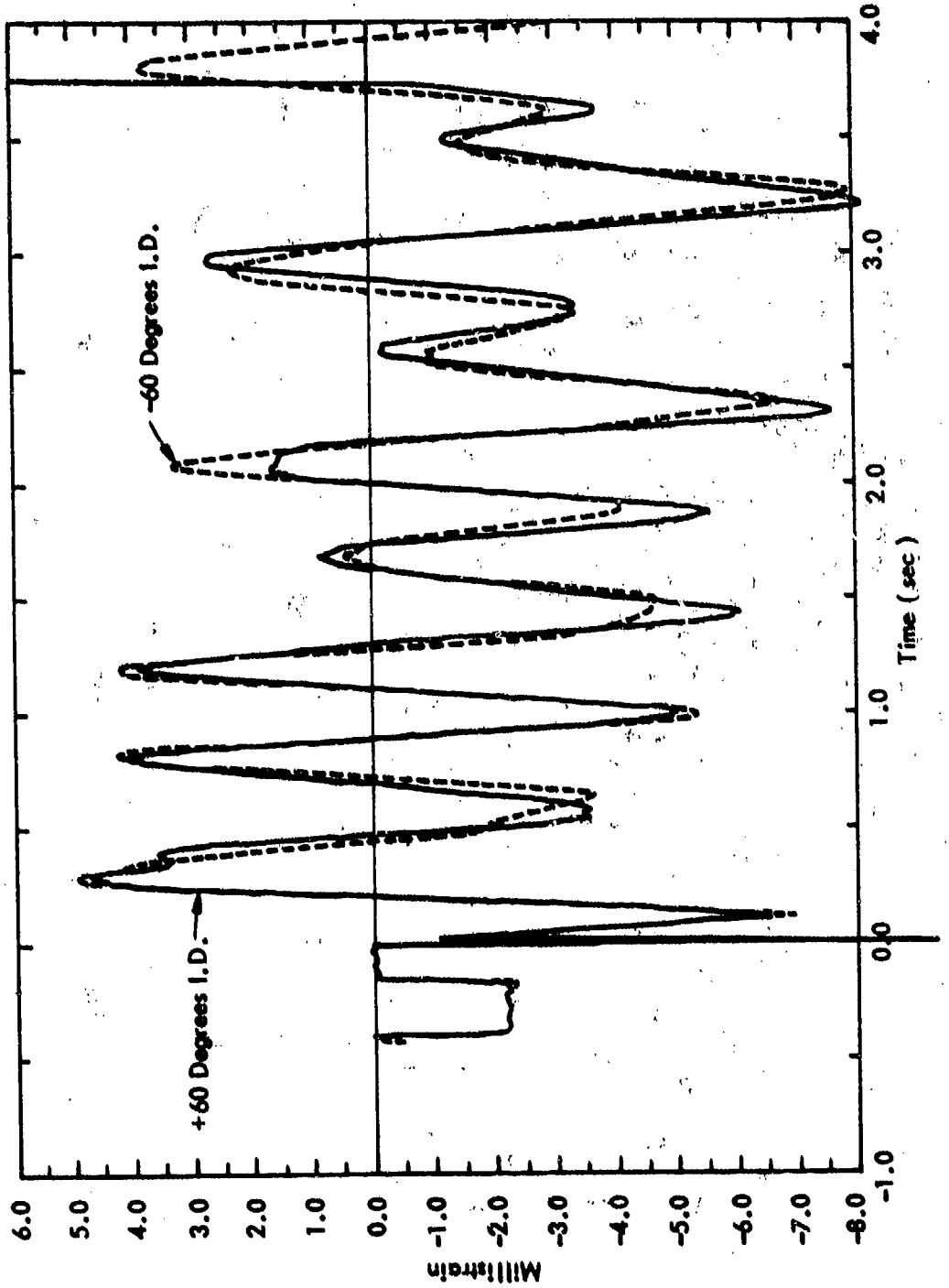

FIGURE 47 MEASURED STRAIN AT ±60 DEGREES FOR SHOT 2-316
50.8-cm DIAMETER 3DQP

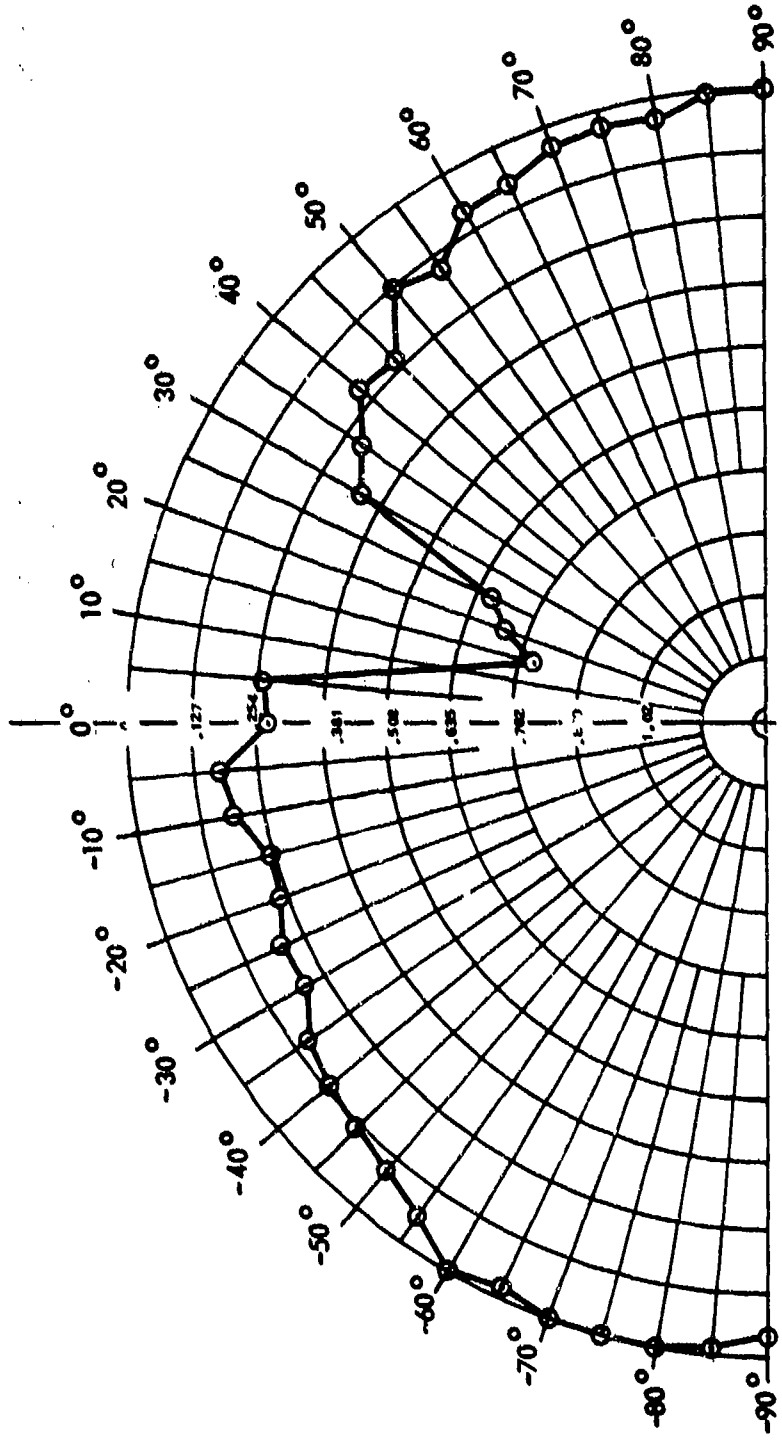

50.8 cm 3 DQP RING

FIGURE 48 RING THICKNESS CHANGE, δ VS CIRCUMFERENTIAL ANGLE

stress-strain curve which are not reflected in properties derived from EME (low strain level) data.

The measured permanent diameter changes for the impacted 3DQP ring are plotted in Figure 41. Except for the 15^{o}-195^{o} diameter, the ring has an oval shape similar to the aluminum ring hit at 7 ktaps. The unusually large diameter change at the 15^{o}-195^{o} axis is probably related to the large thickness change and compression crack at this location which were described previously.

SECTION 5.0

UGT SIMULATION STUDY EXPERIMENTAL RESULTS

5.1 UGT STUDY SAMPLE DESCRIPTION

Material was allocated for the UGT Simulation Study which was similar both in geometry and engineering properties to materials fielded underground. Material was supplied from rings designated 7.1.4. Ring dimensions were 19.56-cm diameter, 3.81-cm wall height, and 1.40-cm thick. Arc dimensions were 3.81-cm wide, 3.81-cm long, and 1.40-cm thick.

5.2 FLYER PLATE PERFORMANCE

The flyer plate dimensions were sized to correspond to the smaller dimensions of the test samples used for the UGT Simulation Study. The flyer plates used in these tests were 6.35-cm wide at 0° and sized in length to load over a 160° arc. From studies conducted by S^3 of the UGT environment[6], a 0.64-cm thick aluminum flyer was chosen to perform the UGT Simulation Study.

The prime impulse diagnostic for these shots were determined by the Veldet technique. TOA pins were run on each shot in order to provide a crosscheck on the impulsive load delivered to the sample. These TOA data are presented in Table 12 and are plotted in Figure 49. These data would suggest that the Rogowski coil impulse measurement is 10% high with respect to the TOA implied impulse (i.e., for a TOA impulse of 10,000 taps, the Rogowski coil would read 11000 taps). Possible explanations of this discrepancy can be obtained from consideration of the effects of flyer plate buckle and edge curl on TOA pins. Flyer plate buckle should be present to some degree due to the relatively thick flyer

TABLE 12 TOA VS IMPULSE DATA

VELDET IMPULSE
ROGOWSKI COIL
TOA PIN
0.064 CM THICK AL FLYERS
19.36 CM DIAMETER TARGETS

SHOT #	SYMBOL	FREE RUN (CM)	ROGO 0 TOA	ROGO 0 IMPULSE	PIN 0 TOA	PIN 0 IMPULSE
2-350	△	0.064	6.28	5.02	6.23	4.83
2-366	◊	0.064	6.18	6.03	----	----
2-367	▷	0.061	5.88	5.93	6.33	5.25
2-370	◇	0.055	5.56	5.90	5.61(1) 5.52(2) 5.48(3)	5.61 5.71 5.83
2-372	▱	0.053	5.18	6.51	----	----
2-356	▽	0.053	5.57	5.71	5.94(1) 6.28(2)	4.99 4.75
2-357	▽	0.053	5.58	5.71	6.06(1) 5.71(2) 6.00(3)	4.88 5.35 4.97
2-358	◇	0.053	5.63	5.67	----	----
2-359	▽	0.053	5.62	5.61	5.86(1) 5.75(2) 5.80(3)	5.12 5.32 5.21
2-349	△	0.050	6.28	5.02	6.23	4.83
2-368	▽	0.048	5.43	5.34	5.63(1) 5.83(2) 5.55(3)	4.90 4.75 4.95
2-352	⟹	0.041	4.84	5.09	5.46	4.27
2-369	◿	0.041	5.04	4.97	5.00(1) 5.31(2) 5.62(3)	4.78 4.59 4.28

CONFIDENTIAL

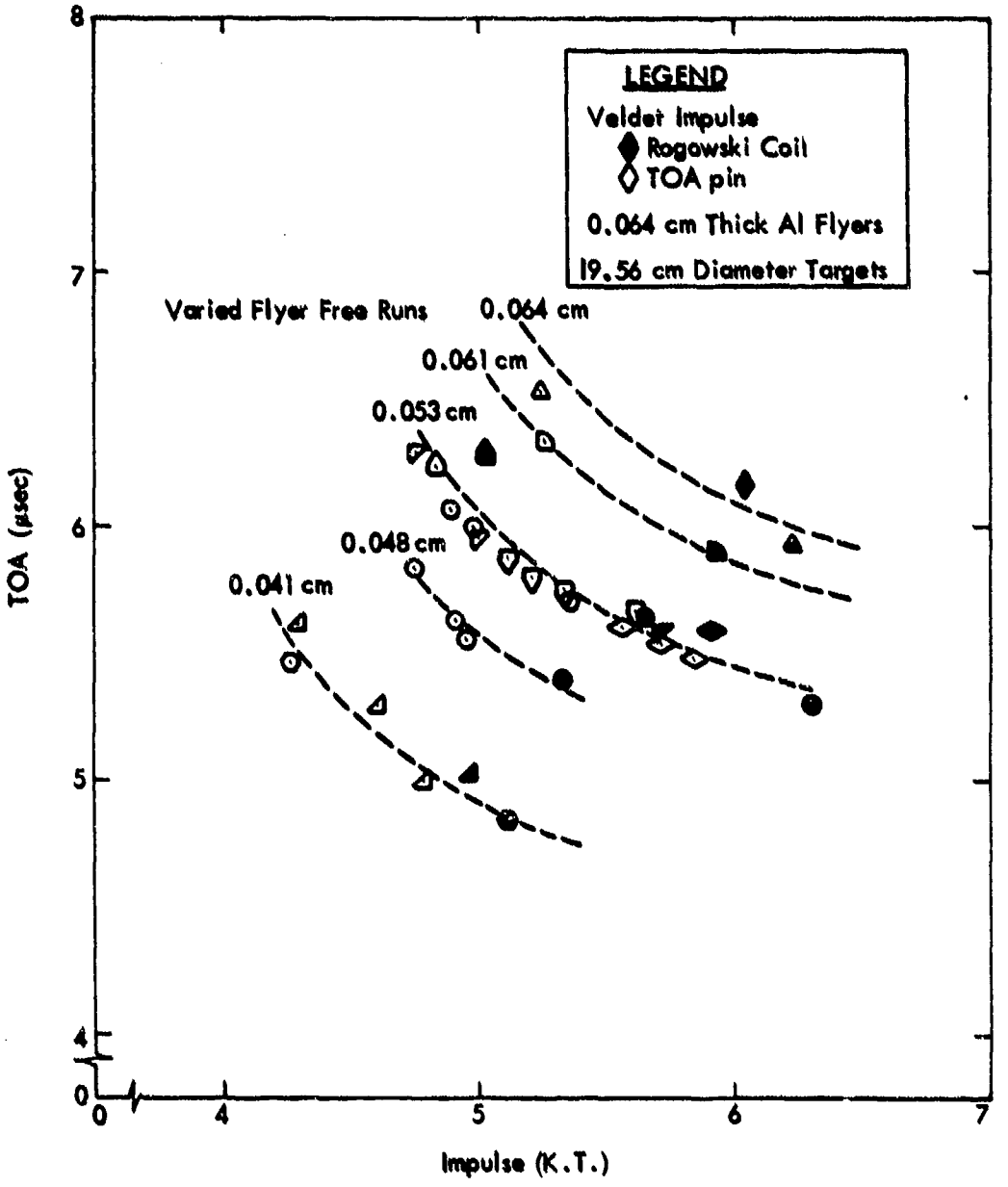

FIGURE 49. PIN VERSUS VELDET IMPLIED FLYER TOA AND IMPULSE DATA

being bent into a small 19.56-cm radius of curvature. Edge curl of the flyer should be present due to heating and field fringing because the flyer was driven to impulse values of 15,000 taps. Of these two effects, edge curl is thought to predominate, and an experimental program is being conducted to eliminate curl at these high impulse levels.

Two shots were performed in order to map the time-of-arrival around the circumference of a 19.56-cm diameter ring. PZT pins were positioned in an adiprene ring at 0°, $\pm 22.5^{\circ}$, $\pm 45^{\circ}$ and $\pm 67.5^{\circ}$ locations in order to monitor the flyer plate closure. These data are plotted in Figure 50. The worst case closure appears to be approximately 2.5 microseconds around the $\pm 67.5^{\circ}$ circumferential distance. Three pins were placed across the width of the ring at 0°, and the worst case closure was less than 100 nanoseconds. For structural response, the 2.5 microsecond closure time is adequate, being less than 10% of the time to form the first membrane peak; for material response criteria, 2.5 microseconds is a poor closure, and it must be hoped that for distances on the order of a few cell sizes the closure time is much smaller. The PZT pin maps at each 22.5° measurement station tend to support this thought. The 100 nanosecond closure measured across the width of the ring is excellent.

5.3 ARC AND RING DAMAGE DESCRIPTION

KSC impacted 11 3DQP arc samples in order to duplicate the one-dimensional damage experienced by Ring Z. Damage mode, damage location, and the degree of damage were the criteria used to judge if the damage produced in the arcs

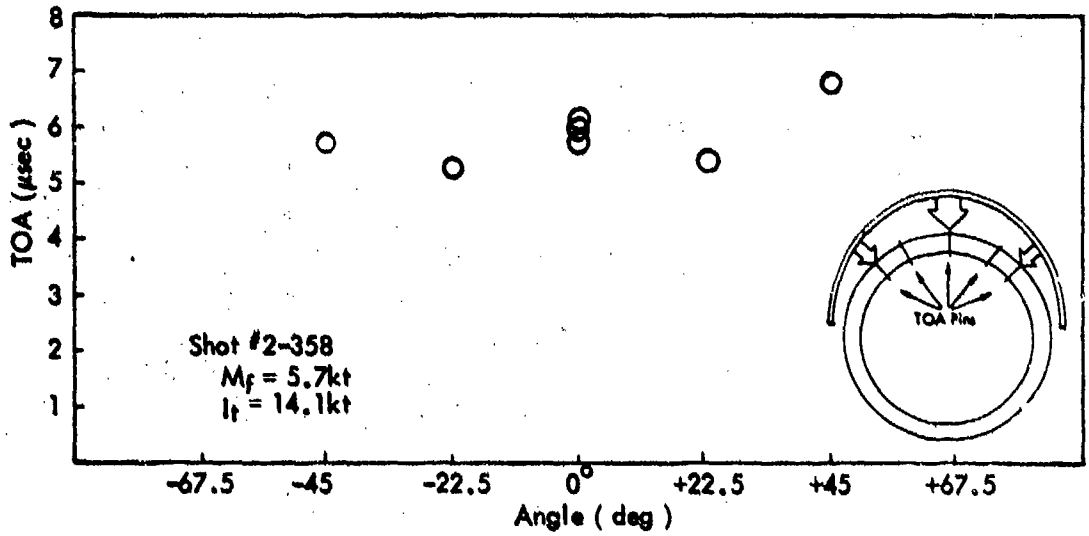

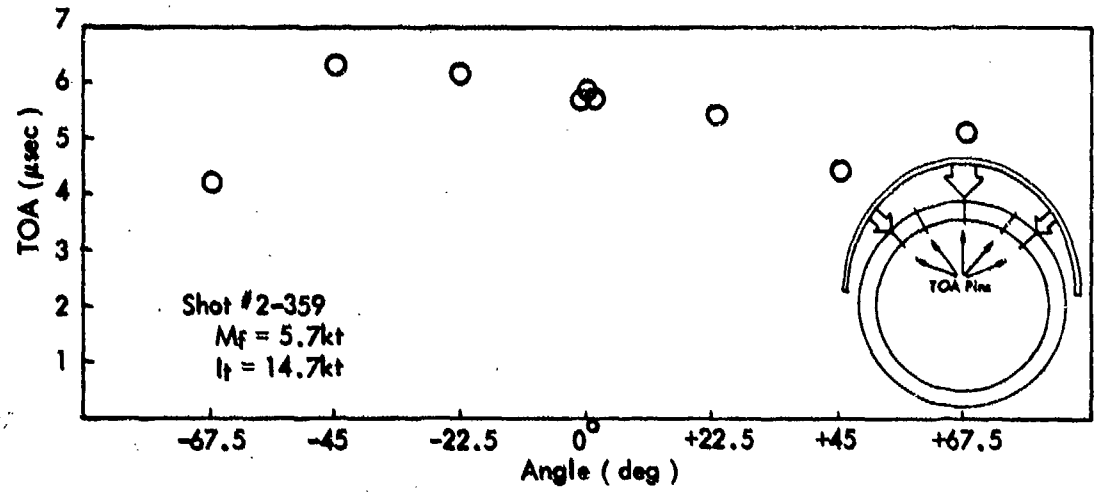

FIGURE 50. TIME OF ARRIVAL VS ANGULAR LOCATION - 19.56 cm DIAMETER FIXTURE RING FIXTURE CALIBRATION

compared favorably with the damage experienced by Ring Z. Ten shots were performed with 0.64-mm thick flyers, while one shot was performed with a 0.305-mm thick flyer. The flyer plate-to-target distance was varied from 0.41 mm to 0.64 mm in order to deliver a pre-selected sharp impulse followed by a post impact push to the sample.

From guidance furnished by S^3 (Reference 6), it was decided that the UGT environment could best be simulated by lengthening the loading time over which the impulse was delivered to the sample. In order to accomplish this, the KSC capacitor bank was modified by the addition of a ballast inductance. KSC realized that the capacitor banks could not be made to deliver an impulsive load over several hundred microseconds such as experienced in an UGT event. However, the discharge cycle could be modified rather easily to deliver impulse for tens of microseconds. The initial ballast inductor raised the bank inductance to 35 nanohenries, lengthening the discharge period to approximately 17 microseconds. With the ballast inductor in place, the capacitor bank output was altered by two different methods to achieve the desired waveforms. The first method produced 8 kilotaps in the flyer with a long duration, low amplitude post-impact magnetic push producing the additional 8 kilotaps. The second technique, called a series foil chop, produced an 8 kilotap flyer with a shorter duration, higher amplitude post-impact magnetic push producing the additional 8 kilotaps.

In order to more completely describe these different discharge techniques, the measured current trace was used to calculate the magnetic pressure waveform for each shot. The magnetic pressure drives the flyer plate across the free run distance, building impulse in the flyer; after impact the magnetic pressure continues to produce an impulsive load on the test sample.

The velocity of the flyer determines the front surface pressure, while the magnetic pressure waveform after impact determines the characteristics of the tail of the pulse. An idealized sketch of the resultant front surface pressure is shown in Figure 51. The two contrasting magnetic pressure waveforms produced by the two discharge techniques described above are overplotted in Figure 52; the magnetic pressure waveform used to accelerate flyers for the Facility Correlation Study are also shown in Figure 52 as a point of reference.

Two shots were performed utilizing the different post-impact tails just described. A most dramatic difference in the damage mode was produced even though the sharp and total impulse delivered to each sample was nearly identical. Photographs of the two damaged samples are shown in Figure 53 and provide a most vivid comparison of the damage modes. The first sample, K60, impacted with an 8 kilotap sharp impulse and a longer duration, lower amplitude tail, only suffered lifting of the axial and circumferential fibers at its rear surface. The mid-plane cracks and delaminations so prevalent in the 50.8-cm diameter arcs and also found in Ring Z were conspiciously absent (both visual and radiographic x-ray examination failed to reveal any mid-plane damage). The second sample, K62, also impacted with an 8 kilotap sharp impulse but followed by a shorter duration higher amplitude tail, suffered gross mid-plane damage and complete lifting of the circumferential and axial fibers from the rear surface. The mid-plane damage was so extensive that every radial fiber was broken, causing the sample to break into two pieces.

The facts were that, even though impacted by nearly identical impulsive loads, the resultant damage modes were vastly different. These results are explained by the

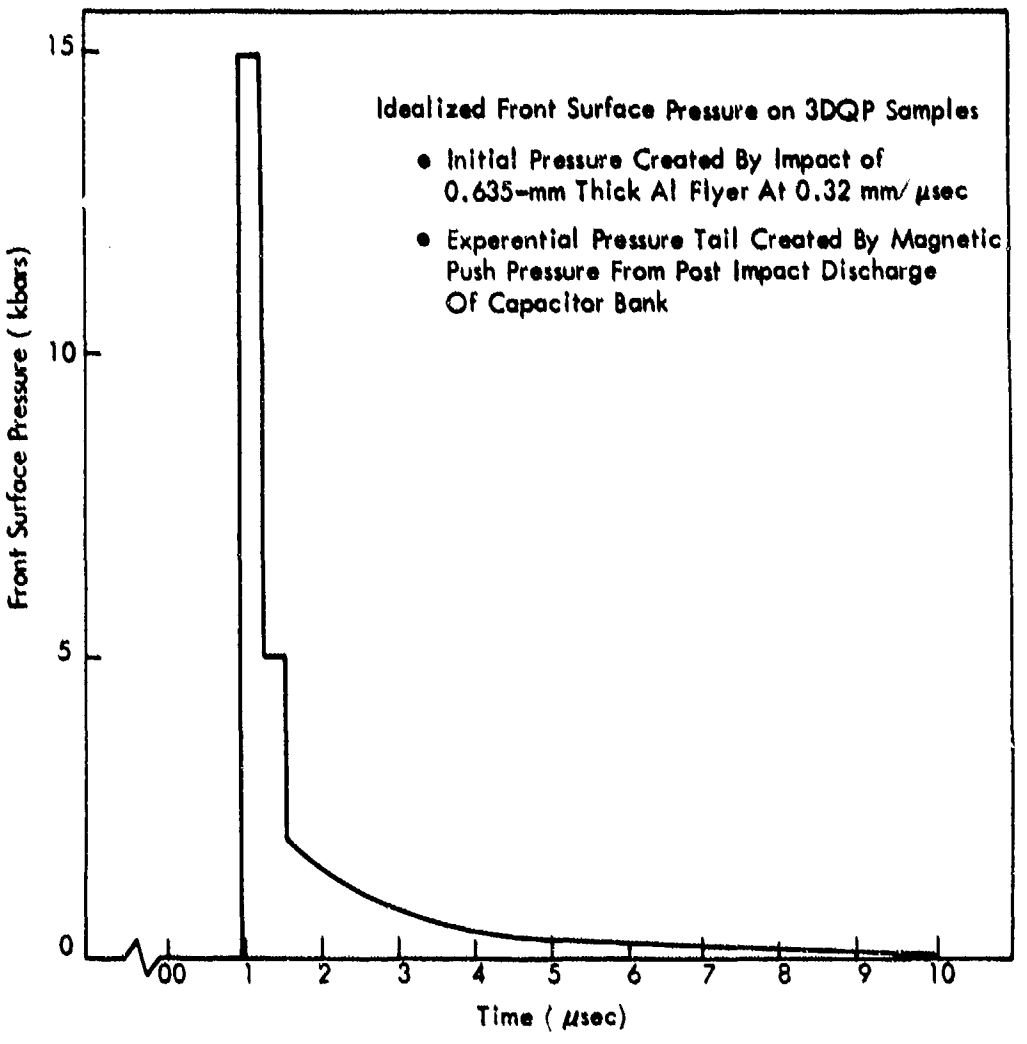

FIGURE 51. IDEALIZED FRONT SURFACE PRESSURE

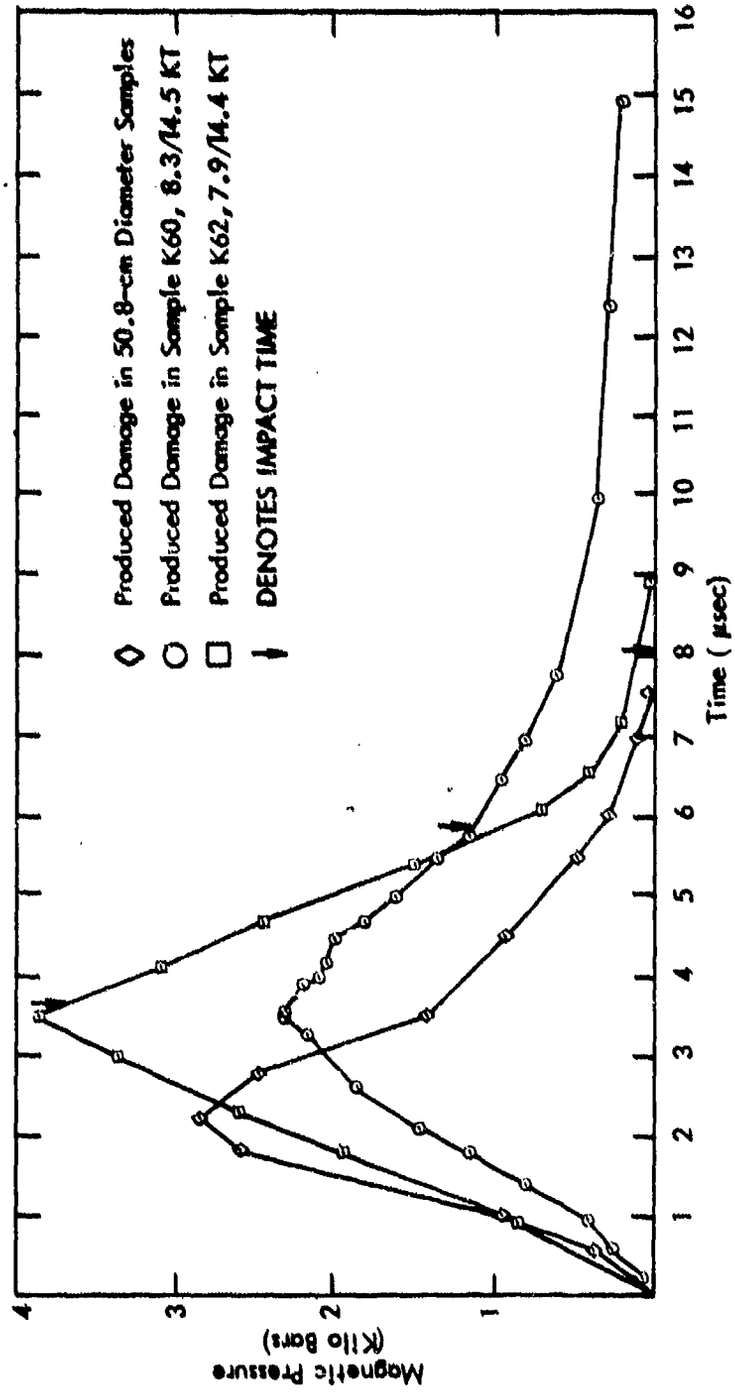

FIGURE 52. CONTRASTING MAGNETIC PRESSURE TIME WAVEFORMS USED TO PRODUCE DIFFERENT DAMAGE MODES IN 19.56-cm DIAMETER 3DQP SAMPLES

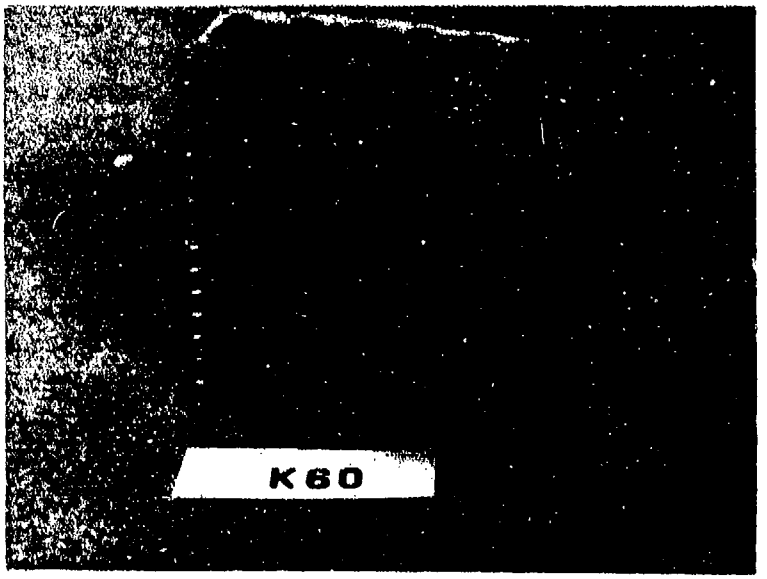

Damage Produced By Flyer Plate Impact With Long Duration, Low Amplitude Magnetic Push , 8.3 KT Sharp Impulse, 14.5 KT Total

Damage Produced By Flyer Plate Impact With Short Duration, High Amplitude Magnetic Push, 7.9 KT Sharp Impulse, 14.5 KT Total

FIGURE 53 DAMAGE MODES PRODUCED BY DIFFERENT POST IMPACT MAGNETIC IMPULSE TAILS

shock wave physics argument that different thickness flyer plates can cause different damage in test samples, even though the samples might receive the same impulse. This effect is caused, of course, by the different pressure-time histories presented to the sample by the different thickness flyer plates. Through the use of complex discharge waveforms from the AWRE and KSC capacitor banks, this same argument has been advanced to suggest that identical thickness flyer plates, delivering identical impulsive loads, can be used to produce different damage modes by varying the post-impact magnetic push. The explanation for this effect is again given by the fact that the post-impact magnetic push alters the pressure-time history delivered to the sample. The utility of these data became obvious, that the proper tailoring of the post-impact magnetic push might lead to a duplication of the damage experienced in the UGT environment. In fact, as will be shown later, this was accomplished.

Additional material was allocated to further refine the damage in arc samples and to provide samples for x-cut quartz instrumented lats and strain gaged rings. KSC subsequently tested these additional arcs with a larger ballast inductor, further lengthening the duration of the discharge waveform in an attempt to subdue the damage patterns experienced by K62. Initial shots indicated that this new capacitor bank configuration, with an inductance of approximately 100 nH, caused damage similar to that experienced by Ring Z. The capacitor bank was left in this configuration for all the remaining shots since this configuration so successfully achieved the desired damage mode described below.

The arcs impacted using these test methods suffered both rear surface and mid-plane damage modes. The rear surface damage typically consisted of lifting of lateral fibers to a depth of a few plies and cracking of the phenolic causing delaminations and/or near delaminations to a depth of 5 to 10 plies (0.127 cm to 0.254 cm in depth from the rear surface). The mid-plane damage was typically located between 0.3 cm and 0.6 cm from the front surface of the samples and consisted of cracking in the phenolic to form delaminations or near delaminations in the mid-section of the samples. An edge-view photograph and radiographic x-ray of typical sample damage are shown in Figure 54.

A group of four arcs were tested which produced rear surface damage more severe than experienced by Ring Z, while the mid-plane damage ranged from too light to too severe in comparison with Ring Z. Interestingly, the magnetic pressure waveforms for the four shots were almost identical. Even though the loading waveforms were the same, two samples suffered too little mid-plane damage, while two other samples suffered approximately correct mid-plane damage. These four waveforms are emphasized by the shaded area in Figure 55, which presents the magnetic pressure-time histories for all the arc and ring shots. These data lead SoRI[2] to suggest that the mid-plane damage at this magnetic pressure loading level were being dominated by variations in the strength of the material. SoRI suggested that if 10 rings were loaded in this manner, five might show mid-plane damage while the other five would fail to show mid-plane damage. One can conclude that the loading conditions represented by the magnetic pressure waveforms falling on the lower end of the shaded zone of Figure 55 form a lower boundary for producing incipient damage.

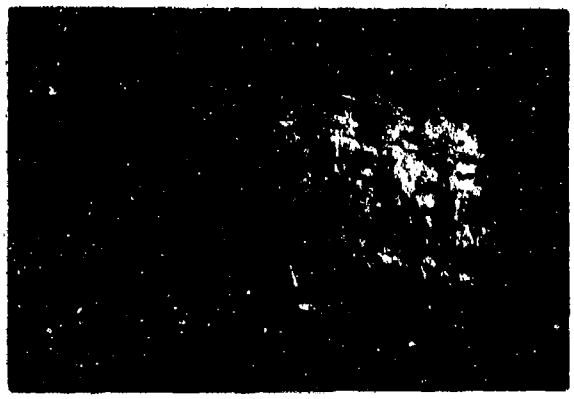

Grazing Light Photograph
of Sample Edge

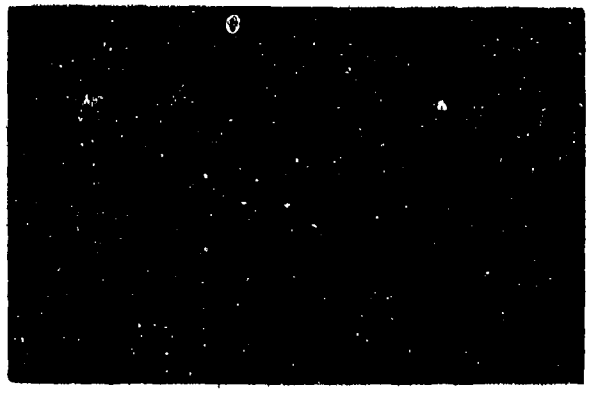

X-Ray Radiograph

FIGURE 54. TYPICAL MID-PLANE AND REAR SURFACE DAMAGE OF 19.56-cm DIAMETER 3DQP SAMPLES

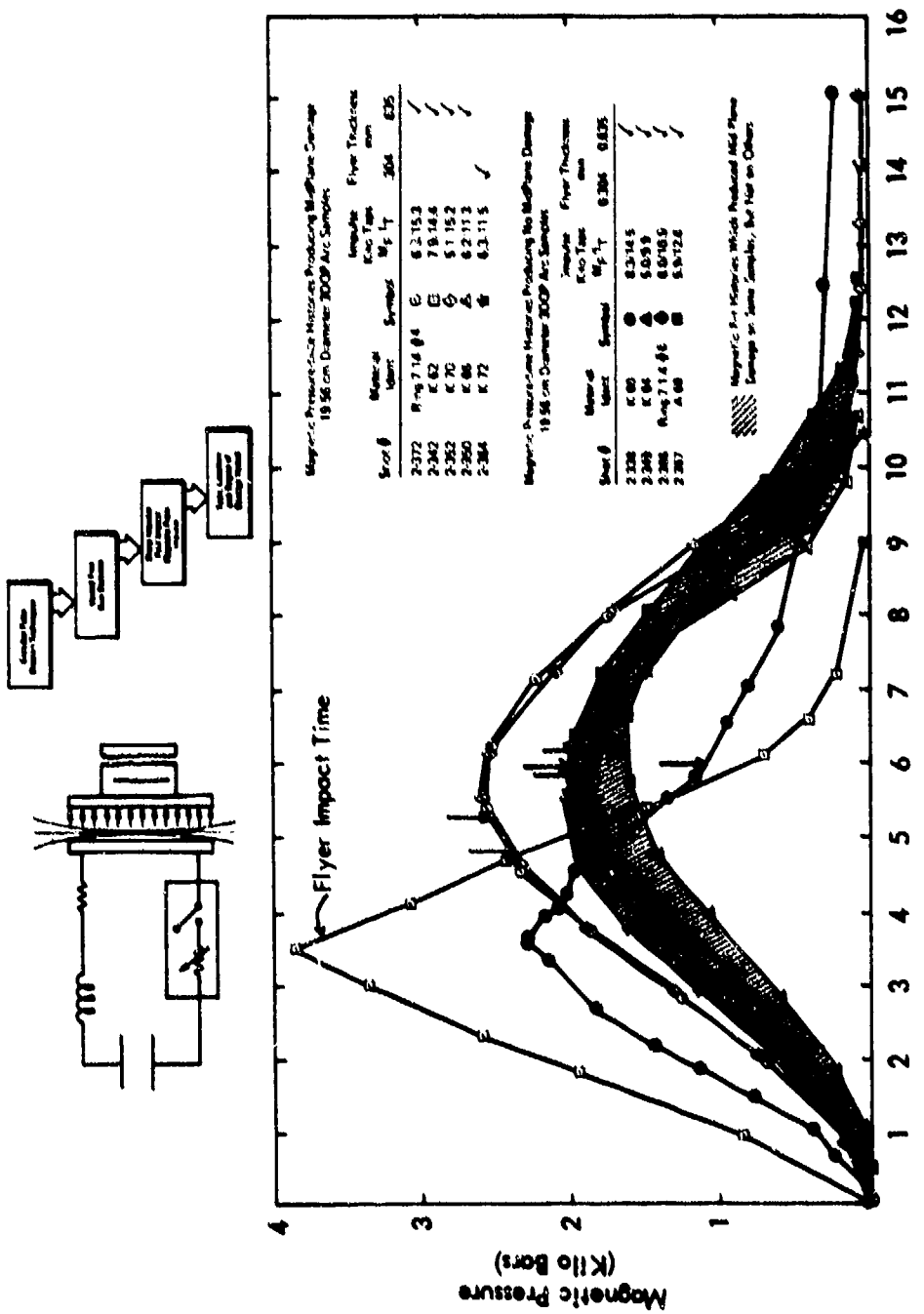

FIGURE 55. CONTRASTING MAGNETIC PRESSURE-TIME WAVEFORMS USED TO PRODUCE DAMAGE ON 19.56-cm DIAMETER 3DQP SAMPLES

A shot on sample K70 produced strong mid-plane damage (but rear surface damage which was a proper duplication of that experienced by Ring Z). Because the magnetic pressure waveform was also larger, this shot produced a more severe loading condition and more severe mid-plane damage than had been previously experienced. For this reason, K70 served as an upper boundary for mid-plane damage. The post-test x-rays of selected samples, shown in Figure 56, point out the range of damage produced by the bounding magnetic pressure waveforms. The radiographs show that samples A69 and K64 suffered relatively little mid-plane damage. Sample K66 suffered about the right amount of mid-plane damage, and sample K70 suffered mid-plane damage which was too strong. The damage depicted in the radiographs duplicates properly the location of mid-plane damage while bounding the severity of damage. In summary, the range of damage modes just described was judged sufficient to bound Ring Z damage such that ring shots could be performed. Table 13 provides a summary of all the arc and ring damage shots performed on the UGT Simulation Program.

To assess the realism of the impulse vs. time being delivered to the sample by the pressure-time curves shown on Figure 55, a hydrocode calculation was performed which modeled the UGT environment experienced by Ring Z. The calculation was performed using the KSC Puff VI code. The impulse vs. time of the flyer plates were obtained by assuming the idealized P vs. t waveform shown in Figure 51. The flyer plate momentum is transferred to the sample in approximately 4 flyer plate transit times after which the momentum is assumed to be delivered by the measured late time magnetic waveform. The UGT and selected mag flyer impulse vs. time curves are plotted in Figure 57. The predicted UGT curve is closely approximated by the K66 experiment which closely duplicated the UGT damage. Thus, the simulated waveforms are generating realistic impulse vs. time curves.

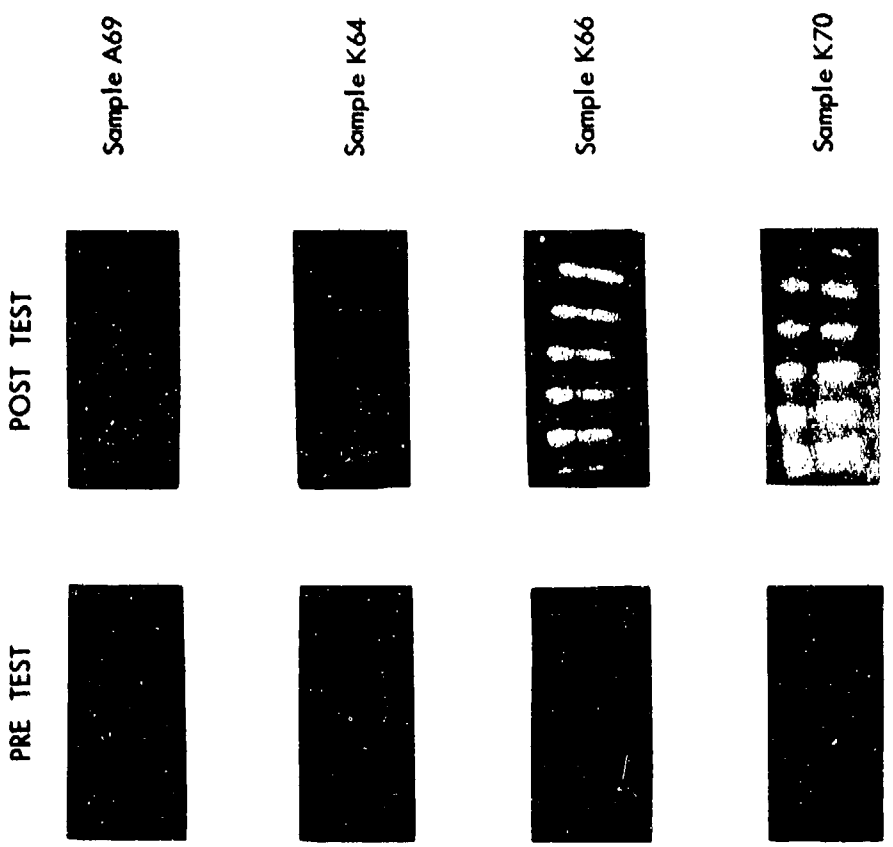

FIGURE 56. PRE AND POSTTEST RADIOGRAPHS OF SELECTED SAMPLES SHOWING RANGE OF DAMAGE PRODUCED IN 3DQP SAMPLES

TABLE 13 DAMAGE SHOT SUMMARY

19.56 cm DIAMETER, 1.397 THICK 3DQP ARCS AND RINGS

SHOT #	SAMPLE #	FLYER THICKNESS		BANK CONFIGURATION				IMPULSE (TAPS)		PRESSURE (KILOBARS)	DAMAGE EVALUATION RELATIVE TO RING 2	
		0.0305 CM	0.0635 CM	35NH CB[2][1]	100NH CB[2][1]	35NH FC[3][1]	100NH FC[3][1]	M_F	I_T	P_p	R.S.[4] (PLIES)	M.D.[5]
2-338	K60		✓	✓				8.3	14.5	2.3	6 Slightly heavy	Too little
2-342	K62		✓			✓		7.9	14.4	3.8	7 Slightly heavy	Much too severe
2-349	K64		✓				✓	5.0	9.9	1.6	8 Slightly heavy	Too little
2-350	K66		✓				✓	6.2	11.3	2.0	7 Slightly heavy	About right
2-351	K68		✓				✓	2.6	4.5	6.5	BANK PREFIRE	
2-352	K70		✓				✓	5.1	15.2	2.6	6 Slightly heavy	More severe
2-364	K72	✓					✓	6.3	11.5	2.0	12 Too severe	Too severe
2-365	A61		✓		✓			5.3	13.5	1.8	~10 Too severe	Too little
2-367	A69		✓				✓	5.9	12.6	2.0	~10 Too severe	Too little
2-366	7.1.4 #6Ring		✓				✓	6.0	10.9	1.9	7 Slightly heavy	Too little
2-372	7.1.4 #4Ring		✓				✓	6.3	15.3	2.6	4 Correct	Slightly higher

[1] NH is nanohenry.

[2] CB is crowbar.

[3] FC is foil chop.

[4] RS is rear surface.

[5] MD is mid delamination.

CONFIDENTIAL

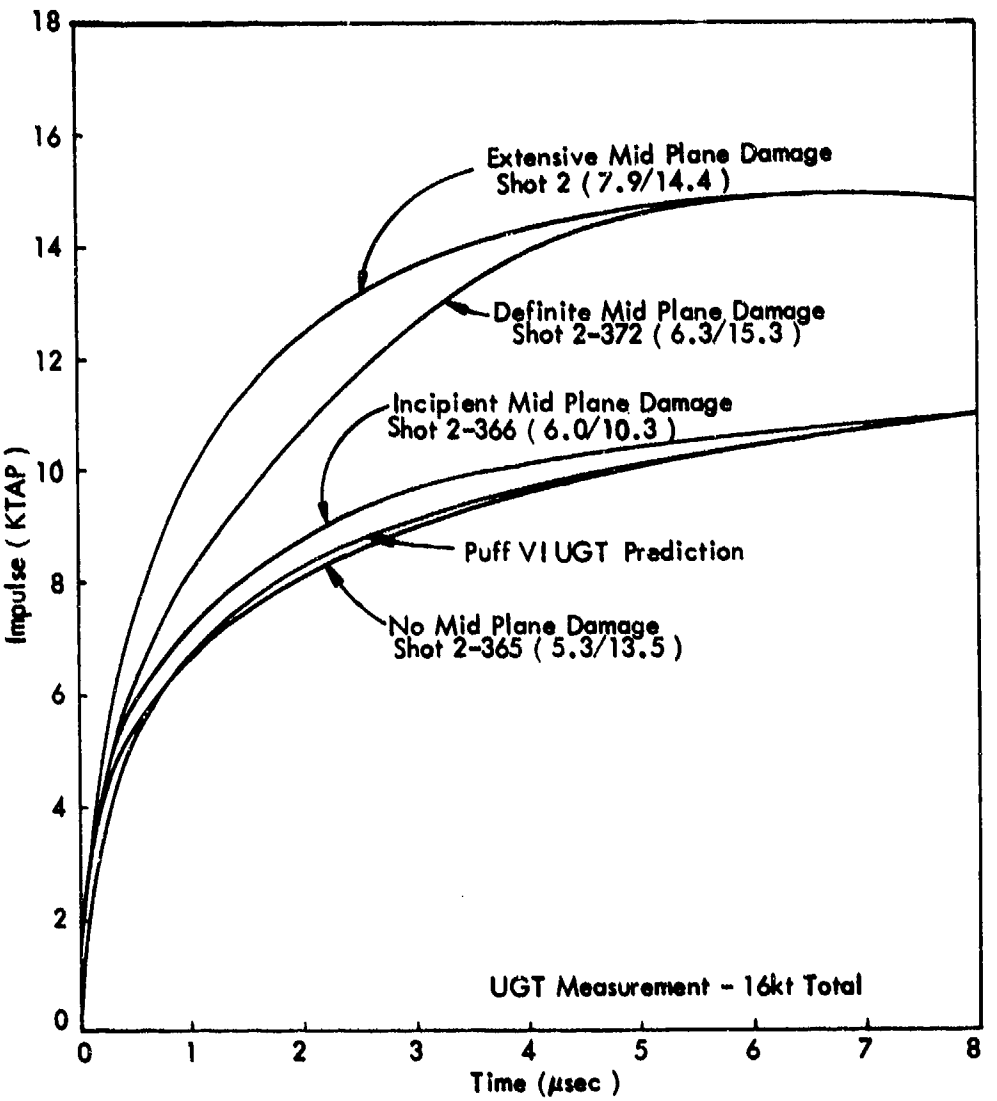

FIGURE 57 IMPULSE VS TIME - 3DQP

Two rings were impacted with magnetic pressure waveforms similar to those waveforms used to produce damage in the arc samples. The first shot on ring 7.1.4 #6 was actually designed to produce a magnetic waveform between arc samples K66 and K70. However, the resultant waveform was similar to K66 and fell in the shaded area as shown in Figure 55. Mid-plane damage was not formed in ring 7.1.4 #6 with this loading condition, just as the magnetic waveform did not produce damage in some of the arc samples. In order to produce mid-plane damage, ring 7.1.4 #4 was shot at a slightly higher level than for ring 7.1.4 #6. The resultant magnetic waveform was nearly identical to that produced for sample K70, and mid-plane damage was formed in the ring, though not nearly as strongly as produced in the arc. Pre- and post-test x-rays of K66, ring 7.1.4 #6, ring 7.1.4 #4, and K70 are shown in Figure 58.

In comparison, K66 and 7.1.4 #6 suffered almost identical rear surface damage, both having lateral fiber lifting[2] 5 plies deep, and rear delaminations[2] 7 plies deep. As mentioned, ring 7.1.4 #6 suffered no mid-plane delaminations while arc K66 did. In light of the arc results detailed in Figure 55 and Table 13, this fact is not surprising. Arc K64, for example, loaded with a magnetic pressure waveform falling in the shaded area of Figure 55, suffered nearly identical rear surface damage as K66 and 7.1.4 #6, yet did not show any mid-plane damage. The lack of mid-plane damage in ring 7.1.4 #6 is therefore consistent with the data shown in Figure 55.

Samples K70 and 7.1.4 #4 suffered failure of nearly the same location, type, and severity of damage. The rear surface damage was nearly identical as K70 had 2 lateral plies lifted[1] from the rear surface, while 7.1.4 #4 lifted[1] 3 plies. K70 suffered rear delamination[1] to a depth of 5 to 6 plies, while 7.1.4 #4 delaminated to a depth of 4 plies. The mid-plane

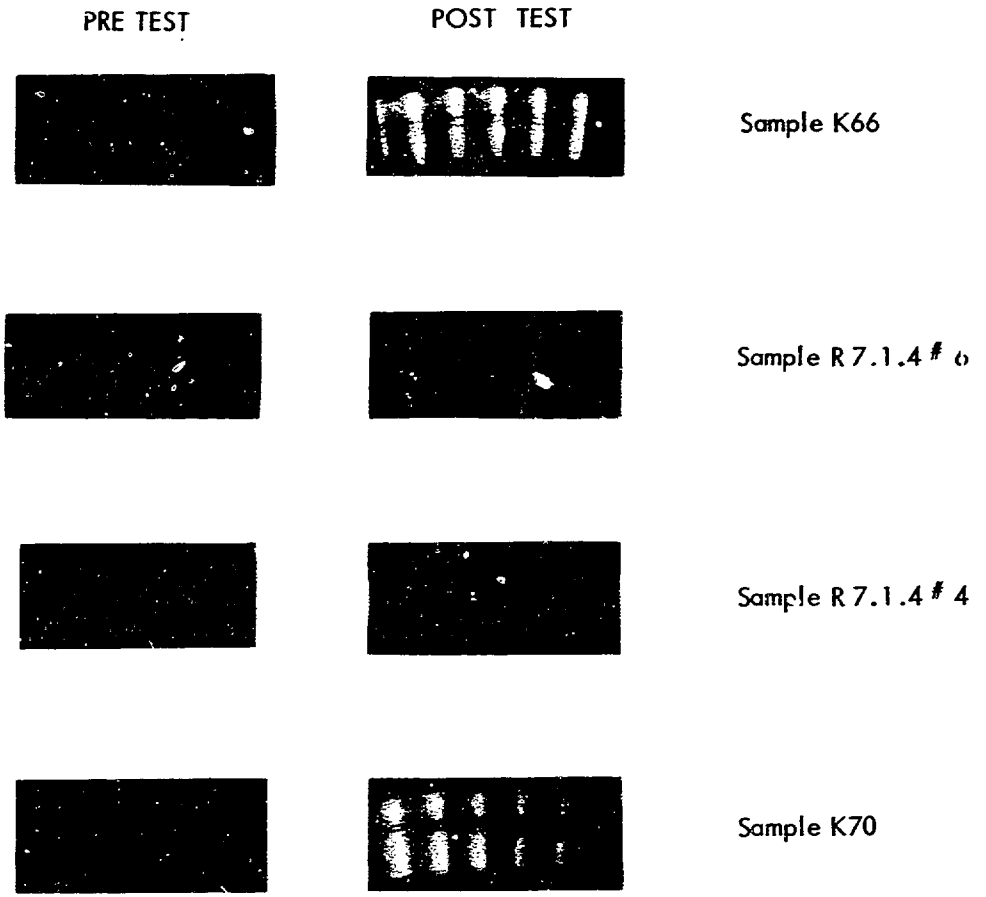

FIGURE 58 RADIOGRAPHS SHOWING DAMAGE SIMILARITY BETWEEN ARC K66 AND RING 7.1.4 # 6 AND BETWEEN ARC K70 AND RING 7.1.4 #4 (THOUGH DAMAGE IN ARC IS OBVIOUSLY MORE SUBSTANTIAL)

damage suffered by K70 and 7.1.4 #4 was also nearly identical. K70 suffered mid-plane delaminations ranging from a depth of 26 to 38 plies while 7.1.4 #4 had damage over a depth of 26 to 36 plies. The location, severity, and type of damage agree well in the mid-plane area of these samples.

Examination of the damage as a function of circumferential angle often provides some insight into the quality of flyer plate symmetry. Observations of the two rings were made by SoRI, and their data are presented in Figure 58 with their permission. The damage on both shots extended to approximately $\pm 67^{\circ}$. As shown in Figures 59 and 60, however, the depth of damage for ring 7.1.4 #6 was most severe approximately 22° off center, indicating the peak load delivered by the flyer plate was skewed. The damage profile for ring 7.1.4 #4 indicated a symmetrical depth of damage which was centered about the $0^{\circ}/180^{\circ}$ axis of the ring. These data would suggest that the load delivered by the flyer plate was symmetrical and centered on 0° for this shot.

5.4 TRANSMITTED WAVE PRESSURE TESTS

Three transmitted wave pressure tests were conducted in order to measure the rear surface pressure-time history in 3DQP at the loading level used to impact arc K70 and ring 7.1.4 #4. The purpose of the tests was to verify that the pressure-time history which comprised the sharp impulse was the same as measured underground. The similarity of the traces was to be compared for 2.2 μsec, the reading time of the AGT quartz gage.

The targets impacted by flyer plates were designed to match the configuration of those fielded underground. Two 3DQP targets were machined flat from arcs to dimensions of 5.72-cm wide by 5.72-cm long by 0.762-cm thick; the arcs were obtained from cylinder 7.1.4 so that the material possessed properties similar to those materials which were fielded under-

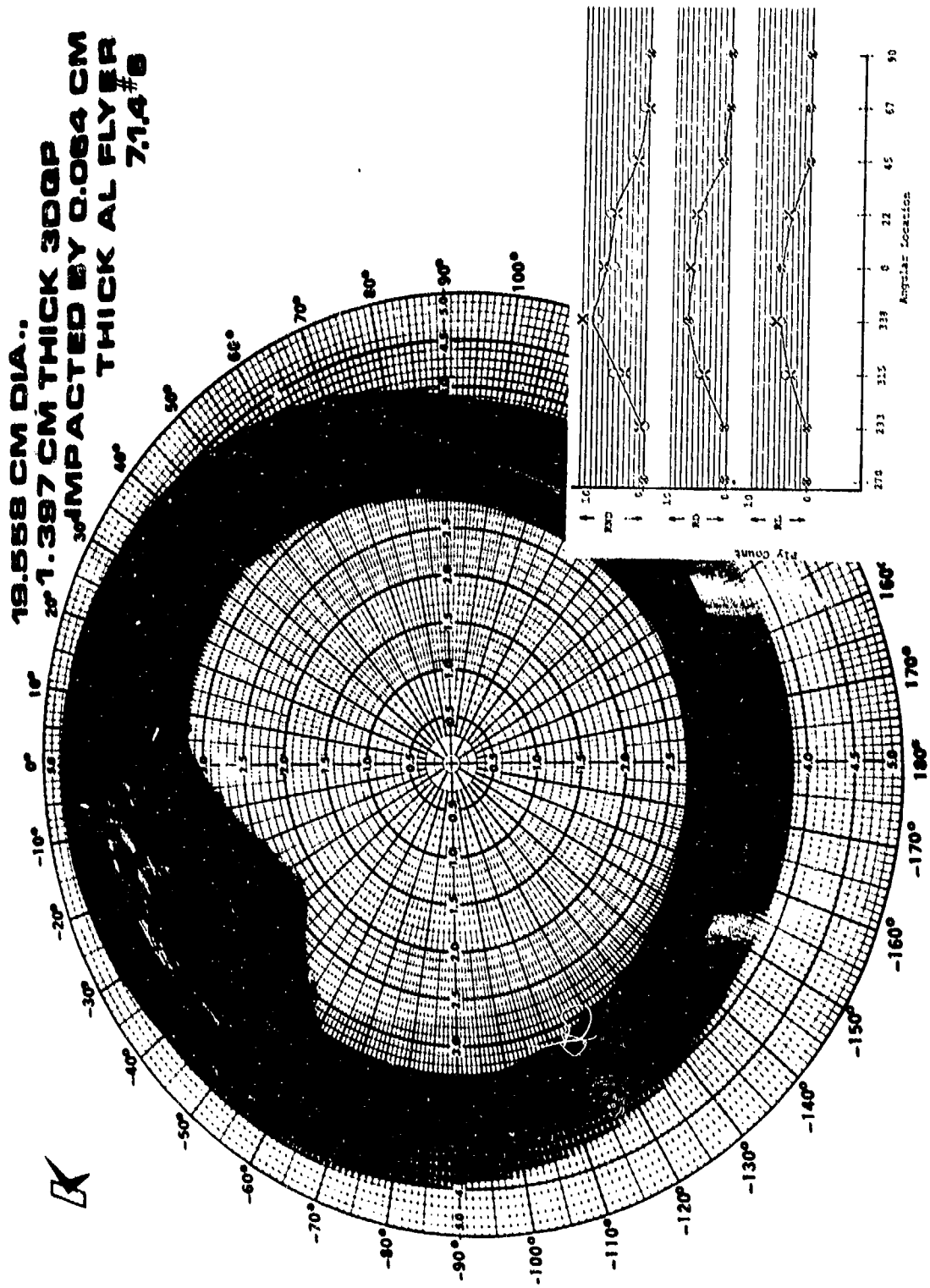

FIGURE 59. DEPTH OF DAMAGE VERSUS ANGULAR STATION FOR RING 7.1.4 #6

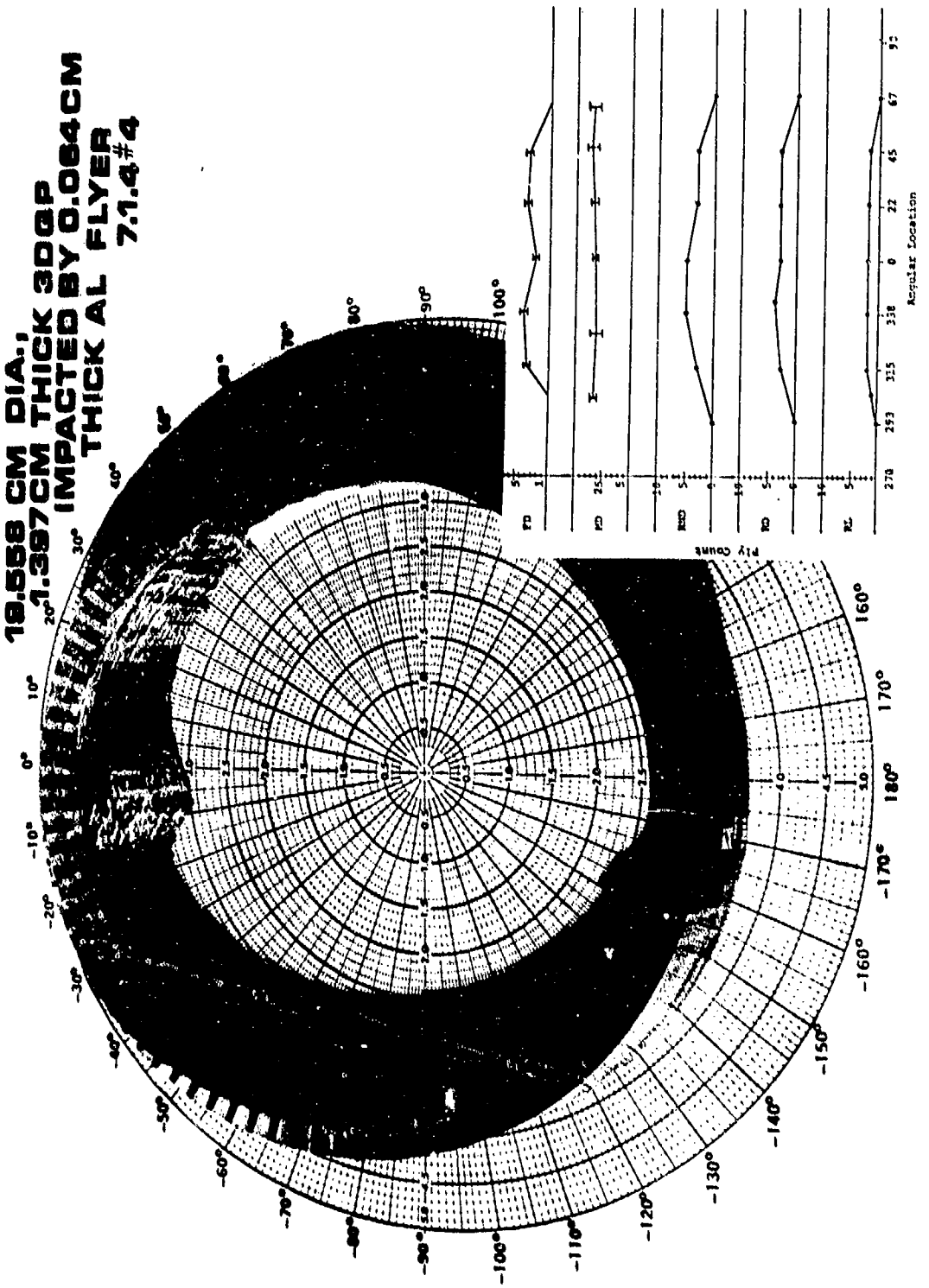

FIGURE 60. DEPTH OF DAMAGE VERSUS ANGULAR STATION FOR RING 7.1.4 #4

ground. The flat samples were then backed with 0.254-cm thick 2024-T3 aluminum buffer plates and 1.270-cm thick x-cut quartz crystals. The quartz crystal was potted in Hysol epoxy. A third sample was constructed with slightly different dimensions. The 3DQP sample was machined into a flat which dimensions were 3.81-cm wide, 3.81-cm long, and 1.40-cm thick. Since the lateral dimensions of the sample were smaller than the diameter of the quartz gage, epoxy was used to fill out the sample; no undesirable effects were observed due to this geometry, probably because of small diameter guard ring cut in the quartz gage. This sample was backed by a 0.160-cm thick 6061-T6 aluminum buffer plate and a 1.270-cm thick x-cut quartz crystal.

The pressure-time transmitted waveforms are presented in Figure 59 along with their associated oscilloscope records. As seen in Figure 61, the oscilloscope voltage records have extremely noise-free baselines, especially considering that the signals were recorded early after bank fire on shots which ultimately produced over 15,000 taps impulsive load. The clean signal eliminates error in the pressure waveform data reduction due to bank discharge noise.

The pressure-time transmitted waveforms from the flyer plate tests are overplotted on this UGT-transmitted waveform in Figure 62. The agreement of the rise times and peak pressures between the UGT trace and AGT flyer plate simulation is excellent. The pulse width produced by the flyer plate seems longer than that produced in the UGT environment, since the UGT unloading wave seems to be falling more quickly than the unloading wave produced by the flyer plate. A complete record is not available, however, since the AGT waveform is clipped at 2.2 μsec due to the recording time limitations of the 1.27-cm thick quartz gage.

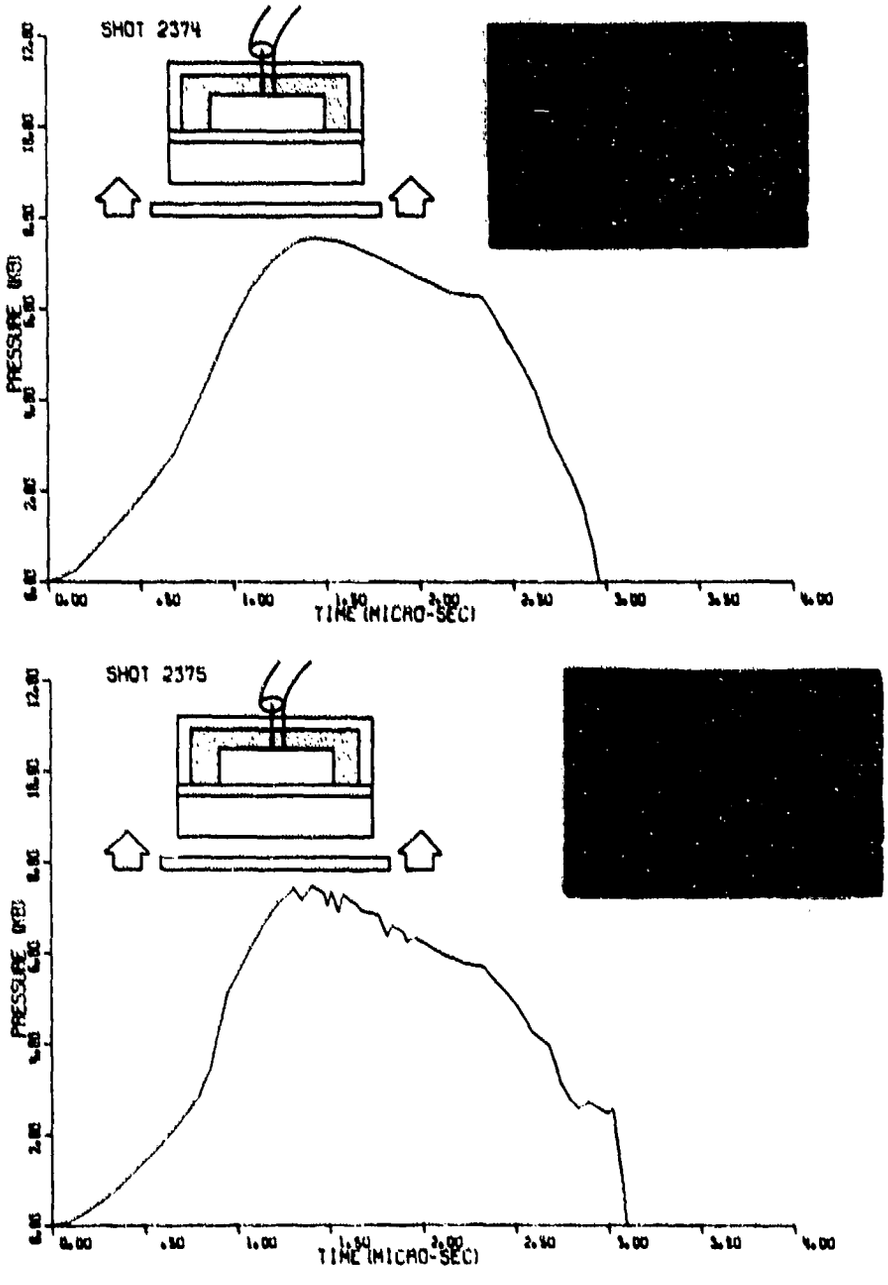

FIGURE 61. TRANSMITTED PRESSURE-TIME WAVEFORMS RECORDED BY QUARTZ GAGE

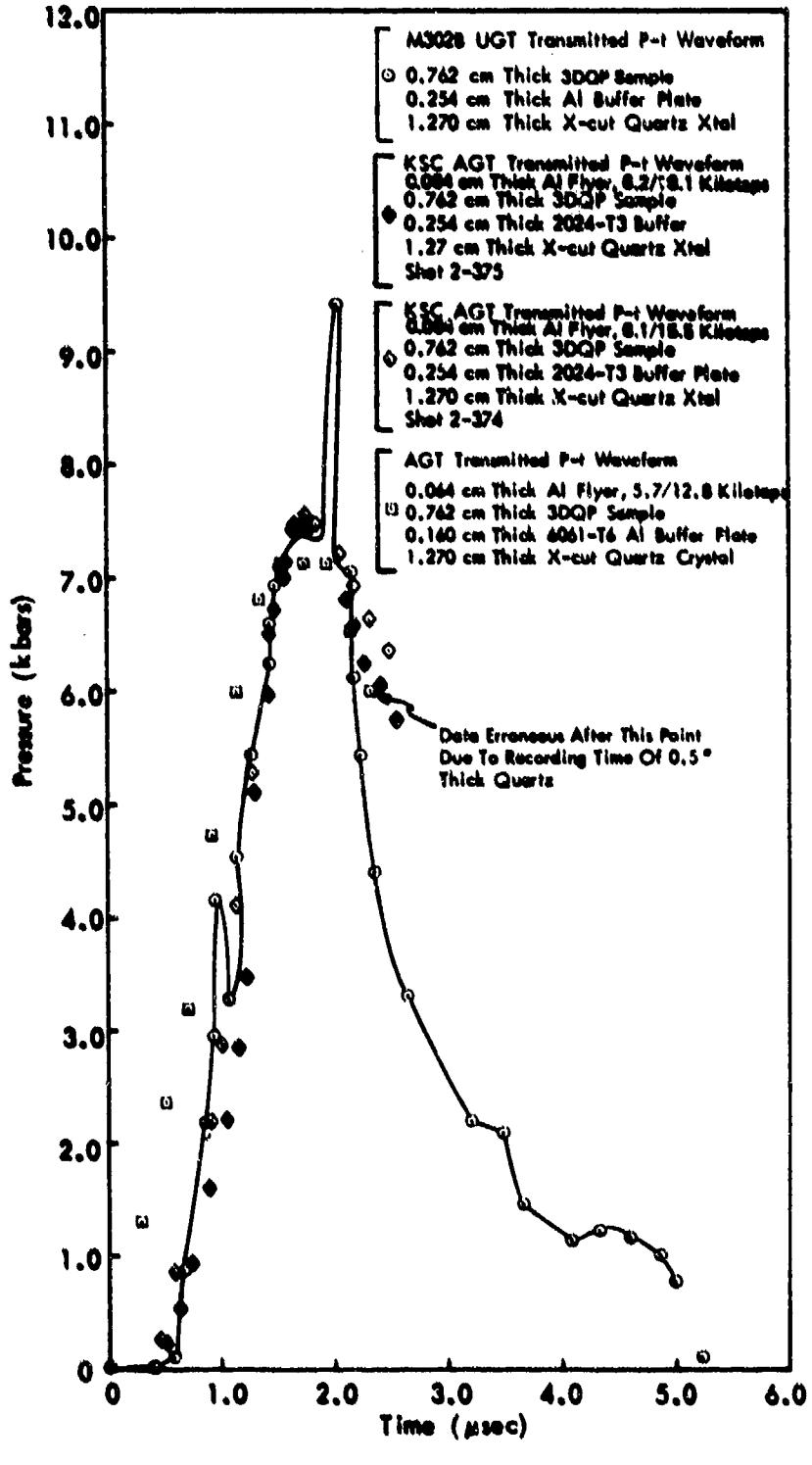

FIGURE 62. COMPARISON OF UGT AND AGT TRANSMITTED P-t WAVEFORMS

In brief summary, the AGT and UGT rise time and peak pressures match nicely. The AGT pulse width may be longer, however, than the UGT pulse width. Even so, the overall agreement between the AGT and UGT pressure-time histories at the rear surface of the 3DQP samples suggests a successful match of the desired loading conditions by AGT techniques.

5.5 STRUCTURAL RESONANT FREQUENCY TESTS

Dynamic loading conditions caused by an Electro-Magnetic Excitation (EME) device can determine several of the resonant frequencies associated with membrane response and bending of a ring. Relatively simple ring or shell theories can relate these resonant frequencies to material properties for the ring. For example, a uniformly thick, homogeneous, elastic ring has the following frequencies of interest.

$$f_o = \sqrt{E/\rho}\ /2\pi R \qquad (5.1)$$

$$f_2 = .775\sqrt{E/\rho}\ h/2\pi R^2 \qquad (5.2)$$

where

- E = Young's modulus (in both tension and compression)
- ρ = Mass density
- R = Midsurface radius
- f_o = First membrane frequency
- f_2 = First bending frequency

Either of these two frequencies can be used to deduce E, as h, R and ρ can be easily measured.

For rings that have non-uniform properties an elastic-shell formulation is somewhat more complicated. If it is assumed that E and h have spatial variation of the form

$$E(\theta) = E(-\theta) = E_o - \Delta E\cos\theta \qquad 0 \le \theta \le 90$$
$$= E_o \qquad 90 < \theta \le 180$$

$$h(\theta) = h(-\theta) = h_o - \Delta h \cos(90\ \theta/\theta_c) \qquad 0 \leq \theta \leq \theta_c$$
$$= h_o \qquad \theta_c < \theta \leq 180$$

then f_o^{**}, the first membrane frequency, can still be derived without excessive algebra.

$$f_o^* = \left(\sqrt{E_o}/\rho\ /2\pi R\right) \sqrt{\frac{1 - \Delta E/E_o\pi - 2\Delta h\theta_c/h_o\pi \cdot 180}{1 - 2\Delta h\theta_c/h_o\pi \cdot 180}} \qquad (5.4)$$

A combination of (5.4) and (5.1) can be solved for ΔE if this ΔE and Δh occurred between tests on virgin and degraded material.

$$\frac{\Delta E}{E_o} = \pi(1 - 2\Delta h\theta_c/h_o\pi \cdot 180)(1 - (f_o^*/f_o)^2) \qquad (5.5)$$

Equation (5.5) is quite useful in deducing ΔE, the change in Young's modulus at $\theta = 0$, due to wave propagation damage.

Table 14 is a compilation of the frequencies measured by EME for Ring Z and samples 7.1.4 #4 and #6. Each of these rings have been measured by SoRI and a reasonable approximation for $h(\theta)$ is

Ring Z

$$h(\theta) = h(-\theta) = .552 - .098 \cos(\theta) \qquad 0 \leq \theta \leq 90 \qquad (5.6)$$

7.1.4 #4 and 7.1.4 #6

$$h(\theta) = h(-\theta) = .552 - .057 \cos(90\ \theta/55) \qquad 0 \leq \theta \leq 55 \qquad (5.7)$$

Application of these thickness relationships to the formula of Equation (5.5) yields an estimate of E for each of the 3 rings. Table 15 summarizes these data. Table 15 also demonstrates that a combination of the first flexural frequency and the first

TABLE 14 RESONANT FREQUENCIES (HERTZ)

	f_o	f_2	f_4^+
PRE-TEST MEASUREMENTS			
UGT RING Z	--	--	--
7.1.4 #6	6948	810	2206
7.1.4 #4	6939	806	2197
POST-TEST MEASUREMENTS			
UGT RING Z	6649	715	1966
7.1.4 #6	6629	743	2015
7.1.4 #4	6506*	738	2010

*Resonant frequency was inaudible, this value estimated from 90° strain gage record.

+f_4 = second bending frequency

TABLE 15 RING THICKNESS AND MODULUS SUMMARY

h_o=.552 in, R=3.546 in
ρ=1.56x10^{-4} lb-sec^2/in^4

SAMPLE	$\Delta E/E$	h_{eff} (Inches)[2]	h_{min} (Inches)[3]	h_{rear} (Inches)
Ring Z	.246[1]	.492	.457	.050
7.1.4 #6	.270	.513	.495	.057
7.1.4 #4	.374	.519	.510	.042

[1]Pre-test frequency is assumed identical to 7.1.4 #6.

[2]h_{eff} = uniform thickness associated with f_2^* (Equation (5.2))

[3]SoRI measurements.

membrane frequency can be used to calculate an "effective" thickness that is between the original ring thickness and the final minimum thickness. This effective thickness appears to be quite a bit nearer to the minimum thickness and can, therefore, be used as a quick estimate of damage. Table 15 also shows the change in thickness for rear surfaces as these are the ones that are being simulated in AGT.

The EME resonance data in conjunction with first-order shell thoeries leads to the conclusion that the modulus degradation in Ring Z is closer to that of 7.1.4 #6 than 7.1.4 #4.

5.6 AGT/UGT STRAIN GAGE CORRELATIONS

All theoretical predictions of AGT/UGT 3DQP experiments performed by KSC have utilized the TWORNG computer program (see 4.1.3). For Ring Z and both 7.1.4 #4 and #6, it was determined that the structural deformation was not severe enough to require a yielding model. Furthermore, the fabricating process for this type of 3DQP seemed to produce a nearly equal modulus of compression and modulus of tension. All calculations thus used the values

$$E_o = 3.80 \times 10^6 \text{ psi}$$

$$\rho = 1.56 \times 10^{-4} \text{ lb} \cdot \text{sec}^2/\text{in}^4$$

$$\% \text{ damping} = .5$$

Thickness and modulus variation identical to those of Section 5.5 with angle (θ) were allowed. The effect of modulus variation is important enough that a parameter sensitivity study on TWORNG was also completed. Figure 63 shows the effect on the strain record at $\theta = 90^\circ$ of allowing $\Delta E/E_o$ to

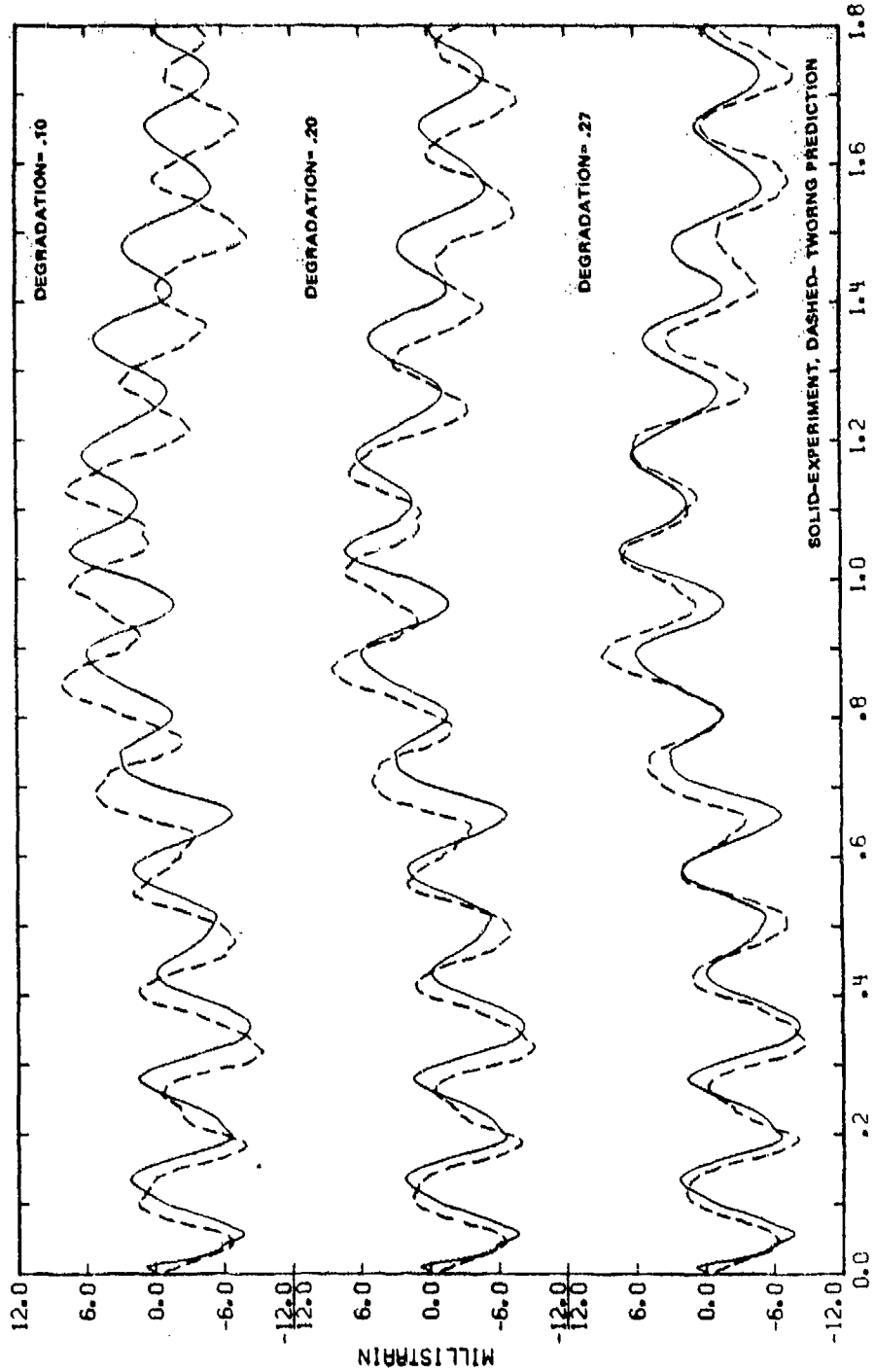

FIGURE 63. EFFECT OF DEGRADATION ON TWORNG PREDICTION AT THETA = 90. (7.1.4 f 6)

vary. The correlation for $\Delta E/E_o$ = .270 is quite good, and this agreement verifies the EME measurements and Equation (5.4). Figure 64 demonstrates the TWORNG/experimental correlation for other strain traces on 7.1.4 #6.

The correlations for 7.1.4 #4 and Ring Z are given in Figures 65 and 66. Agreement between theory and experiment in Figure 65 is considered to be a reasonably good correlation for Ring Z until time = .62 msec. After this time the Ring Z experimental data seems to have an increased amplitude for the membrane frequency component. This implies that an additional load has been imparted to the ring at about .6 msec. It is not known what caused this unexpected load.

5.7 AGT SIMULATION ASSESSMENT

Figures 67 and 68 illustrate overplots of strain records for AGT/UGT comparisons. The AGT experiment on 7.1.4 #6 brackets the UGT data because the 180° ID trace has a higher membrane amplitude than the UGT trace and the 180° OD trace has a lower amplitude. Frequency correlations appear to be acceptable for the experiment on 7.1.4 #4, the AGT resulted in amplitudes that were somewhat large. The frequency correlation was not significantly different than that for 7.1.4 #6. Table 16 shows the peak strain comparisons in a quantitative manner. The conclusion remains that 7.1.4 #6 is a slightly better match for Ring Z than 7.1.4 #4, but either correlates reasonably well out to .62 msec.

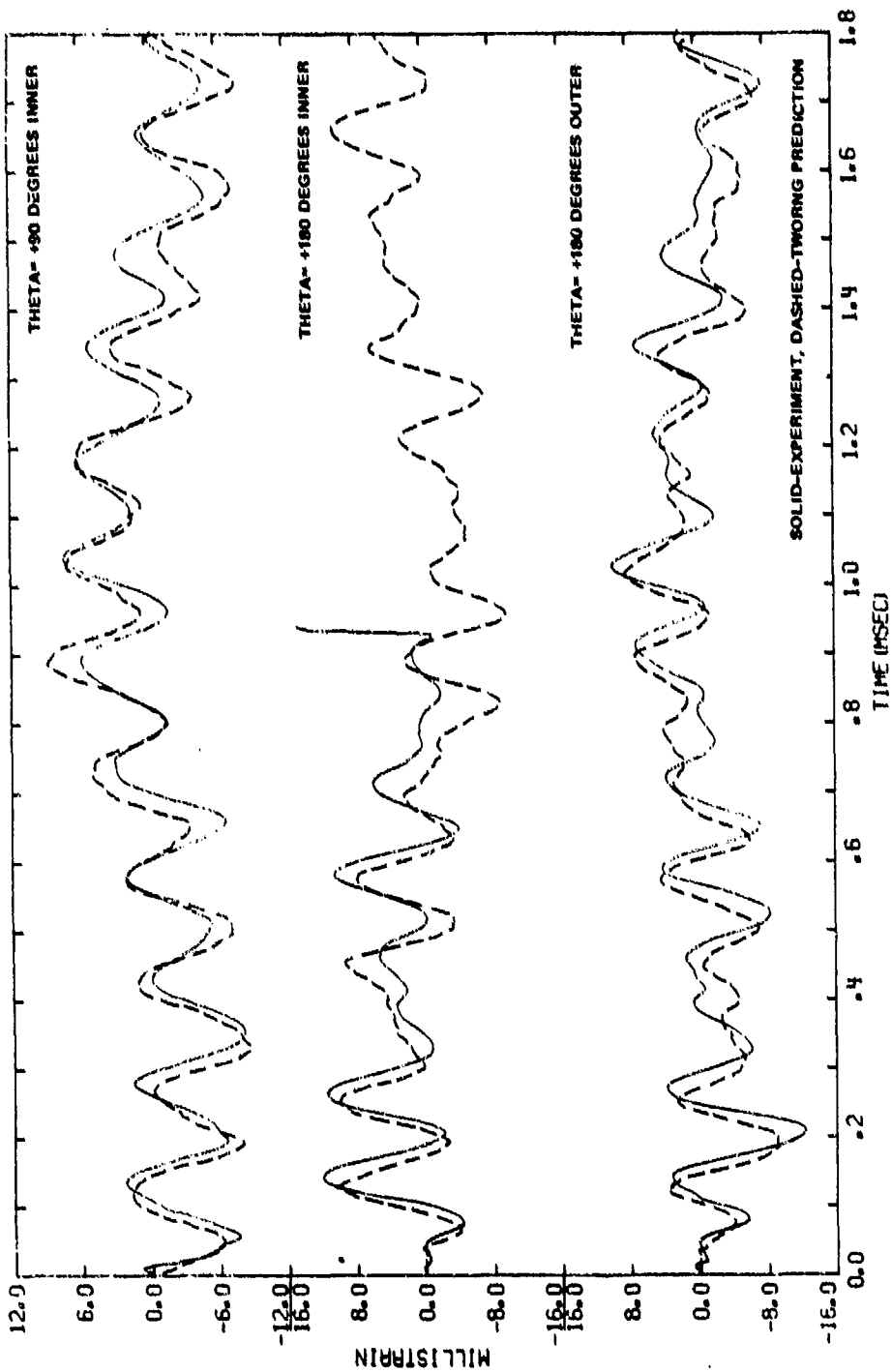

FIGURE 64. DYNAMIC RESPONSE CORRELATIONS FOR A 19.6 CM O.D. 3DQP RING (SHOT 2-366) ($\Delta E/E$) = .270

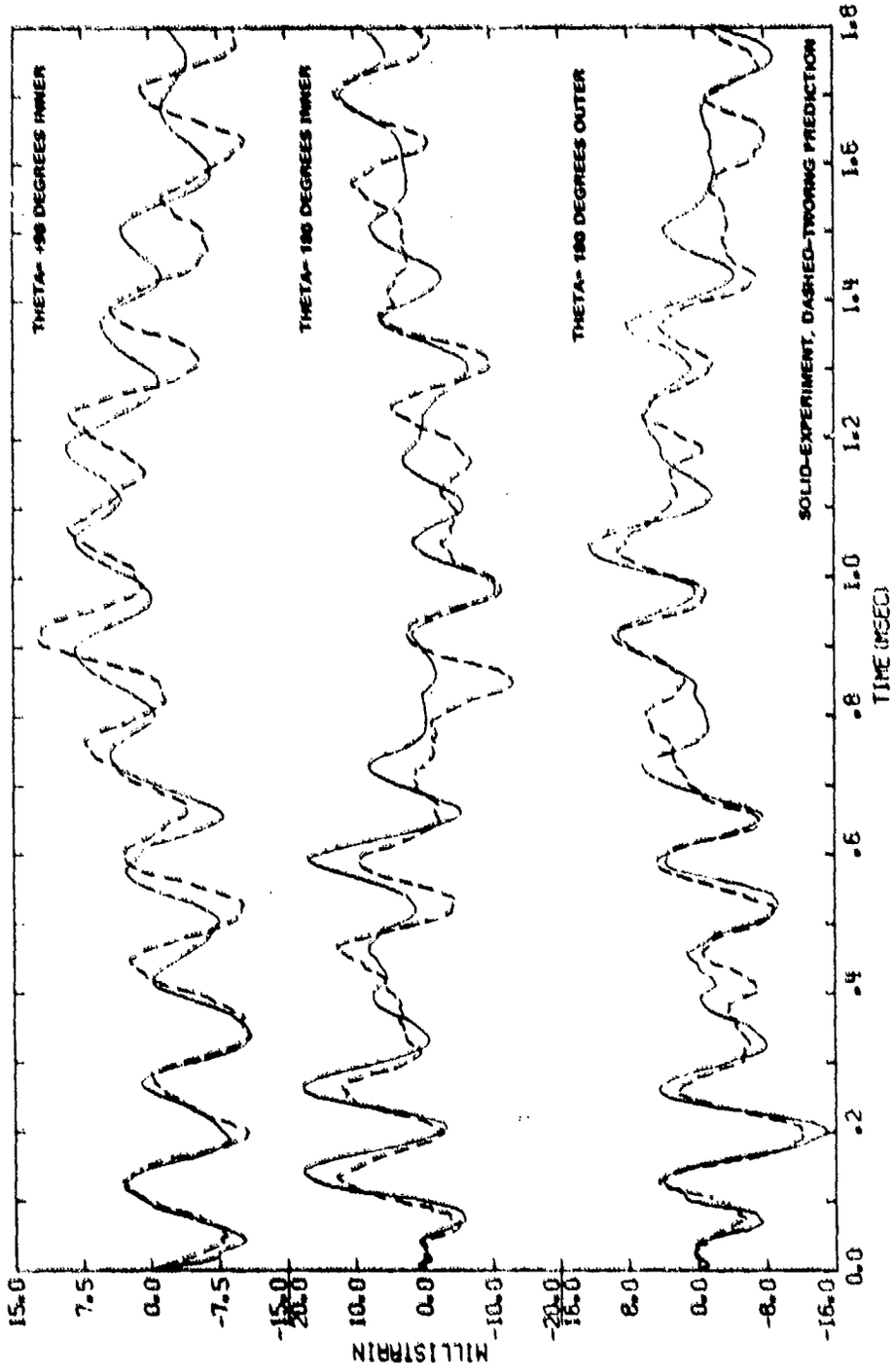

FIGURE 65. DYNAMIC RESPONSE CORRELATIONS FOR A 19.6 CM O.D. 3DQP RING (SHOT 2-372) ($\Delta E/E$) = 0 374

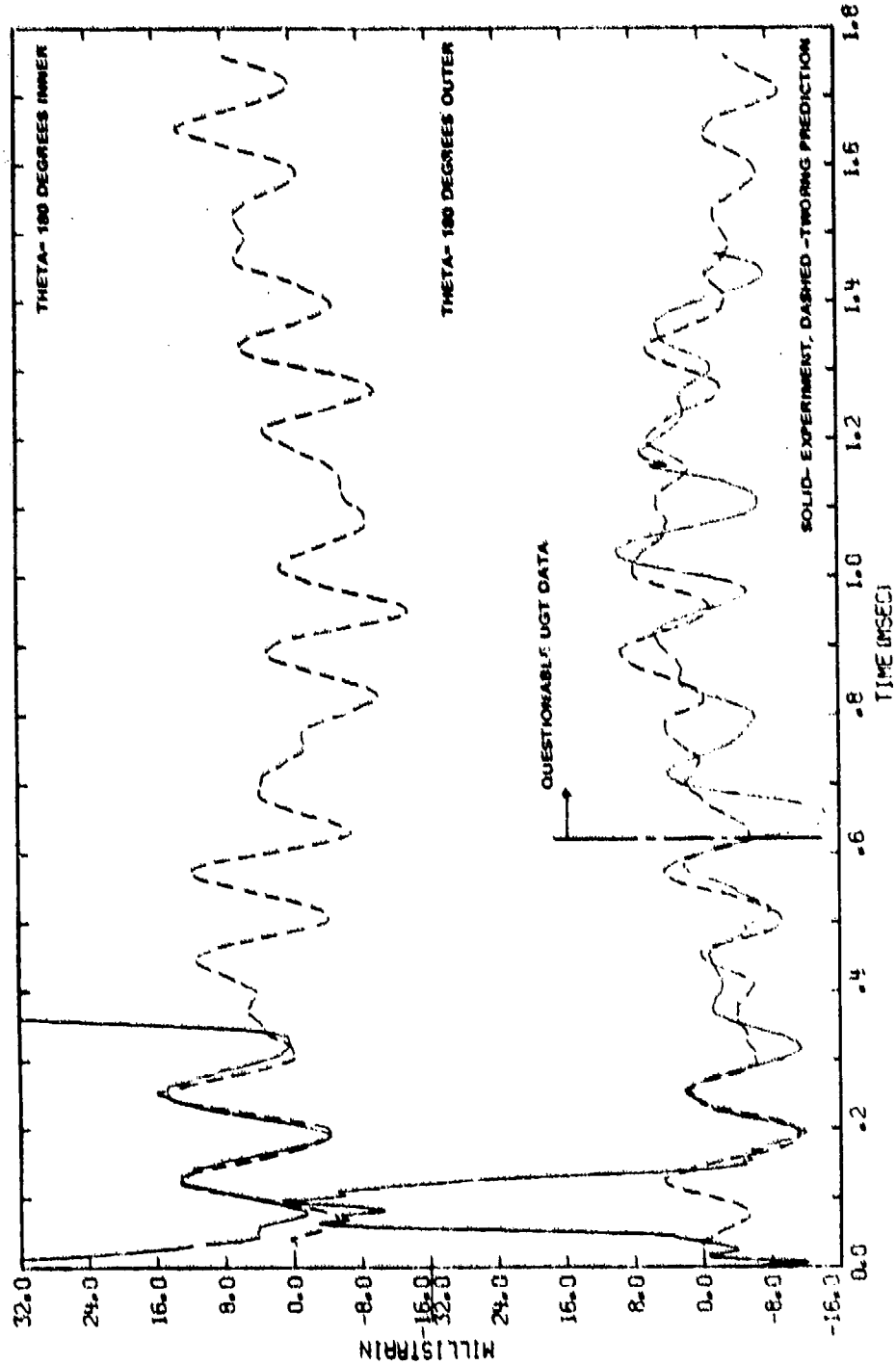

FIGURE 66. DYNAMIC RESPONSE CORRELATIONS FOR UGT ($\Delta E/E$) = .246

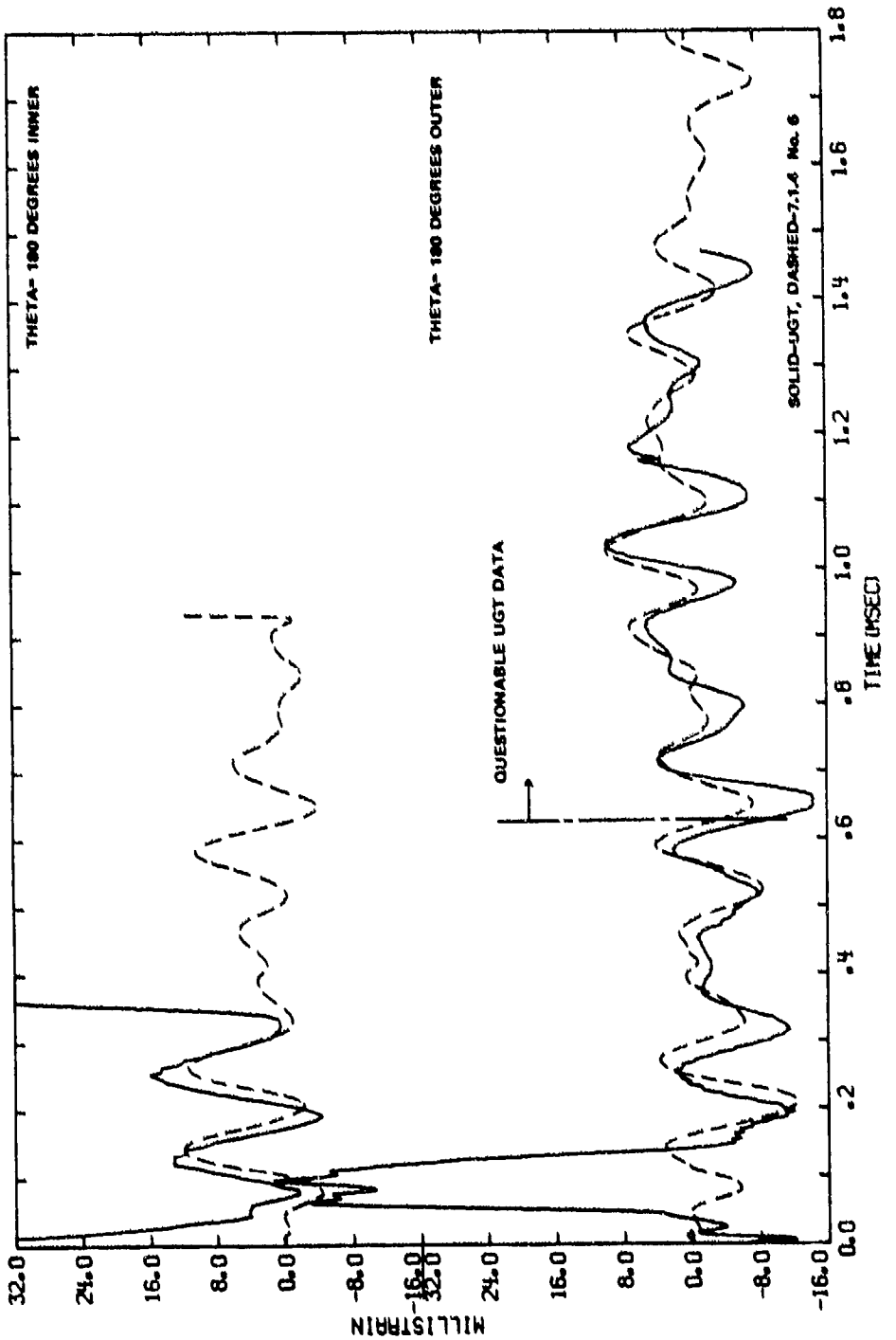

FIGURE 67. DYNAMIC RESPONSE COMPARISONS UGT & AGT

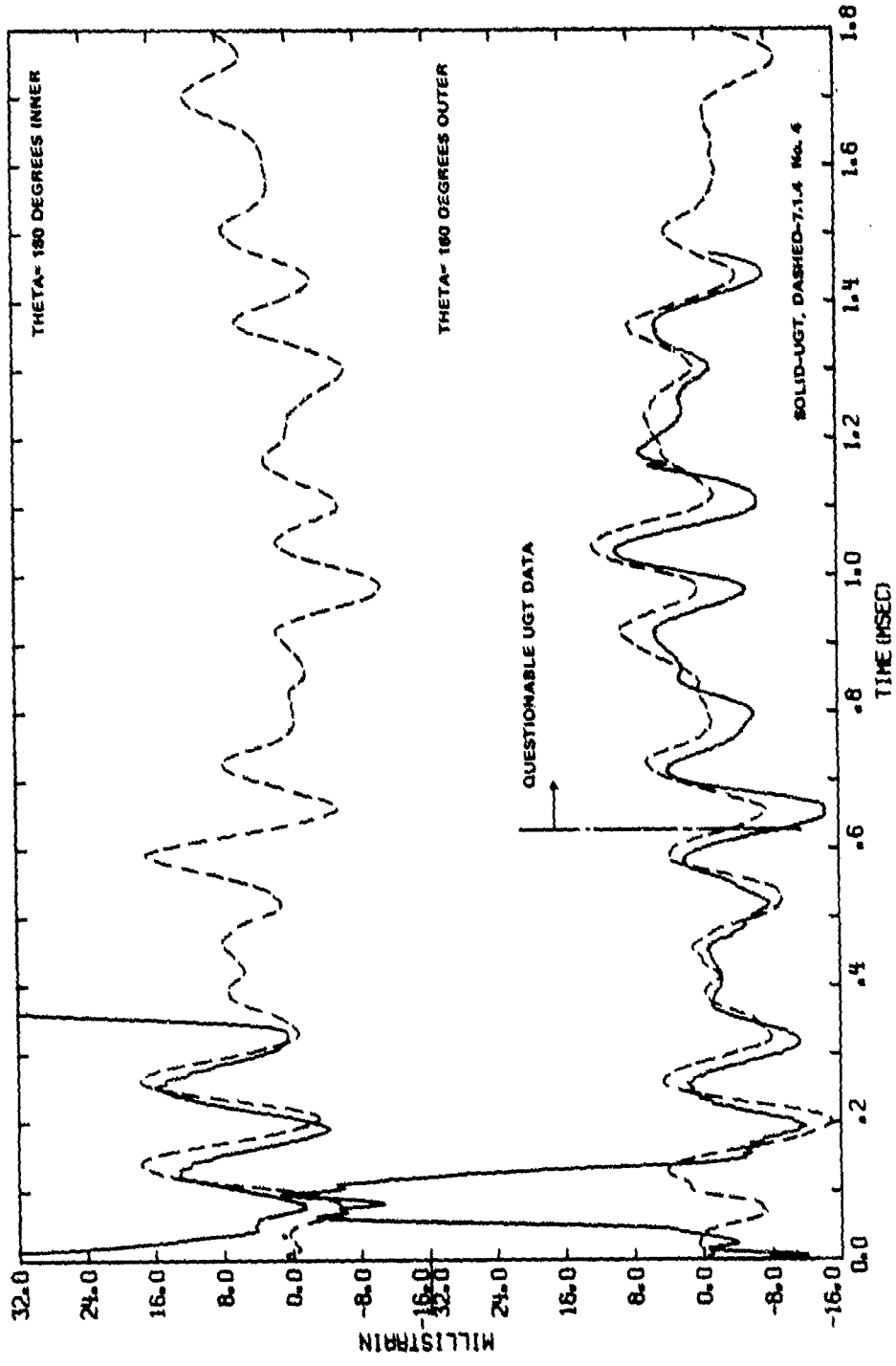

FIGURE 68. DYNAMIC RESPONSE COMPARISONS UGT & AGT

TABLE 16 PEAK STRAIN COMPARISONS AT EARLY TIMES

	SAMPLE	TIME (μSEC)	STRAIN (με)
180° OUTER GAGE			
	Ring Z	195.	-12.0
	7.1.4 #6	212.	-12.4
	7.1.4 #4	205.	-15.0
180° INNER GAGE			
	Ring Z	252.	16.0
	7.1.4 #6	264.	11.4
	7.1.4 #4	264.	17.6

SECTION 6

RESULTS AND CONCLUSIONS

The following conclusions were made from work performed for the Facility Correlation Study.

1. The flyer plate for the facility correlation would be 0.64-mm thick aluminum.

2. The free run distance for the facility correlation would be 2.54 mm.

3. The 50.8-cm diameter 3DQP material used for the facility correlation was typical of "A" process 3DQP.

4. The damage mode of the 50.8-mm diameter 3DQP material was mid-plane cracking and rear surface fiber lifting.

5. 0.3-mm thick aluminum flyer plates produced more stress wave damage in the 50.8-mm diameter 3DQP material than was produced by 0.64-mm thick aluminum flyers.

6. The accuracy of the impulse values quoted by KSC was found to be ±7.5% by three independent techniques.

7. The KSC and AWRE facilities are capable of producing equivalent stress wave damage in 3DQP within approximately ±10% of their quoted impulse values.

8. Experimental and theoretical combined response data on rings exhibit good correlation for aluminum and excellent correlation for "A" process 3DQP.

The following conclusions were made from work performed for the UGT Simulation Study.

1. For the AGT/UGT simulation conditions, it has been shown that the proper pressure-time loading history is the most pertinent parameter for reproducing UGT material damage levels and damage location, transmitted pressure profiles, and early-time structural response of 3DQP. Impulse and impulse ratios are not the key parameters.

2. Capacitor bank pulse shaping techniques have been shown to produce the proper pressure-time loading history necessary for AGT/UGT simulation.

3. Using these AGT capacitor bank techniques, 3DQP samples have been impacted and have been found to approximate Ring Z damage level and location, transmitted pressure waveforms, and early-time strain response.

4. AGT Ring 7.1.4 #4 suffered damage of a similar nature as Ring Z: rear surface delamination to a depth of 4 or 5 plies on both rings, and mid-plane delamination closer to the impact surface and slightly more intense than experienced by Ring Z.

5. The peak AGT transmitted pressure matches the UGT value, but probably has slightly longer

pulse width. Issue is clouded by 2.2 microsecond recording time of AGT quartz gage.

6. Comparisons between AGT and UGT strain records are quite good out to .62 milliseconds. AGT experiment on 7.1.4 #6 produces a slightly better strain record correlation than the AGT experiment on 7.1.4 #4.

7. EME measurements demonstrate that the apparent modulus degradation experienced by the AGT and UGT rings is very similar.

8. TWORNG calculations, based upon the apparent degraded modulus determined by EME measurements, provide good correlations of the AGT and UGT measured strains. These successful correlations demonstrate an overall understanding of the simulation parameters, as well as the material and structural modeling. Also these correlations lend credence to the dynamic degraded modulus measurement of the EME facility.

REFERENCES

1. Larrabee, A. D., Meagher, T. F. V., and Webster, L. D., "Calculation of Magnetically Driven Flyer Behavior From Bank Discharge Data Records," KN-70-62(R), December 1970.

2. Private communication, Mr. Gene Fornaro, data used by permission; or subsequently reported by SoRI, and used by permission.

3. Bealing, R., "H10.1 Data Report No. 39: HP 65 Bounce Estimation," SWAI/RB/7610/212.

4. Webster, L. D., "Three Analytical Studies Pertinent to Structural Testing," KN-69-202(R), Kaman Nuclear, 15 May 1969.

5. Koenig, J. R. and Fornaro G. F., "Evaluation of the Compressive Properties of a Special 3DQP," SoRI, September 1976, DNA 4174F, Defense Nuclear Agency, Washington, DC.

6. Gurtman, G. A., et al, "3DQP AGT/UGT Correlation Study (U)," System, Science and Software, March 1978, DNA 4597, Defense Nuclear Agency, Washington, DC.

DISTRIBUTION LIST

DEPARTMENT OF DEFENSE

Assistant to the Secretary of Defense
Atomic Energy
ATTN: Executive Assistant

Defense Advanced Rsch. Proj. Agency
ATTN: TIO

Defense Documentation Center
Cameron Station
2 cy ATTN: DD

Defense Intelligence Agency
ATTN: DT-2

Defense Nuclear Agency
ATTN: STSP
ATTN: SPSS
ATTN: DDST
ATTN: SPAS
ATTN: SPTD
4 cy ATTN: TITL

Field Command
Defense Nuclear Agency
ATTN: FCPR
ATTN: FCTMD

Joint Chiefs of Staff
ATTN: SAGA/SFD
ATTN: SAGA/SSD
ATTN: J-5, Force Planning & Program Div.
ATTN: J-5, Nuclear Division

Joint Strat. Tgt. Planning Staff
ATTN: JLTW-2
ATTN: JPTM

Livermore Division, Field Command, DNA
Lawrence Livermore Laboratory
ATTN: FCPRL

Under Secretary of Def. for Rsch. & Engrg.
ATTN: Strategic & Space Systems (OS)

DEPARTMENT OF THE ARMY

BMD Advanced Technology Center
Huntsville Office
ATTN: M. Whitefield
ATTN: ATC-T, M. Capps

BMD Program Office
ATTN: DACS-BMT, J. Shea
ATTN: DACS-BMZ
ATTN: DACS-BMT, C. McLain
ATTN: DACS-BMZ-D, J. Davidson
ATTN: Technology Division

BMD Systems Command
ATTN: BMDSC-TEN, N. Hurst

Deputy Chief of Staff for Ops. & Plans
ATTN: Dep. Dir. for Nuc. Plans & Policy

DEPARTMENT OF THE ARMY (Continued)

Deputy Chief of Staff for Rsch. Dev. & Acq.
ATTN: Nuclear Team

Harry Diamond Laboratories
ATTN: DELHD-RC, R. Oswald/D. Schallhorn
ATTN: DELHD-RBH, J. Gwaltney
ATTN: DELHD-NP

U.S. Army Ballistic Research Labs.
ATTN: DRXBR-X, J. Meszaros
ATTN: DRDAR-BLE, J. Keefer
ATTN: DRXRD-BVL, W. Schuman, Jr.

U.S. Army Material & Mechancis Rsch. Ctr.
ATTN: DRXMR-HH, J. Dignam

U.S. Army Materiel Dev. & Readiness Cmd.
ATTN: DRCDE-D, L. Flynn

U.S. Army Missile R&D Command
ATTN: DRDMI-TKP, W. Thomas

U.S. Army Nuclear & Chemical Agency
ATTN: Library

U.S. Army Research Office
ATTN: Technical Library

DEPARTMENT OF THE NAVY

Naval Research Laboratory
ATTN: Code 7770, G. Cooperstein
ATTN: Code 2627
ATTN: Code 5180, M. Persechino

Naval Sea Systems Command
ATTN: Code 0351
ATTN: 0333A, M. Kinna

Naval Surface Weapons Center
ATTN: Code R10, J. Petes
ATTN: Code K06, C. Lyons
ATTN: Code 2302
ATTN: Code F31

Naval Weapons Evaluation Facility
ATTN: L. Oliver

Office of the Chief of Naval Operations
ATTN: R. Blaise
ATTN: Op-604
ATTN: Op-981

Strategic Systems Project Office
ATTN: NSP-273
ATTN: NSP-272

DEPARTMENT OF THE AIR FORCE

Aeronautical Systems Division, AFSC
ATTN: ENFTV

Air Force Rocket Propulsion Laboratory
ATTN: RTSN, G. A. Beale

This document is being sent to the below listed contractors for the use of the individuals listed. Recipient contractors are requested to validate individuals' clearances before forwarding document to same.

DEPARTMENT OF THE AIR FORCE (Continued)

Air Force Materials Laboratory
ATTN: MBE, G. Schmitt
ATTN: MBC, D. Schmidt
ATTN: T. Nicholas

Air Force Systems Command
ATTN: SOSS
ATTN: XRTO

Air Force Weapons Laboratory
ATTN: DYT
ATTN: DYV
ATTN: DYS
ATTN: NT
ATTN: SUL

Deputy Chief of Staff
Research, Development, & Acq.
ATTN: AFRDQSM
ATTN: AFRD

Foreign Technology Division, AFSC
ATTN: TQTD
ATTN: SDBS, J. Pumphrey
ATTN: SDBG

Space & Missile Systems Organization/DY
ATTN: DYS

Space & Missile Systems Organization/MN
ATTN: MNNR
ATTN: MNNH

Space & Missile Systems organization/RS
ATTN: RSS
ATTN: RSMA
ATTN: RSSE

Strategic Air Command/XPFS
ATTN: XPQM
ATTN: XOBM
ATTN: XPFS
ATTN: DOXT

DEPARTMENT OF ENERGY

Lawrence Livermore Laboratory
ATTN: Doc. Con. for D. Hanner
ATTN: Doc. Con. for L-92, C. Taylor
ATTN: Doc. Con. for L-125, J. Keller
ATTN: Doc. Con. for L-94, L. Woodruff

Los Alamos Scientific Laboratory
ATTN: Doc. Con. for J. McQueen/J. Taylor
ATTN: Doc. Con. for D. Shover
ATTN: Doc. Con. for R. Dingus
ATTN: Doc. Con. for R. Skaggs

Office of Military Application
ATTN: Doc. Con. for Res. & Dev. Branch

Sandia Laboratories
Livermore Laboratory
ATTN: Doc. Con. for H. Norris, Jr.
ATTN: Doc. Con. for T. Gold

DEPARTMENT OF ENERGY (Continued)

Sandia Laboratories
ATTN: Doc. Con. for M. Forrestal
ATTN: Doc. Con. for R. Boade
ATTN: Doc. Con. for C. Mehl
ATTN: Doc. Con. for M. Cowan

DEPARTMENT OF DEFENSE CONTRACTORS

Acurex Corporation
ATTN: J. Huntington

Aerospace Corporation
ATTN: R. Crolius
ATTN: W. Barry
ATTN: R. Mortensen
ATTN: R. Strickler
ATTN: W. Mann

Avco Research & Systems Group
ATTN: P. Grady
ATTN: J. Gilmore
ATTN: W. Broding
ATTN: J. Stevens
ATTN: Document Control

Battelle Memorial Institute
ATTN: M. Vanderlind

Boeing Company
ATTN: B. Lempriere

California Research & Technology, Inc.
ATTN: K. Kreyenhagen

Effects Technology, Inc.
ATTN: R. Parrino/M. Rosen
ATTN: R. Wengler/R. Bick

Ford Aerospace & Communications Corp.
ATTN: P. Spangler

General Electric Company
Space Division
ATTN: D. Edelman
ATTN: G. Harrison

General Electric Company
Re-Entry & Environmental Systems Div.
ATTN: P. Cline

General Electric Co.-TEMPO
Center for Advanced Studies
ATTN: DASIAC

General Research Corp.
Santa Barbara Division
ATTN: R. Rosenthal

Institute for Defense Analyses
ATTN: Classified Library
ATTN: J. Bengaton

Ion Physics Corporation
ATTN: R. Evans

This document is being sent to the below listed contractors for the use of the individuals listed. Recipient contractors are requested to validate individuals' clearances before forwarding document to same.

DEPARTMENT OF DEFENSE CONTRACTORS (Continued)

Kaman AviDyne
Division of Kaman Sciences Corp.
ATTN: R. Ruetenik

Kaman Sciences Corp.
ATTN: W. Doane
ATTN: T. Meagher
ATTN: L. Webster
ATTN: J. Oscarson
ATTN: F. Shelton

Lockheed Missiles & Space Co., Inc.
ATTN: R. Walls
ATTN: O. Burford

Lockheed Missiles & Space Co., Inc.
ATTN: F. Borgardt

Lockheed Missiles & Space Co., Inc
ATTN: F. Fortune

Martin Marietta Corp.
Orlando Division
ATTN: L. Kinnaird

McDonnell Douglas Corp.
ATTN: H. Berkowitz
ATTN: J. Peck
ATTN: M. Schneider
ATTN: L. Cohen
ATTN: E. Fitzgerald

Pacific-Sierra Research Corp.
ATTN: G. Lang

Physics International Co.
ATTN: J. Shea

Prototype Development Associates, Inc.
ATTN: N. Harrington
ATTN: J. MacDonald

R&D Associates
ATTN: F. Field
ATTN: C. MacDonald
ATTN: P. Rausch
ATTN: W. Graham, Jr.

DEPARTMENT OF DEFENSE CONTRACTORS (Continued)

Rand Corp.
ATTN: R. Rapp

Science Applications, Inc.
ATTN: O. Nance
ATTN: W. Yengst

Science Applications, Inc.
ATTN: W. Layson
ATTN: W. Seebaugh

Southern Research Institute
ATTN: C. Pears

SRI International
ATTN: G. Abrahamson
ATTN: H. Lindberg
ATTN: D. Curran

Systems, Science & Software, Inc
ATTN: G. Gurtman
ATTN: T. McKinley

Terra Tek, Inc.
ATTN: S. Green

TRW Defense & Space Sys. Group
ATTN: J. Farrel
ATTN: W. Wood
2 cy ATTN: P. Dai/D. Jortner

TRW Defense & Space Sys. Group
San Bernardino Operations
ATTN: W. Polich
ATTN: L. Berger
ATTN: V. Blankenship

Defense Threat Reduction Agency
45045 Aviation Drive
Dulles, VA 20166-7517

CPWP/TRC March 1, 2000

AD-C013-969

MEMORANDUM TO THE DEFENSE TECHNICAL INFORMATION CENTER
ATTN: OCQ

SUBJECT: DOCUMENT UPDATE

Reference to your enclosed request. The cited document has been cleared for open publication.

DNA-4622F, UNCLASSIFIED, DISTRIBUTION STATEMENT A

If you have any questions, please call me at 703-325-1034.

Ardith Jarrett

ARDITH JARRETT
Chief, Technical Resource Center

Recd 3/8/2000